Title

Resolving the Nearshore: Remote Sensing and Data Driven Analysis of Fine-Scale Mixing, Turbidity, and Sea Surface Temperature of the Ocean off Northern California

Permalink

https://escholarship.org/uc/item/1mc2p4k2

Author

Speiser, William

Publication Date

2024

Peer reviewed|Thesis/dissertation

Resolving the Nearshore: Remote Sensing and Data Driven Analysis of Fine-Scale Mixing, Turbidity, and Sea Surface Temperature of the Ocean off Northern California

By

WILLIAM HENRY BALLEN SPEISER
DISSERTATION

Submitted in partial satisfaction of the requirements for the degree of

DOCTOR OF PHILOSOPHY

in

Hydrologic Sciences

in the

OFFICE OF GRADUATE STUDIES

of the

UNIVERSITY OF CALIFORNIA

DAVIS

Approved:

John L. Largier, Chair

Yufang Jin

Gonzalo Saldías

Committee in Charge

2024

Abstract

Nearshore waters are governed by complex hydrodynamic interactions within landscapes that vary globally. Many of these often-energetic flows are intricate, diverse, and fine-scale, making holistic understanding difficult. Advancements in computational processing, coupled with ever growing environmental datasets and refining remote sensing technologies, offer new opportunities to constrain the controls behind these processes. This dissertation investigates complex, important nearshore hydrodynamics through applications of remote sensing technologies and data analysis. Focusing on the nearshore ocean off the geomorphologically diverse coastline of Northern California, we develop and implement novel methodologies to observe, quantify, and analyze fine-scale processes in each chapter of this dissertation, thereby illuminating coastal hydrodynamics that have been difficult to monitor.

In chapter 1, we analyze the dispersion of turbid freshwater plumes from the Russian River, California, a prototypical small mountainous river system. River plumes of this size, although common and vital in Mediterranean climate regions, have been understudied, leading to significant gaps in understanding. Using 15 years of daily MODIS satellite imagery and environmental data, we reveal the interplay of river discharge, waves, winds, and tides in shaping plume behavior. This analysis serves as a ground truth for previous studies and uncovers previously undiscussed patterns of small to moderate sized river plume dynamics.

Chapter 2 presents a methodology that enhances nearshore temperature monitoring capabilities by utilizing calibration data between high-resolution (100m) Landsat thermal infrared data and coincident moderate resolution (1km) MODIS sea surface temperature (SST) data. Data calibrated by this methodology is tested against in-situ measurements at various distances from the Northern California coast and presents use cases for this high-resolution dataset, demonstrating significant advancement over traditional SST products and offering initial insights into fine-scale temperature mixing processes.

In Chapter 3, we investigate wave-driven cross-shore sediment transport using high resolution (10m) Sentinel-2 remote sensing data, enhanced by machine learning post-processing utilized to resolve nearshore heterogeneity. By isolating turbid water signals and analyzing them alongside wave model data, tidal data, and high resolution (2m) bathymetric data, we characterize sediment transport dynamics across diverse coastal facies. This work constrains how the interplay between wave climate, bathymetric complexity, and sediment availability influences the extent and patterns of offshore turbidity transport in both sandy and rocky environments.

Collectively, the studies in this dissertation advance our understanding of nearshore hydrodynamics by leveraging remote sensing and data analysis constrain to their controls. The methodologies and findings presented here contribute to improved coastal monitoring, management, and research, with potential applications in similar coastal regions globally.

Acknowledgements

When I first moved to California for a job irrelevant to this work, I had no idea of the uniquely privileged life I would build there. I eventually ended up getting to spend my time admiring seascapes- floating on the waters of Tomales Bay and the Russian River estuary, standing on the beaches of Sonoma County, within a research lab overlooking the Pacific Ocean, and through many hours behind a computer monitor in idyllic Petaluma. I want to express my gratitude for my advisor, John Largier, through whom these opportunities were possible. John, I owe you great deal of thanks for the support you have offered me through my pursuits, even ones that were completely tangential to this work. Thank you for allowing me the space to create and experiment, develop independence in my work, make room for error, and learn how to move on. You have taught me a lot on how to make observations, but even more on how to look at life and interpersonal connections, inside and out of academia.

I also want to extend my thanks to my dissertation committee, Gonzalo Saldías and Yufang Jin. Your valuable advice on methodology and encouraging feedback have well impacted this work. You have both donated a great deal of your time to help me with this work and I am very appreciative. I am also grateful to Gregory Pasternack, Fabian Bombardelli, Berkay Basdurak, and Yufang Jin for their time and insightful feedback during my qualifying exam. From their comments and encouragement, I was able to springboard my research.

Through my research, I have met many colleagues and collaborators who have also become friends. Berkay Basdurak, your encouragement and shared laughs in our bi-monthly meetings are always very uplifting and your excitement in producing novel work is motivating. Daniel Buscombe, your enthusiasm, as well as your creativity in extracting as much information as conceivably possible from imagery has greatly impacted this work. Daniel Kozar, you were my first colleague at UC Davis and I am grateful to get to include you in two paragraphs of this section.

I am very grateful for my lab mates in the Coastal Oceanography Group, particularly: Robin Roettger, for your inviting nature and making the lab a positive environment; David Dann, for providing opportunities to escape to the field; and Nicholas Trautman, for your humor and readiness to help.

I would be remiss not to thank the people in my life outside of academia for their role in this work. My time in graduate school took place during a pandemic, through the latter half of my twenties, and in a new place that became my home for many years. I attribute a great deal of the positivity in my life throughout my pursuits in those times to: Abby, Jack, Dan, AJ, Anna, Jonah, Lukas, Elias, Pieter, Max, Willie, and David.

Finally, I would like to thank my brother, Alex, and my mother, Sian, whom I have never had to think twice to turn to. I am so lucky for it to feel obvious in expressing how much you have both supported me throughout my life. I am grateful to Allie and Richard for their warmth. I also thank my late father, Greg, from whom I inherited a great deal of my curiosity.

TABLE OF CONTENTS

Abstract ... ii

Acknowledgements ... iv

TABLE OF CONTENTS ... vi

Introduction ... 1

CHAPTER 1 ... 5

- **Abstract** ... 5
- **1. Introduction** ... 6
  - 1.1 River Plumes ... 8
  - 1.2 Site Description ... 10
- **2. Methods** ... 12
  - *2.1 Environmental Data* ... 12
  - *2.2 Satellite Data* ... 14
  - *2.3 Plume Detection* ... 16
  - *2.4 Regression Analysis* ... 17
- **3. Results** ... 19
  - *3.1 Nearshore Trapping of Plume* ... 19
  - *3.2 Average Plume Pattern* ... 20
  - *3.3 River Discharge Effects* ... 21
  - *3.4 Wind Effects* ... 25
  - *3.5 Tidal Effects* ... 29
- **4. Discussion** ... 30
  - *4.1 River Discharge* ... 31
  - *4.2 Wind Speed and Direction* ... 32
  - *4.3 Waves* ... 34
  - *4.4 Tides* ... 35
  - *4.5 Other Nearby Sources of Turbidity* ... 36
  - *4.6 Implications of Plume Patterns* ... 38
- **5. Conclusion** ... 39
- **Author contribution** ... 40
- **Acknowledgments** ... 41
- **References** ... 41

CHAPTER 2 ... 47

Abstract 47

1. Introduction 48

2. Methods 51

2.1 Study Site 51

2.2 Satellite Data 52

2.3 Brightness Temperature to Sea Surface Temperature Calibration 55

2.4 Data Validation 60

3 Results 62

3.1 Sea Surface Temperature Calibration 62

3.2 Data Validation 65

4. Discussion 73

4.1 Image Calibration 73

4.2 Observation and Use Cases 78

5. Conclusions 83

Acknowledgements 86

References 86

CHAPTER 3 93

Abstract 93

1. Introduction 94

2. Methods 97

2.1 Study Site 97

2.2 Environmental Data 102

2.3 Satellite Data 103

3. Results 114

3.1 Region-wide Analyses 114

3.2 Sitewise Analyses 120

4. Discussion: 131

4.1 General Discussion 131

4.2 Shoreline Supply/Erodibility: C_0 133

4.3 Wave-induced transport: b 134

4.4 Wave Induced Transport of Turbidity: C_0 & b 136

4.5 Controls on transport extent and region wide turbidity 137

5. Conclusion: 140

Acknowledgements: 143
References 143
Appendix 150

Introduction

The ocean is vast and occupies most of our planet. However, the small nearshore zone is where most human interactions with marine waters occur. This zone where land meets ocean is resource-rich, highly productive, and serves as an economic hub across numerous sectors. Despite its importance, much remains unknown about the dynamics of nearshore waters that govern these regions. The nearshore, though relatively small, is characterized by great energy, driven by complex hydrodynamic interactions with landscapes that vary globally. These forceful and intricate dynamics make nearshore monitoring challenging, especially in regions where strong currents and land interactions create hazardous conditions, and the wide diversity of environments complicates holistic understanding.

These powerful mixing processes inherently leave marked imprints on the environment. When water moves, its integration into new areas is gradual, not immediate. Waters transitioning between zones of different temperatures create warm or cold tendrils along their paths. Rivers outflowing into the ocean bring nutrients, chemicals, and sediments from terrestrial sources, discoloring coastal waters. Waves, as they drag along varying seabed and crash onto shores, mobilize deposited sands, creating yellow-brown plumes. These "fingerprints" make these essential processes observable. Satellites capture these imprints as numerical data with optical sensors that orbit the planet. Remote sensing of these small yet influential features, especially when contextualized with large, continuous monitoring datasets, offers a promising methodology to constrain their controls across diverse coastlines. This is particularly true alongside ever-progressing spatial and temporal resolution of satellite data necessary to capture fine-scale, variable features. Northern California, with its great hydrodynamic diversity and wealth of environmental data, serves as an ideal observatory to better understand these processes. In this dissertation, I develop methodologies using these powerful datasets to resolve complex, fine-scale features in the nearshore.

In Chapter 1, I examine the dispersion of buoyant turbid freshwater plumes from the Russian River, California, as a representative system in Mediterranean climates. These plumes are smaller than those typically studied in river plume literature, making them more susceptible to varying environmental conditions and, therefore, less predictable. Despite their stature, these smaller plumes are more common and impactful in Mediterranean climate regions globally. I use 15 years of daily MODIS satellite image data alongside coincident environmental data to capture the complexity of these plumes and resolve the controls of their hydrodynamics. Using novel methodology in river plume remote sensing, I analyze the statistical relationship between water-leaving radiance, which serves as a proxy for surface suspended sediment concentration, and environmental data to characterize the dynamic controls on river outflow turbidity. This work serves as both a ground truth for recent computational models of smaller plumes and a presentation of previously undiscussed behavior, presenting insights into the interactions between river outflow, wave energy, ocean water level, wind conditions, and rotational forces in influencing plume dispersion trajectories.

In Chapter 2, I present a methodology to enhance the capability of nearshore monitoring through thermal infrared (TIR) satellite imagery. Many crucial nearshore mixing processes lack turbid visual signatures, making observation impractical with visible sensors, and are too small for traditional sea surface temperature (SST) satellites, leaving gaps in understanding nearshore temperature and chemical mixing processes. I develop a methodology to calibrate high-resolution (100m) Landsat TIR data, which is typically used for land observation, with traditional ocean-observing moderate resolution (1km) MODIS SST data, enabling observation of these features. In this methodology, I form a generalized calibration equation and validate these data with in-situ temperature measurements at different distances offshore and test its performance on data outside of the sample set to assess its general applicability. Validations show that this methodology significantly increases the accuracy of Landsat's thermal measurements from nearshore waters, surpassing MODIS SST accuracy and creating a dataset better suited for nearshore observation. The chapter highlights the potential of this enhanced dataset in revealing initial insights into fine-scale nearshore temperature mixing.

Finally, in Chapter 3, I explore the dynamics of nearshore surface turbidity by examining wave-driven cross-shore sediment transport outside the influence of freshwater. Wave orbitals create friction along the seabed, and their breaking imparts energy on the shoreline, mobilizing sediments and mixing waters in the cross-shore direction. Monitoring these highly energetic processes in-situ, especially in rocky environments, is challenging, resulting in significant knowledge gaps. Remote sensing offers a promising solution but isolating turbid water pixels from nearshore heterogeneity (e.g., foam and land) proves difficult. In this chapter, I employ novel machine learning segmentation methodologies to resolve nearshore heterogeneity in high-resolution satellite imagery, isolating red water-leaving radiances as proxies for sediment-laden turbidity. Coincident data from spatially distributed wave models and tide gauges allow for an examination of the impact of waves on turbidity across the entire region, with further investigation of their control on cross-shore turbidity at 31 specific sites. By comparing these results with bathymetric data of each site, I differentiate between characteristics of wave-driven sediment transport in sandy and rocky environments. The findings reveal that rip currents regularly transport sediments hundreds of meters to kilometers offshore. In rocky shores, rough bathymetries enhance sediment transport, but sufficient wave energy is necessary to initiate a turbid signature. In sandy environments, sediments are easily mobilized, but in the absence of rough bathymetry, wave energy is crucial for offshore sediment transport. Areas with both complex bathymetry and ample sediment supply facilitate the furthest offshore turbid signals. Transport extent is enhanced in low water level conditions. This chapter's novel application of machine learning segmentation to isolate relevant water reflectance, combined with the analysis of wave-driven sediment transport across diverse coastal environments, provides new insights into the complex, important dynamics of nearshore turbidity.

CHAPTER 1

Long-term observations of the turbid outflow plume from the Russian River, California.

Abstract

Understanding the mechanisms that spread freshwater away from small river systems and form turbid, low-salinity coastal plumes is crucial for assessing water quality in coastal waters. We present an analysis of 15 years (January 2004 to December 2018) of daily MODIS Aqua satellite data and in-situ instrument data on the turbid freshwater plume that forms off the Russian River (California, USA), a prototypical Mediterranean-climate, small mountainous river system (SMRS). We present per-pixel statistical metrics and regression analyses to identify and quantify the controls on the extent and configuration of the plume exerted by river discharge, waves, winds, and tides. While freshwater outflow exhibits a persistent signal in nearshore waters, a large-scale plume only extends offshore into coastal waters during high river flow, when plume turbidity can be detected more than 10km offshore from the river mouth. Our results show times when wave radiation stress exceeds outflow inertia, confining the plume within the surf zone and leading to an absence of detectable plume turbidity in coastal waters. Although tidal currents significantly influence the plume near the inlet, wind forcing is the primary control on plume shape and extent in coastal waters, deflecting the turbid outflow more than 30km upcoast or downcoast of the river mouth with respective wind directions. Coriolis forcing is also significant and observed most clearly during periods of high river discharge and low wind forcing. In addition to introducing novel remote sensing methodology for SMRS plume analyses, these findings highlight the complex interplay of forcing related to tides, river discharge, winds, and waves in shaping the behavior of SMRS plumes. New insights include the impact of tides on larger discharges, the role of Coriolis forcing in SMRS plumes, and the effect of cross-shore winds on plume compression. Further, by considering the Russian River as a model for SMRS, this study can be used to ground-truth existing

numerical models of small river plumes and to contribute to understanding critical for managing coastal water quality and nearshore ecosystems.

Keywords: MODIS, Coastal Oceanography, Hydrology, River Plumes, Turbidity, Sediment

1. Introduction

In coastal regions with dry summers and wet winters, outflow from small mountain river systems (SMRS) significantly influences the biogeochemical and geomorphic balances in coastal waters (Wheatcroft et al., 2010). These river systems (e.g. Russian, Gualala, Garcia, Navarro, Big, Noyo, Ten Mile, and Mattole Rivers in Northern California, USA) are characterized by small river basins (<2 x 10^4 km^2) and high relief (>1000m). Outflow fluctuates between near-zero summer discharges (order 1 m^3s^{-1}) and winter discharges several orders of magnitude higher (order 1000 m^3s^{-1}), transporting seasonal concentrations of sediments to the coastal ocean, exacerbated by interannual drought and flood cycles (Wheatcroft et al., 2010).

In Mediterranean-climate regions like Northern California, sediments from these outflows supply over 80% of the sediment to littoral cells (Griggs and Hein, 1980; Runyan and Griggs, 2003). Coarse sediments in these outflows deposit quickly nearshore, contributing to the cycle of shoreline morphodynamics (Warrick, 2020). Finer sediments remain suspended in a surface freshwater layer (or plume) that can travel hundreds of kilometers alongshore (Warrick et al, 2007). These suspended particles increase water turbidity, affecting both light attenuation through the water column and acting as a tracer for sorbed riverine pollutants.

Despite the significant role of SMRS outflow, most research has focused on larger river systems and small constructed engineered outflows (see discussions in Basdurak et al., 2020). This research gap is important because SMRS differ significantly from these systems in terms of discharge and plume dynamics. SMRS have lower average discharges than larger rivers, making their plume trajectories more dependent on variable environmental forcings rather than the classical, constant buoyancy-rotation balance (Horner-Devine et al., 2015). At the same time, SMRS outflows are more stratified and less dependent on jet dynamics compared to engineered outflows (Basdurak et al., 2020). SMRS discharges also vary significantly, reflecting values that fall between those of larger river systems and engineered outflows.

Recent studies have begun addressing plumes from SMRS, primarily using computational models, with few utilizing remote sensing or in-situ observations. Remote sensing and observational research are crucial for validating the results of computational models, (see section 1.1). Remote sensing studies typically use the light reflectivity of coastal waters as a proxy for the concentration of suspended particles in river plumes. These studies can be broadly categorized based on the spatial and temporal resolution of remotely sensed data. High spatial resolution studies make use of imagery from Unmanned Aerial Vehicles (UAVs) and fine-resolution satellites like Landsat 5-9 and Sentinel-2. However, these studies are often limited in temporal scope due to the logistical challenges of UAV sampling and the infrequent repeat overpasses of high-resolution satellites. In contrast, low spatial resolution sensors (e.g., SeaWIFS, MODIS) benefit from more frequent data but lack fine-scale spatial resolution and prior works tend to focus on statistical metrics like mean and standard deviation rather than more nuanced statistical tests such as correlation and regression, thus overlooking the variability common in small plumes. Moreover, much of this work predates recent findings on the significant impacts of waves (Rodriguez et al., 2018, Kastner et al., 2019) and tides (Basdurak et al., 2020) on smaller plumes. Computational studies often focus on a specific mechanism, thus precluding a more holistic view of plume dispersion mechanics.

This study aims to enrich understanding of SMRS plume dispersion by observing turbid outflow from the Russian River in northern California (USA), with a prototypical, seasonally variable hydrograph. We validate and enrich numerical models across river plume literature by using updated techniques to compare nearly two decades of remote sensing data from MODIS with coincident data on waves, tides, and river discharge. Our geospatial results not only align with existing models across various plume sizes but also reveal previously unexplored controls on plume shape and the fate of freshwater outflow. We show that the seasonality of discharge in the Russian River SMRS results in plumes that exhibit behaviors consistent with "small" plumes during low flows (plume controlled by wave and wind conditions) and "large" plumes during high flows (plume controlled by buoyancy and Coriolis effects).

Our primary objectives are (i) to identify and quantify the spatial configuration of small river plumes subject to wind, wave and tidal forcing, (ii) to develop and deploy new methodologies in river plume remote sensing (iii) to validate and enrich prior simulation models of plumes, and (iv) to contrast controls on "large" Coriolis-influenced plumes to controls on "small" river plumes.

1.1 River Plumes

River plumes are bodies of freshwater that flow from a river into another body of water, such as lakes or the ocean. When entering marine waters, these plumes often form a relatively thin layer of freshwater that is stratified at the surface due to its higher buoyancy compared to denser, saline ocean water (Horner-Devine et al., 2015). Large and small plumes are often delineated by the degree to which the trajectory of their dispersion is dependent on rotational Coriolis forces (Horner-Devine et al., 2015; Basdurak et al., 2020). This relationship is explored by Garvine, 1995, where large and small plumes are classified by a non-dimensional Kelvin number K:

$$K= \frac{\gamma L}{(c/f)} \qquad \text{eq. 1}$$

Where γ is plume thickness, L is the alongshore length of the plume, c is the internal wave phase speed, and f is the coriolis parameter. "Large" plumes occur where Coriolis is dominant

(K>>1) and “small” plumes occur where Coriolis effects are dominated by inertia and buoyancy effects (K<<1). Typical large-plume patterns and outflow trajectories are well documented (Horner-Devine et al., 2015). As the low-density outflow leaves the outlet, it enters the near-field plume region where transport is driven by outflow momentum. Eventually, the plume lifts from the seabed at the critical Froude number (Armi and Farmer, 1986) marking the mid-field region, where dispersion of the buoyant plume layer is shaped by an interplay between buoyancy (Hetland, 2010), wind (Rennie et al.,1999; Lentz and Largier, 2006; Horner-Devine et al., 2009), Coriolis (Horner-Devine et al., 2015), and discharge (Fong and Geyer, 2002; Horner-Devine et al., 2009). The influence of Coriolis results in an anti-cyclonically rotating “bulge”, which scales in size with discharge rate and duration (Horner-Devine et al., 2009). Beyond the bulge is the far-field where transport is no longer controlled by discharge and the buoyant plume layer travels alongshore as a shore-attached coastal buoyancy current. Both the mid- and far-field regions of the plume can be impacted by winds and currents. Upwelling increases the extent of the bulge and induces thinning in the plume; downwelling winds cause opposite effects (Fong and Geyer, 2001; Lentz and Largier, 2006; Horner-Devine et al., 2009). While sufficiently strong winds can overcome Coriolis effects in large plumes (Pullen and Allen, 2000; Horner-Devine et al., 2009), this is more common in small plumes (K<<1) that are less susceptible to Coriolis effects (Basdurak et al., 2020; Basdurak and Largier, 2022).

Some recent publications highlight the role of wave forcing (Wong et al., 2013; Rodriguez et al., 2018; Kastner et al., 2019). Depending on the balance between estuary outflow, tidal influences, and breaking wave momentum, river water can be partially or fully trapped in the surf zone. Rodriguez et al., (2018) model the balance of momentum (p) between breaking waves and river discharge with the following equation:

$$\frac{S_{xx}^{b}}{\rho_0 \beta L_{sz}} \frac{A^2}{Q^2} = p \qquad \text{eq. 2}$$

where Q is river discharge, S_{xx}^{b} is wave radiation stress, βL_{sz} is the water depth at the breaking point, ρ_0 is the background density of ocean water, and A is the cross-sectional area at the river or estuary mouth. As p increases, more freshwater is trapped in the surf zone. Given a high enough value of p, river outflow becomes completely trapped and is transported alongshore in the surf zone until later dispersed offshore by rip currents (Clarke and Largier, 2007).

When outflow momentum dominates and river water escapes the surf zone, dispersion pathways can still be influenced by waves and tides. Basdurak et al., 2020 shows that small plumes are deflected up and down coast from the estuary mouth by alongshore tidal currents. Other works model the role of wave breaking in turbulent mixing that can slow near-field advection and far-field dispersion (Gerbi et al., 2013; Thomson et al, 2014).

1.2 Site Description

This study focuses on outflow from the Russian River (California, USA) a prototypical small mountainous river system (SMRS) in northern California (*Fig. 1*) that is representative of outflows from mountainous coasts worldwide. The mouth of the river is about 90 km north of San Francisco, and the 180-km long river drains a 3850 km^2 watershed subject to intense rainfall events in winter (i.e., atmospheric river events). Winds are seasonal, with persistent strong northerly winds driving coastal upwelling in spring and summer (April to June), southerly wind events during winter storms (December to February), and weaker winds in the fall (August to October) as described by Garcia-Reyes and Largier (2012).

At the mouth of the Russian River is a bar-built estuary that is intermittently closed off from the ocean by a wave-built sand barrier (Behrens et al., 2013). Adjacent to the mouth of the estuary, the shores are rocky, and waters are designated as a Marine Protected Area. During high precipitation events, river discharge exceeds 1000 m^3/s, but during low discharge conditions (~4 m³/s) water enters and exits the estuary mouth tidally. Comparable conditions exist in many other northern California estuaries.

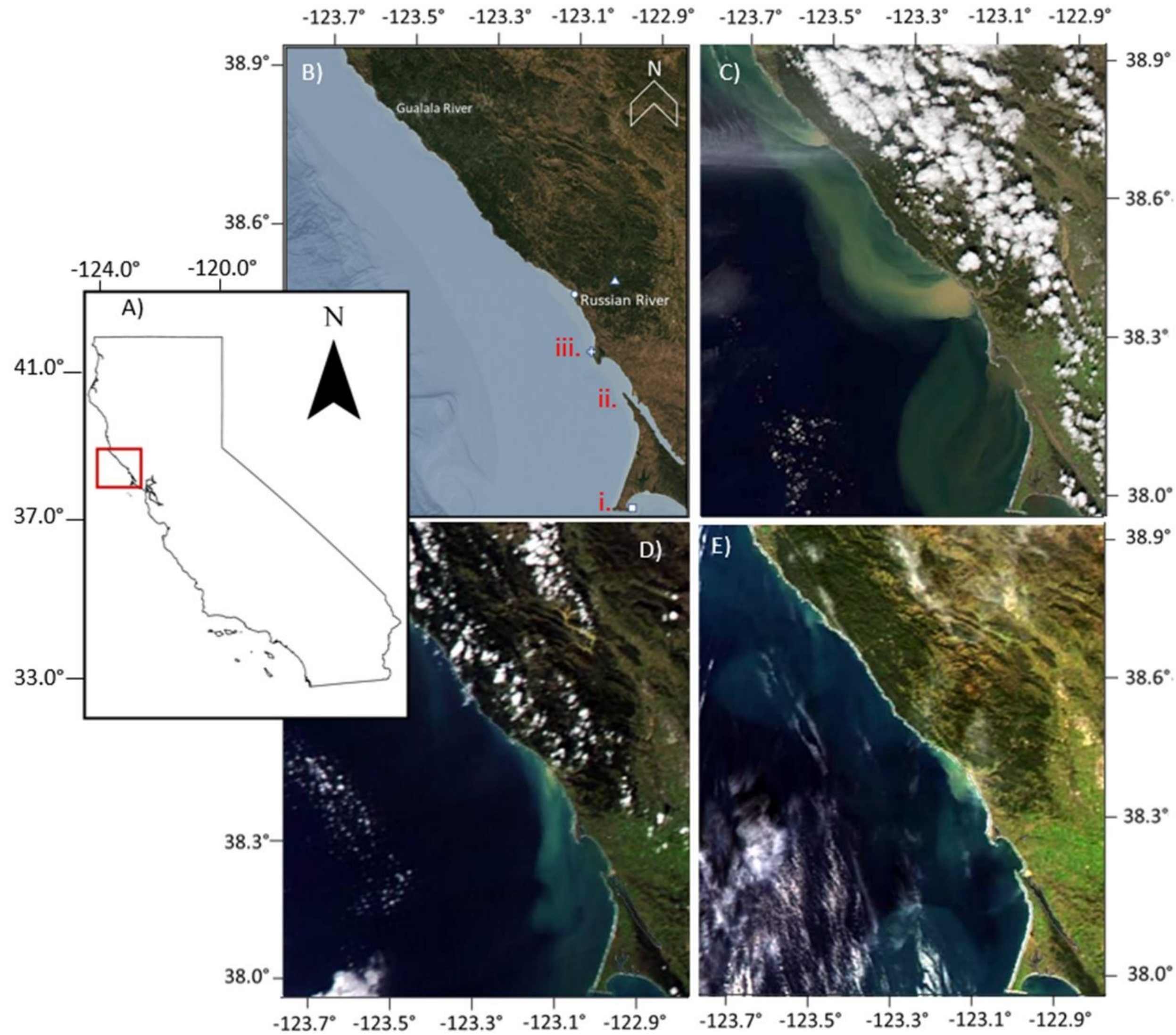

Fig. 1. (A) Map of California, USA, study site highlighted by red box (B) Map of study site and data sources (● = Russian River Inlet & CDIP MOP wave energy location, ▲= USGS River Gauge #11467000, + = BOON wind observatory, ■ = NOAA Tide Gauge Station #9415020). Roman numerals mark (i) Point Reyes, (ii) Bodega Bay and Tomales Bay, and (iii) Bodega Head. (C-E) Examples of turbid river plumes from MODIS true color images: (C) 28 February 2019, (D) 28 February 2017 and (E) 28 February 2008.

2. Methods

This study uses daily satellite data and concurrent data on river flow and environmental conditions. Data on river discharge (Q), wind (W), ocean water level (WL), river turbidity (T), and wave height (Hs) are available from 2004 to 2019. Environmental data are binned in intervals preceding each satellite overpass: W, T, Q, and Hs are averaged over the preceding 24 hours while WL is averaged hourly.

2.1 Environmental Data

Winds: Wind direction and magnitude at Bodega Head were observed with a 4-blade helicoid propeller and wind vane from May 2001 to May 2014, and with a 2-axis ultrasonic anemometer after May 2014 (BOON; https://boon.ucdavis.edu/). Daily wind direction was classified in quadrants relative to the shoreline orientation of 315°: winds blowing from directions between 90° and 180° are classed as "upcoast", between 0° and 90° as "off-coast", between 270° and 360° as "downcoast", and between 180° and 270° as "on-coast". The daily alongshore wind component is calculated from daily wind speed and direction at an orientation of 315° (i.e., downcoast winds have positive magnitudes) and the cross-shore wind component is calculated for an orientation of 225° (i.e., on-coast winds have positive magnitudes). Wind data were averaged for the 24 hours prior to the satellite overpass (zero lag), or for 27-3 hours prior (3-hr lag), or for 30-6 hours prior (6-hr lag). Correlations with greater lag have previously been found to yield stronger relations between plume behavior and wind stress (Geyer et al., 2000; Warrick et al., 2007).

Tides: Water level data were used to index tidal phase at the time of each satellite image. Data referenced to MLLW were obtained from the tide gage at Point Reyes (National Oceanic and Atmospheric Administration gage #9415020), which is known to represent tides at the Russian River mouth with negligible phase and amplitude differences (J.L. Largier and D.S. Behrens unpublished data). Water level data are hourly averaged and matched with the time of image capture time rounded to the nearest hour.

River Discharge and Turbidity: Russian River discharge and turbidity data were collected at Hacienda Bridge (United States Geological Survey gauge #11467000), approximately 18.5km upstream of the mouth. Quarter-hourly discharge values are available from October 1987 onward, and turbidity data are available since June 2008. Turbidity is measured in FNU units with a monochrome near-infrared LED light (780-900nm) at a detection angle of 90° ± 2.5^{o}.

Waves: Daily average significant wave height H_s at the 10m isobath adjacent to the Russian River mouth (*Fig. 1*) are available from the Coastal Data Information Program (CDIP; https://cdip.ucsd.edu/). These values are generated using a linear, spectral refraction wave model driven by observations at offshore wave buoys (O'Reilly et al., 2016). Radiation stress (S_x^b) is calculated by assuming that phase velocity equals the group velocity in shallow nearshore waters:

$$S_{xx}^b = E = \rho_0 \, g \, H_s^2 \qquad \text{eq. 3}$$

where E is the mean-depth wave energy density per unit horizontal area and g is gravitational acceleration.

Daily average S_{xx}^b and Q were used to calculate a daily value of p (Eqn 2). The value of βL_{sz} is approximated by depth d. This depth is estimated using the theoretical equation from Miche (1944) where the depth-limited breaking of a solitary wave occurs at a critical value of $H_s/d = 0.781$ (Kastner et al., 2019). The cross sectional-area (A) is assumed to be 100 m^2, consistent with the average dimensions of the inlet channel at the Russian River mouth (Behrens et al., 2013).

Mouth State: Daily observations of the state of the Russian River mouth are available from 2004 to 2019, allowing classification as open or closed (Behrens, 2013; Largier et al., 2020; Winter, 2020). These data were extracted from a daily photograph record.

2.2 Satellite Data

Ocean color data were collated for every MODIS Aqua image captured for the study region (38.95°- 37.99°N, 123.75° - 122.85° S) between January 2004 and December 2018, aligning with daily Russian River inlet-state data. Daily MODIS L1A files were downloaded from NASA's Ocean Color website (http://oceancolor.gsfc.nasa.gov/) and subsequently processed to L1B and L2 surface reflectance data (*Rrs*) using the SeaDas (SeaWIFS Data Analysis System, version 8.1.0, Baith et al., 2001).

Atmospheric correction was performed using the NIR-SWIR (Near Infrared Radiation-Shortwave Infrared Radiation) algorithm by Wang et al., (2009). Traditional atmospheric correction methods rely solely on NIR bands (748 and 869 nm), but these are not suitable for turbid water conditions. Hence, the Wang et al., (2009) method switches from NIR to SWIR (1240 and 2130nm) correction for pixels detected as turbid by an index (Wang et al., 2009; Saldías et al., 2012). We used a pixel size of 500m rather than 250m to resolve heterogeneity in imagery pixels that arise from issues such as sun glint (Aurin et al., 2013).

Surface reflectance from the 645nm band (Rrs_{645}) is an accepted proxy for surface turbidity due to suspended sediments, based on correlations in prior studies (e.g., Lahet and Stramski, 2010; Saldías et al., 2016). We validate this relation for our study site by finding the Spearman non-linear correlation coefficient between Rrs_{645} and hourly average turbidity measured at the Hacienda Bridge gage, 18.5 km from the river mouth. We do this independently for each pixel for an image time series from June 2008 to January 2019. Spearman Rho values are 0.8 at the mouth, demonstrating that reflectance is an effective turbidity metric, and above 0.7 for locations up to

4.5km offshore of the mouth (Fig. 2), despite the spatial offset and potential for changes in turbidity between the river gauge and pixels in coastal waters.

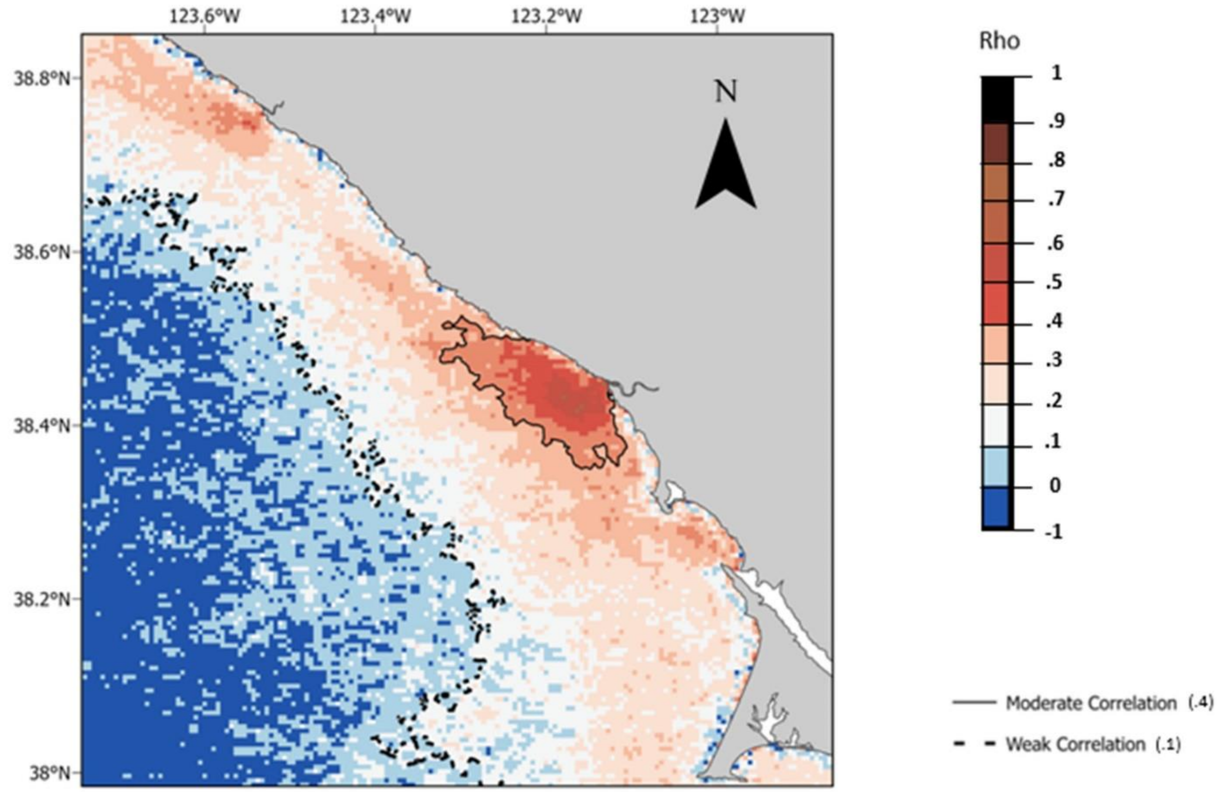

Fig. 2. Map of pixel-wise Spearman's rho correlation coefficients between hourly-average measured turbidity from USGS gauge #11467000 and coincident Rrs_{645} at each pixel position.

2.3 Plume Detection

To isolate river plume effects on ocean turbidity apart from other processes (e.g., phytoplankton blooms, wave-driven resuspension, rip currents, white capping), we examine the distribution of turbidity values in coastal waters on dates when the river inlet was observed as closed. We determined a threshold value of 0.59 x 10^{-3} Sr^{-1} for non-plume turbidity by calculating the 97th percentile value of Rrs_{645} values for all pixels 1.5km offshore across 1371 images captured when the Russian River inlet was closed (*Fig. 3)*. This threshold assumes that in the absence of sediment-laden freshwater, the ambient Rrs_{645} reflectance of oceanic waters is much less than reflectance values associated with the plume. Therefore, the maximum non-freshened values would represent the highest condition before Rrs_{645} is elevated by freshwater sediment influence. The 3% of values exceeding this threshold are likely due to occasional wave-driven events that cause resuspension and circulation, exporting nearshore turbidity offshore (Speiser et al, in preparation). Nonetheless, even these high values rarely exceed 1.0 x 10^{-3} Sr^{-1}, which is an order of magnitude lower than typical plume turbidity values (Fig. 4). Similar thresholding methodologies have been applied in other river plume remote sensing studies, although without the advantage of an estuary closure (for example, Saldías et al., 2012; Mendes et al., 2014; Saldías et al., 2016)

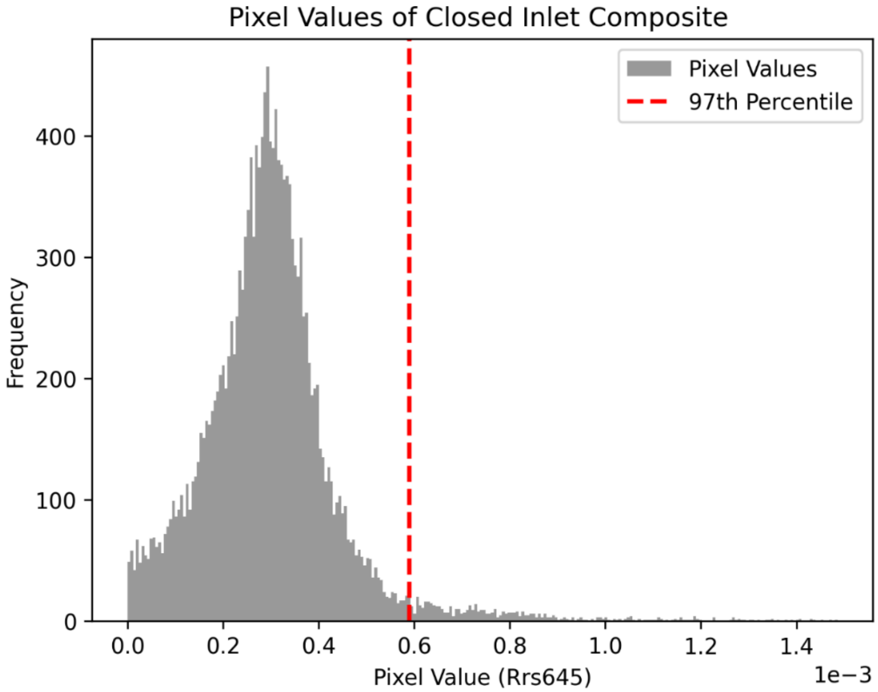

Fig. 3. Frequency histogram of the average Rrs_{645} at all pixels 1.5 km offshore from all MODIS images on days when the Russian River mouth was closed. The red line marks the 97th percentile value, 0.59×10^{-3} Sr^{-1}.

2.4 Regression Analysis

To evaluate the influence of different environmental drivers on plume behavior we calculated Spearman's Rho non-linear regression correlation coefficients between coincident environmental data (i.e., *W, Hs, WL, Q*, and *T*) and turbidity proxy values Rrs_{645} at each pixel position across the study region. We used statistical tests (pixel correlations) instead of pixel mean or median to differentiate between different processes that occur simultaneously. Further, by evaluating per-pixel regression we can identify spatial patterns in processes controlling plume presence. Spearman's rho ordinal rank correlation was chosen over linear regression as pixel values are altered simultaneously by other drivers and Spearman does not require linear relationships. For instance, the turbidity of a pixel may be strongly influenced by river discharge, but transport to that specific position may be diminished or enhanced by processes such as wind-driven transport, altering the pixel Rrs_{645} value. Further, Spearman's rho correlation coefficients are less impacted by outliers, which are caused by non-observed variables, thus highlighting relationships with the tested variable.

To assess the strength of correlation we adopt the classes outlined by Schober et al.,(2018) – Table 1. To demarcate spatial extent of the correlation, contours are drawn to encompass the mouth of the Russian River. If a contour does not surround the river inlet, it is not highlighted. The value ranges for these classes are determined to the second decimal (i.e., 0.394 falls in the "weak correlation class", while 0.395 is rounded to 0.40 and falls in the "moderate correlation" class). This approach precludes attention on features due to other river outflows or wave-driven rip-current features.

Absolute value of Rho	*Interpretation*
0.00-0.10	Negligible Correlation
0.10-0.39	Weak Correlation
0.40-0.69	Moderate Correlation
0.70-0.89	Strong Correlation
0.90-1.00	Very Strong Correlation

Table 1: Correlation strength classes from Schober et al., 2018.

3. Results

3.1 Nearshore Trapping of Plume

As found by Rodriguez et al.,(2018), wave radiation stress can stall or fully trap the outflow jet, precluding the formation of a plume beyond the nearshore (surf zone and rip-current zone), which is the focus of this paper. Thus, instead of using a minimum daily average discharge as a qualifier for images used in plume analyses (e.g. Saldías et al., 2012; Mendes et al., 2014; Fernandez-Novoa et al., 2015; Saldías et al., 2016), we use a qualifying threshold based on daily average p value. For all images when the Russian River inlet was open (n=3419), we calculated the daily average p and divided the dataset into deciles. For each decile, we created an average image. Only the lowest four p-value deciles exhibit reflectance values 1 km offshore that exceed the plume turbidity threshold. The 1km location was chosen to mitigate any influence of subpixel constituents such as land, sea stacks, boulders, and white water and foam lines generated by breaking waves. We thus use p = 41 as the upper bound for images used in our evaluation of the offshore turbid plume (a total of 1357 images). This is the lower bound of the 4th decile (not the average p value 109), i.e., only the three lowest deciles are used in the analysis. The distributions of available pixels across these images are mapped in Fig. 4., with an average of n=498 values at each pixel position, a minimum of n=27 and a maximum of n=650.

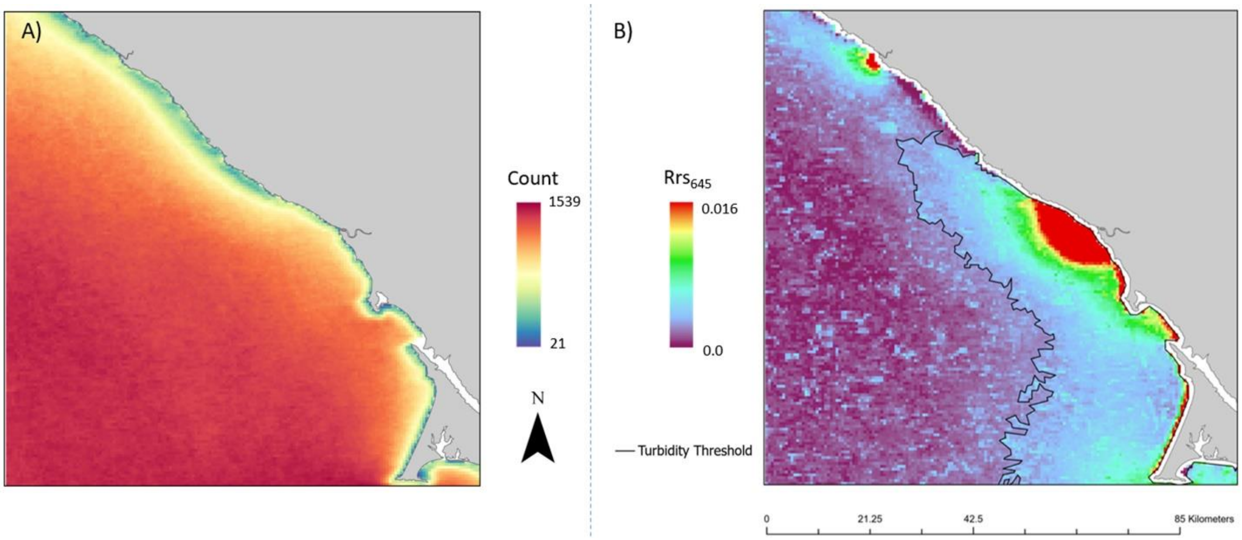

Fig. 4. Mapped statistics of dataset images when plume breaks through surf zone (A) Count of available values at each pixel position. (B) Pixel-wise average of Rrs$_{645}$, ranging from 0.0 to .016 Sr^{-1}. The black line is the contour where average Rrs$_{645}$ equals plume turbidity threshold value of 0.59 x 10^{-3} Sr^{-1}.

3.2 Average Plume Pattern

The shape of the turbid plume exiting the Russian River can vary significantly (Fig. 1). However, there is a clear zone of elevated turbidity in the 1357-image average field that extends about 10 km upcoast, downcoast and offshore of the mouth (Fig. 4), encompassing the near-field and mid-field of most plume patterns. The far-field evidently varies across wind conditions with no clear pattern in the average. Further, other sources and processes are evident beyond 10 km, including outflow from the Gualala River (38.7° N), Tomales/Bodega Bay freshwater sources (38.2° N) and nearshore zones along wave-exposed beaches on the north shore of Bodega Head (38.3° N) and Point Reyes (38.1°N). The average alongshore (upcoast plus downcoast) extent of turbidity above the plume threshold increases with discharge rate, from 14 km for lowest discharge quintile to 54 km, 65 km, and 77 km for second through fourth quintiles, respectively. For the fifth discharge quintile, elevated turbidity from the Russian River merges with multiple sources in the region (cf., plume coalescence outlined by Warrick and Farnsworth 2017). Average offshore extent is small for low discharge (3 km) but pushes significantly further offshore for higher discharge (8 km, 10 km, and 14 km for the second through fourth quintiles, respectively). The plume area encompassed by the turbidity threshold contour increases from 20 km^2 for low discharges to 180, 298, and 698 km^2 for second, third, and fourth quintiles, respectively.

3.3 River Discharge Effects

As river outflow increases, a larger area of turbid water is observed in coastal waters off the Russian River mouth. This plume-affected zone is demarcated by high Spearman correlation values at pixels where Rrs_{645} turbidity increases with increases in river discharge Q. The spatial distribution of correlations mapped in Fig. 5 shows moderate correlations (greater than 0.4) in a zone extending 11 km offshore of the mouth and 30 km alongshore (darker colors enclosed by moderate correlation contour), both upcoast and downcoast of the mouth – but notably detached from the shoreline south of the mouth. The highest correlation (rho = 0.71) is about 4km offshore of the Russian River mouth (Fig. 5) – lower correlations are found in persistently turbid nearshore waters. This core zone is strongly and predictably impacted by changes in river discharge, but there is an extensive zone of weaker correlations that is continuous through the study area from Point Reyes to Point Arena. The weak-correlation contour is found about 25 km offshore, indicating that discharge-related elevated turbidity extends over the entire shelf during times of high flow in the Russian River, although including multiple sources with correlated outflow following rain events.

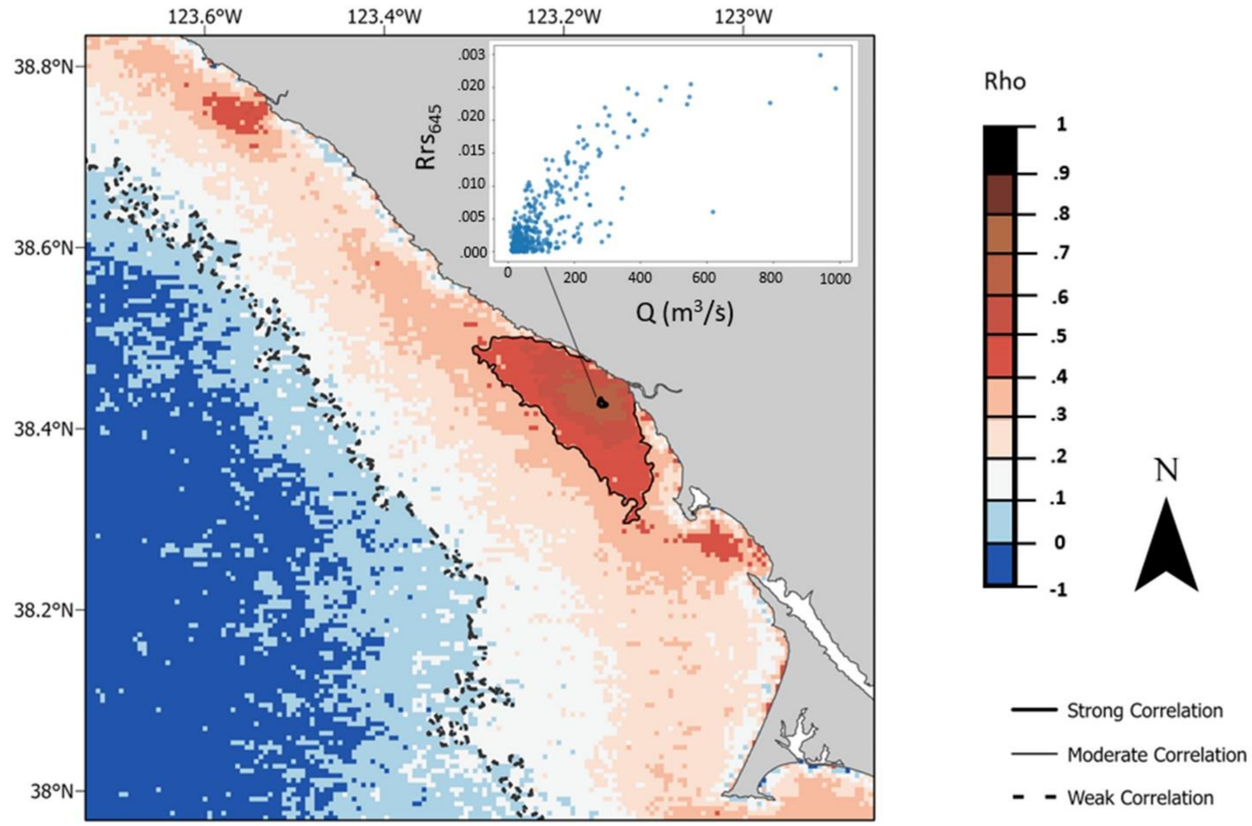

Fig. 5. Pixel-wise correlation coefficients between Rrs_{645} and coincident daily average discharge (Q) values for all dates with visible plumes (average Q is 156.52 m^3/s). The weak correlation (rho) threshold (rho = 0.10) and moderate correlation threshold (rho = 0.40) are shown; only a few pixels exceed the strong correlation threshold (rho = 0.70). The inset graph shows Rrs_{645} values (y axis) versus daily discharge values (x axis) for the pixel position with the highest correlation (rho = 0.71).

Anticipating different plume behavior during high-discharge events and low-discharge events, pixel-wise turbidity-discharge correlations were calculated separately for each daily-average-discharge quartile (Fig. 6, panel c.). With highest river flow, the zone of moderate correlations is found primarily on the upcoast (north) side of the river mouth, pushing 18 km offshore, and separated from the coast. At the center of this zone, the maximum correlation is 0.83. While weak correlations extend over the whole shelf region, elevated correlations are observed in Bodega Bay where turbid outflows include Tomales Bay and Estero Americano (Fig. 1) and at the bottom of the frame where turbid waters flow north from the Gulf of Farallones (Largier et al., 1993; Kaplan and Largier, 2006). For plumes when discharge is in the second highest quartile (Fig. 6, panel c.), correlations are weaker but elevated values are again skewed to the upcoast side. The weak-correlation contour no longer extends over the shelf, and it is centered on the Russian River mouth, extending about 30 km upcoast and about 10 km downcoast separated from the coast. While a coherent zone of correlation is evident for the second lowest quartile (Fig. 6, panel b.) and weak correlations extend about 30 km alongshore and 15 km offshore, the correlation zone is notably weak for the lowest quartile discharge (Fig. 6, panel a.). While turbid plumes are observed on these low-discharge days, the shape and size of the plume is more variable, altered by tidal state (section 3.5) and wind forcing (section 3.4)

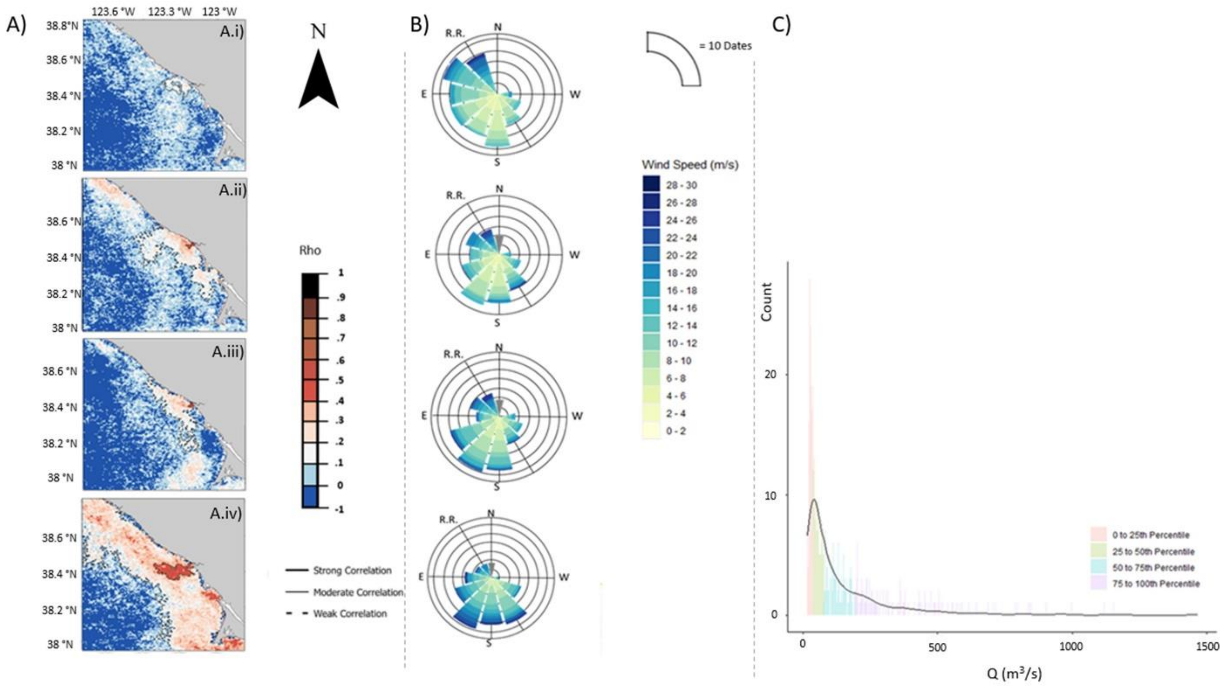

Fig. 6. (A) Pixel-wise correlation coefficients between Rrs$_{645}$ and coincident daily average discharge (Q) values calculated separately for discharge quartiles from low to high (panels A.i-A.iv). (B) Wind roses corresponding to each quartile. The "RR" line indicates shoreline orientation at the mouth of the Russian River. Wind direction is in meteorological convention (i.e., direction from which the wind blows). (C) Histogram showing the discharge for each quartile; colors of bars correspond to respective discharge quartiles 0-25th percentile (16 to 42m^3/s); 25th-50th percentile (42 to 84m^3/s); 50th-75th (84-203m^3/s); 75th to 100th percentile (203 to 2366m^3/s)

Wind forcing shows a correlation with discharge rate (Fig. 6), with more southerly winds during higher discharges and more northerly winds during lower discharges. To preclude the influence of wind on plume behavior, we also calculate pixel-wise correlation between Q and Rrs_{645} for calm days (wind speeds in the lowest quartile, which is less than 6.5 m/s). In the absence of strong wind effects (Fig. 7), correlations are higher (compare with Fig. 5), exhibiting a zone of strong correlation reaching 6 km offshore and 5 km upcoast. The maximum correlation coefficient is rho = 0.81. The moderate-correlation contour also exhibits marked asymmetry, extending ∼20 km upcoast and ∼5 km downcoast.

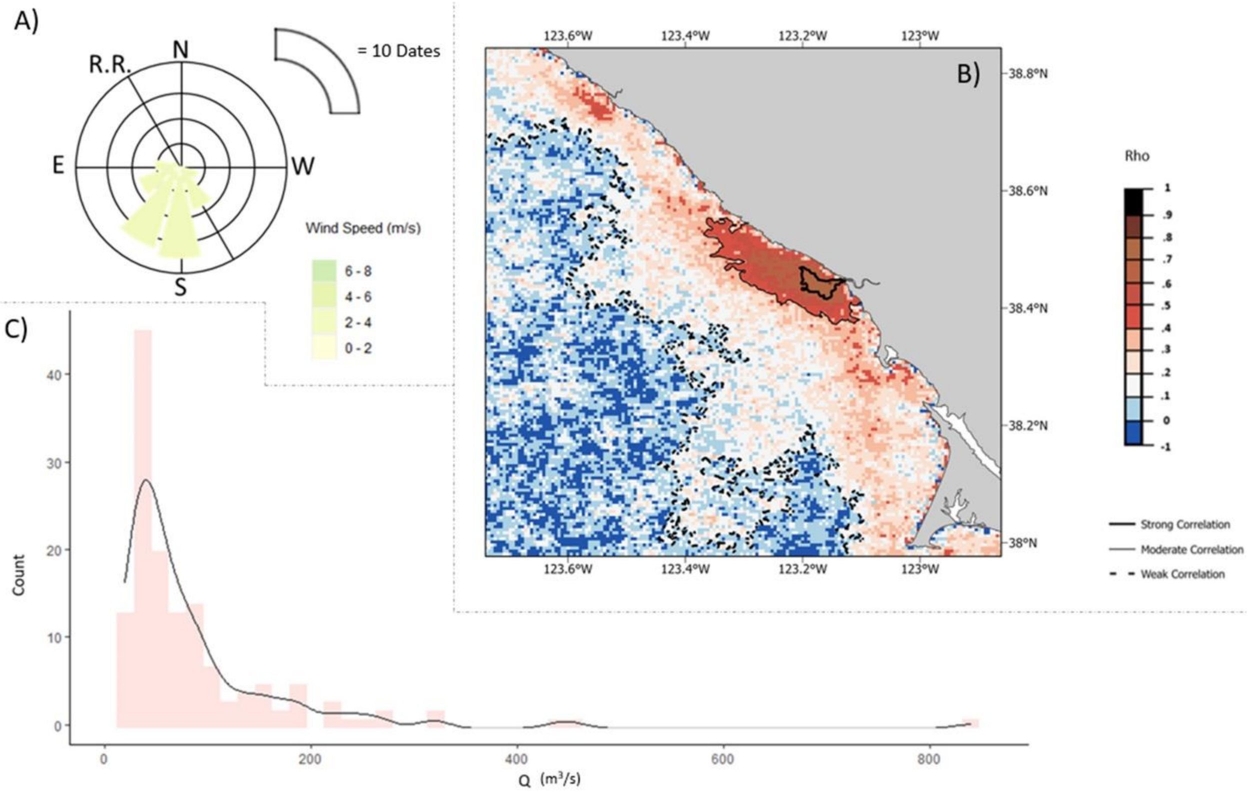

Fig. 7. (A) Pixel-wise correlation coefficients between Rrs_{645} and coincident daily average discharge (Q) values for days with weak winds. (B) Wind rose representing data from the subset, with wind direction in meteorological convention. (C) Histogram depicting discharge rates for this subset.

3.4 Wind Effects

To explore wind effects on plume behavior we calculate discharge-turbidity relationships for different daily average wind direction (Fig. 8), and we calculate correlations between turbidity and wind speed in each of four quadrants (upcoast, downcoast, onshore, offshore) irrespective of discharge but with $p < 41$ as before (Fig. 9).

When the wind blows from the southeast (upcoast quadrant), turbidities increase markedly on the north side of the river mouth during high discharge, with a coherent band of strong correlation extending about 12 km upcoast from the mouth and separate from the shore. However, the broader zone of moderate correlation is attached to the shore and extends over 30 km upcoast (Fig. 8). When daily average discharge is shifted 3 hours earlier (i.e., discharge averaged from 27 hours to 3 hours before the satellite image), or 6 hours earlier, maximum correlations are similar, but the zone of moderate correlation extends further upcoast, increasing from 33 to 39 km consistent with an upcoast propagation rate of 0.28 m/s. Under these upcoast winds, significant discharge-turbidity correlations are also seen emerging from Bodega Bay sources and extending north from the Gulf of Farallones where outflow from San Francisco Bay enters the ocean – these turbidity signals also reach further north with increased lag between discharge and turbidity. In contrast, when the wind blows from the northwest (downcoast quadrant), turbidities increase markedly on the south side of the river mouth, although no pixels exhibit strong correlation. The 30 km zone of moderate correlation extends to Bodega Bay, but remains detached from the shore, consistent with active upwelling driven by NW wind stress and persistent nearshore turbidity along the north shore of Bodega Head. It is interesting to see this zone extending into Bodega Bay, most likely due to merging with turbidity from sources in Bodega Bay and Tomales Bay (cf., Fig. 1). The absence of discharge-correlated turbidity north of the mouth during NW winds shows that the upcoast configuration of the plume requires high discharge (Fig. 6) and/or weak winds (Fig. 7) – conditions under which Coriolis forcing is expected to be important.

Onshore and offshore winds also influence the shape of the plume (Fig. 8). During onshore winds (on-coast), only pixels near the mouth exhibit moderate or strong correlations, illustrating compression of the plume on the shore and limited alongshore plume propagation. Further, in contrast to the no-wind case (Fig. 7) there is no upcoast tendency. With increasing lag between discharge and turbidity, the moderate-correlation plume zone is further reduced in offshore extent, decreasing from 12 to 9 and 8.5 km, respectively. At the same time, the shelf-wide weak correlations are compressed from 32 to 14 and 12 km, respectively. In contrast, offshore winds (off-coast) result in a continuous band of high discharge-turbidity correlations along the coast, although there is notable small-scale spatial heterogeneity with adjacent pixels exhibiting different values.

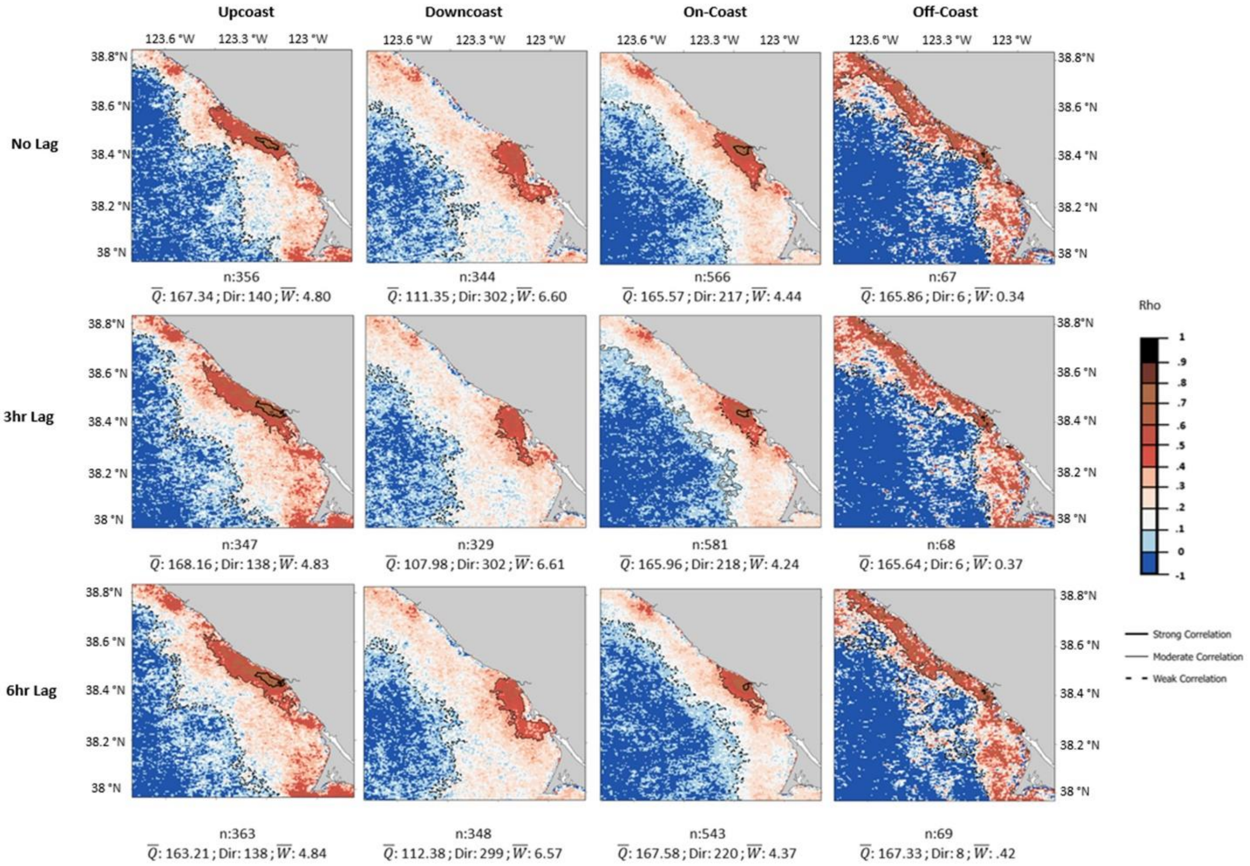

<u>Fig. 8.</u> Pixel-wise correlation coefficients between Rrs_{645} and coincident daily average Q values calculated separately for different wind directions (columns) and time lags (rows). The number of images in each subset (n) is listed beneath each image, along with information on average discharge (Q in m^3/s), average wind direction (Dir), and average wind speed in the subset (W in m/s). <u>Columns, left to right</u>: Daily average upcoast winds, downcoast winds, onshore winds, and offshore winds; <u>Rows, top to bottom</u>: no lag, 3 hours lag, 6 hours lag.

The second analysis of wind influences on the plume addresses the correlation between turbidity at a given pixel and wind speed – calculated separately for four wind vector directions: upcoast, downcoast, onshore, and offshore. While discharge is not a factor, all data are from days when discharge is significant (i.e., the plume is not trapped in the surf zone, $p < 41$). Again, we calculate correlations for wind averaged over the day preceding the satellite overpass, and for daily average wind shifted 3 hrs and 6 hrs earlier. In all cases, the correlation with wind (Fig. 9) is notably weaker than correlation with discharge (Figs. 5, 6, 7, 8), but the weak correlations describe coherent patterns in plume response to wind forcing.

On days with stronger upcoast winds, turbidity is higher in a zone extending upcoast from the mouth of the Russian River (Fig. 9, left panels). Evidently, this response to wind forcing takes time as the 3-hr and 6-hr lagged results show higher correlations and a better-defined plume zone. For zero lag, there is no response south of the mouth, but this is not the case for 3-hr and 6-hr lags, with significant correlations on the north side of Bodega Head, within Bodega Bay and around Point Reyes (likely explained by other turbid waters being advected northward during these upcoast, downwelling favorable winds). In contrast, turbidity increases south of the mouth on days with stronger downcoast winds, forming a 42-km-long continuous zone from the mouth of the river to Point Reyes (Fig. 9 second column), becoming more marked with 6-hr lag due to stronger negative correlations offshore. Correlations are low nearshore, specifically along the north coast of Point Reyes, which is persistently turbid due to wave-driven resuspension. During these NW winds, a marked zone of negative correlation is evident north of the mouth, indicating that turbid plume waters are less likely to be there with stronger downcoast winds, i.e., the upcoast plume pattern found on calm days and during upcoast winds is weakened or prevented by downcoast winds that are strong enough. Negative correlations west of Point Reyes similarly indicate that NW winds preclude upcoast propagation of turbid waters from the Gulf of Farallones. These results are all for periods when there is significant discharge from the Russian River (average Q ~ 130 m^3/s), which is not typical of the summer upwelling season.

Onshore winds also have a direct effect on turbidity, with higher turbidity observed near the river mouth with stronger onshore winds (Fig. 9 third column). This zone is centered on the mouth and strongest at the mouth. Correlations weaken with lag, indicating that the response to onshore winds is quicker than the response to alongshore winds. There is little correlation of turbidity with offshore winds at zero lag (Fig. 9 right panels). However, there is a marked nearshore zone extending north from the river mouth for images lagged 6 hours, representing increased turbidity in the upcoast plume zone with increased offshore winds, which may represent a surface Ekman response. There is a similar zone of increased turbidity in the Gulf of Farallones, south of Point Reyes (i.e., just north of the mouth of San Francisco Bay).

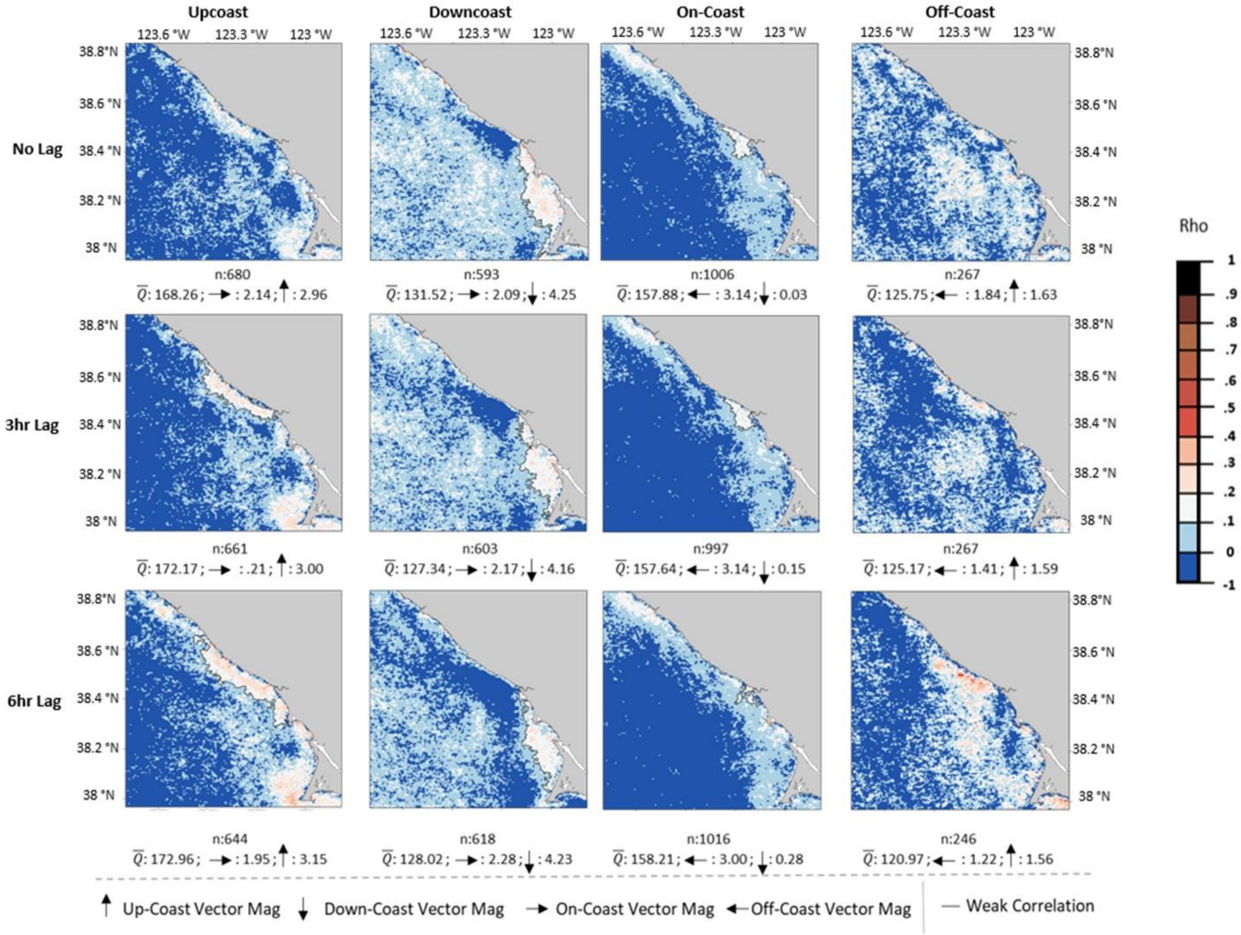

Fig. 9. Pixelwise correlation coefficients between Rrs_{645} and coincident daily average wind speed calculated separately for different wind quadrants (columns) and time lags (rows). The number of images in each subset (n) is listed beneath each image, along with information on average discharge (Q, m^3/s) and average windspeed (m/s) in alongshore and cross-shore orientations. Columns, left to right: daily average upcoast winds, downcoast winds, onshore winds, and offshore winds; Rows, top to down: no lag, 3 hours lag, 6 hours lag.

3.5 Tidal Effects

To explore tidal effects on the turbid plume of the Russian River, we calculate correlations between tidally varying water level (WL) and the turbidity index Rrs_{645} for each pixel (Fig. 10), as before, only using data when $p < 41$. Positive correlations indicate increased turbidity at higher tides and negative correlations indicate increased turbidity at lower tides. Correlations are weak, but small-scale zones are evident adjacent to the Russian River mouth.

Coherent zones of tide-correlated turbidity are most apparent for moderate discharge. For both the second and third discharge quartiles, there is a tendency for higher turbidity at high tide along the shore north of the mouth. However, to the south of the mouth, there is a tendency for higher turbidity at low tide (or lower turbidity at high tide), most apparent in high-discharge quartile plots. Also, for the second quartile, there is a small, elongated zone immediately off the mouth, corresponding to high turbidity at low tide.

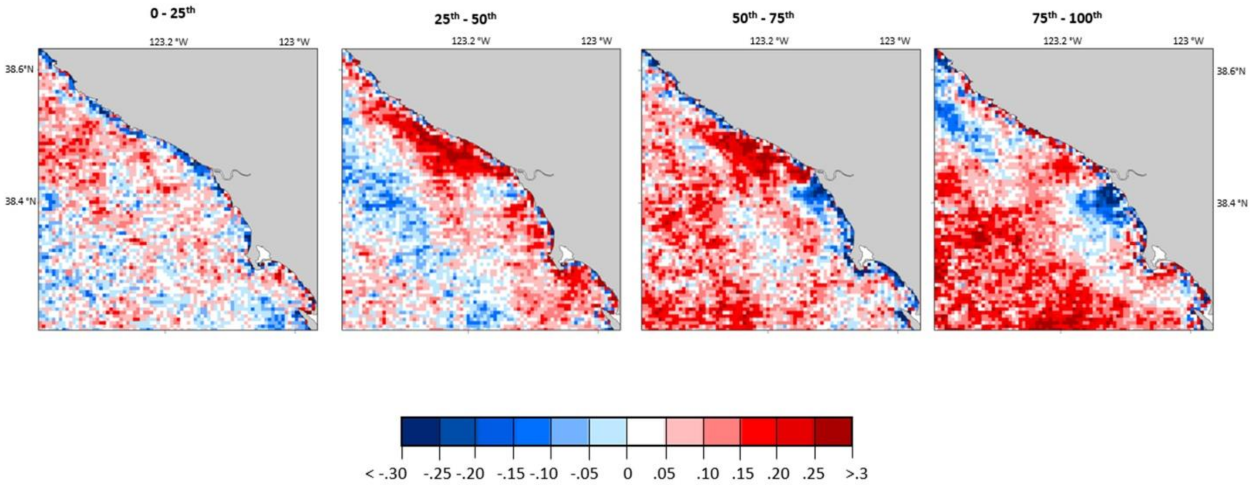

Fig. 10. Pixelwise correlation coefficients between Rrs_{645} and coincident water level (WL), calculated separately for four discharge quartiles. Maps are organized by increasing discharge (Q) quartiles from left to right: 0-25th percentile (16 to 42m^3/s); 25th-50th percentile (42 to 84m^3/s); 50th-75th (84 to 203m^3/s); 75th - 100th percentile (203 to 2366m^3/s)

4. Discussion

Runoff of freshwater from the land forms distinct low-salinity, turbid plumes in the coastal ocean, with shape and extent varying in response to river flow rate and ocean conditions. Prior work has identified at least four types of river plume, including classical large plumes controlled by a balance between buoyancy and Coriolis (Garvine, 1987; Horner-Devine, 2014), wind deflected plumes (Hickey et al., 2005; Lentz and Largier, 2002; Basdurak and Largier, 2022), tidally advected plumes (Basdurak et al., 2020), and plumes entrained into the surf zone by wave action (Kim et al., 2004; Clarke et al., 2007; Rodriguez et al., 2018; Kastner et al., 2019). Here we address a river where all these plume paradigms are observed, with different plume behavior occurring at different times. Outflow from the Russian River creates a turbid plume that is visible in satellite imagery (Fig. 1), both during high discharge and low discharge. Analysis of how turbidity at specific coastal ocean locations varies with changes in discharge, wind, waves, and tides reveals coherent patterns that reflect the influence of all four factors. While satellite data only enables us to track turbidity (concentration of fine suspended sediment), it is used here as a tracer for salinity patterns and patterns in the concentration of runoff-borne material .

Satellite data are only from the surface of the plume, lacking information on stratification and sub-surface structure. However, our results corroborate models and experiments, which help us explain the observed plume surface patterns. This study is novel in the degree of replication (~1500 whole-plume observations over 15 years), which allows us to consider multiple interacting drivers rather than reducing our analysis to a single dynamic. This immense data set shows the complexity and variability in plume types (different dominant forcing) – and variability even within plume types due to secondary forcing terms. Results show coherent patterns that vary with changes in river discharge, wind speed and direction, tidal phase, and wave height.

4.1 River Discharge

The strongest control on plume size and shape is exerted by the river outflow rate (discharge Q), shown by pixelwise correlation with turbidity (Figs. 5-8). Not only does high discharge result in a large volume of water, but it also represents a high buoyancy flux that explains spreading of the plume beyond the near field (where inertia dominates). The larger spatial scales (offshore extent, plume area) result in stronger Coriolis forcing and the observed tendency for high-discharge plumes to turn to the right, i.e., upcoast (Fig. 6). Thus, the Russian River plume behaves like other “large” river plumes in the classical dichotomy articulated by Garvine (1995) and others (Horner-Devine et al., 2015). However, while the Coriolis-induced turning region is observed, discharge off the Russian River and other SMRS is highly variable and high-discharge conditions last for only a few days so that one does not expect a coastal buoyancy current to form as observed for systems with more persistent outflow, e.g., Chesapeake Bay (Rennie et al., 1999), Mississippi River (Castillo and Miller, 2008). In contrast to the coasts characterized by singular, large outflows, the northern California coast is characterized by multiple SMRS that experience simultaneous high discharge events. When plumes coalesce (Warrick and Farnsworth 2017) a coastal buoyancy current may form, as observed off Oregon by Mazzini et al., (2014). For weaker discharges, Coriolis is not a primary forcing term, and the “small” plume configuration is shaped primarily by wind and tide as seen in models (Basdurak et al.,2020; Basdurak & Largier, 2022).

4.2 Wind Speed and Direction

The coastal ocean off northern California is subject to northerly upwelling-favorable winds for much of the year (Garcia-Reyes and Largier, 2012), but winds are more variable in winter when runoff events occur. The plume pattern is markedly different between days with upcoast (downwelling favorable) and downcoast (upwelling favorable) winds (Figs. 8 and 9). In all wind states the correlation between turbidity and discharge remains moderately strong near the mouth of the river (Fig. 8), but extends only upcoast during southerly/upcoast winds, and downcoast during northerly/downcoast winds. This indicates that wind forcing overcomes the buoyancy-Coriolis balance that makes the plume turn right and extend upcoast in the absence of wind (Fig. 7). This response of the plume to wind is also seen in the pixelwise correlation between turbidity and wind speed, calculated for different wind states (Fig. 9). While turbidity-wind correlations are notably weaker than turbidity-discharge correlations, during upcoast winds there is a coherent zone north of the mouth where higher turbidities are observed during stronger winds (most apparent with lag between turbidity and wind), i.e., it is not just the wind direction but also the strength of the wind that influences plume behavior. Likewise, a coherent zone is observed south of the mouth during downcoast winds.

One would expect turbidity-wind correlations to be weaker than turbidity-discharge correlations as wind does not alter the amount of runoff or turbidity and only influences the flow patterns in the receiving coastal waters. As discussed by Basdurak and Largier (2022), wind has multiple effects on river plumes including the direct effect of wind stress and the effect of wind-driven currents. Alongshore currents in this region are well correlated with alongshore wind forcing (Winant et al., 1987; Largier et al., 1993) and these currents can push and drag plume waters by upstream frontal convergence and underlying interfacial stress, respectively. The increase in correlation with lag is consistent with the lag in correlations between alongshore current and wind. At the same time, surface wind stress can force the plume directly, and most effectively when plume stratification is strong enough to contain added momentum in the shallow surface plume layer. Basdurak and Largier (2022) show that surface stress may move the whole plume, when mixing extends throughout the plume layer, or it may strain the plume and thus thin it and spread it downwind, when mixing decreases with depth (suppressed by stratification in the plume). These surface data provide no direct insight to sub-surface structure, but it is notable in Fig. 9 that the zone of coherent turbidity-wind correlation is confined nearshore with downwelling winds (onshore Ekman transport) and spread offshore with upwelling winds (offshore Ekman transport).

We find that cross-shore winds are also important, consistent with model results from Basdurak and Largier (2022). Indeed, turbidity-discharge correlations are strongest close to the river mouth during onshore winds (Fig. 8), indicating that high-turbidity waters are retained near the mouth during onshore winds, countering the offshore forcing due to outflow inertia and buoyancy-driven spreading. As onshore winds are not expected to drive strong onshore currents, this effect is likely due to direct wind forcing, i.e., surface wind stress. While there is a coastwide narrowing in the band of turbidity-discharge correlations with onshore winds, the zone of moderate/strong correlation extends only ~10 km alongshore (both upcoast and downcoast), indicating that onshore winds tend to prevent upcoast propagation of the plume. A similar near-mouth zone is observed for turbidity-wind correlation, showing that turbidities are higher with stronger onshore winds (although not nearshore downcoast of the mouth). It is interesting to note that the turbidity response to onshore wind does not exhibit a lag, which is consistent with direct forcing by wind stress and shorter time scales that do not involve Coriolis forcing. This plume compression by onshore winds has received little prior attention and only in models (Osadchiev et al., 2013; Basdurak and Largier, 2022) – we are unaware of any prior observations showing this effect.

4.3 Waves

As shown by Rodriguez et al., (2018) and Kastner et al., (2019), waves can stall the outflow jet and trap runoff and thus turbidity in surf zone and rip-current influenced nearshore waters. Here, we show that wave forcing can also be important for larger rivers, such as the Russian River – either during low discharge or during periods of large waves and high radiation stress. Through analysis of turbidity-discharge correlations, we quantify a threshold for the wave-outflow parameter *p* formulated by Rodriguez et al., (2018): for *p* values in the upper six deciles, we do not see plume-level Rrs_{645} turbidity at pixels located 1 km offshore of the mouth of the Russian River, so we choose $p = 41$ as the threshold for plumes escaping wave-dominated nearshore waters. This is comparable with a *p*-value of 20 obtained by Rodriguez et al., (2018) from numerical simulations representing conditions at the mouth of Tijuana River ($H_s = 1m$; $Q = 10m/s^3$). During strong wave forcing, turbid outflow can be trapped nearshore for river discharge as high as ~40 m^3/s, showing that wave forcing is likely to be important for all SMRS on wave-exposed coasts. This study is the first empirical validation of this wave-outflow momentum balance for a SMRS.

While river waters may be exported from the surf zone through rip currents after being initially trapped (Clarke et al., 2007), the inertia of the outflow has been lost and even the buoyancy head has been dissipated by mixing in the nearshore. Consequently, these turbid, low-salinity waters are more likely to be dispersed passively and without stratification. And without immediate mechanisms to transport these waters offshore, they are likely to remain in contact with the shore far from the mouth of the river (e.g., Kim et al.,2004).

4.4 Tides

Through an analysis of turbidity-water level correlations (Fig. 10), we show tidal variability in plume behavior addition to strong control by discharge and additional significant control by wind forcing. Basdurak et al., (2020) model the influence of tide on outflow from an idealized SMRS in California and show the alongshore advection of the plume by reversing tidal currents (best described by comparison to the wagging tail of a dog). As noted by Basdurak and Largier (2022), these tidal influences are readily dominated by wind forcing, but in all but the strongest winds the plume continues to exhibit some tidal variability. Consistent with Basdurak et al., (2020) we observed increasing turbidity north of the river mouth during rising tides (Fig. 10), explained by the northward advection of turbid outflow by alongshore tidal currents. The effect is not observed for weak discharge when turbidity is low and the plume can easily be deflected by winds. The effect is strongest for moderately high discharge (up to ~200 m^3/s), when turbidity is higher and there is a tendency for upcoast transport, which can be enhanced by upcoast tidal currents. For highest discharges, correlations are low as the plume is persistent along this coast, without turbidity gradients that can be advected by tidal currents.

South of the river mouth (downcoast), turbidity increases over the falling tide (Fig. 10), consistent with southward advection of turbid waters by the alongshore tidal current. Even if the tidal component is smaller than wind-driven component, it introduces tidal variability in the current which will explain tidal variability in turbidity at a point, given the alongshore gradient in turbidity. Again, the effect is not observed for weakest discharges, but here it is strongest for the upper two discharge quartiles and higher correlations are observed than upcoast of the mouth.

In addition to this alongshore tidal advection, tides modulate the outflow from the Russian River estuary (Behrens et al., 2013). This effect may explain the offshore elongated shape of the negative correlation observed for the second discharge quartile (Fig. 10), which is included in the negative correlation zone for third and fourth quartiles. Tidal fluctuations in outflow are more marked for weak/moderate river discharge when river flow can be retained in the estuary during rising tides and maximum outflow of turbid waters occurs during falling tides, explaining offshore advection and tidally increased turbidity in this zone. Downcoast of the mouth the tidal efflux effect and the alongshore tidal advection effect both account for a negative correlation, whereas the effects have opposite sign upcoast of the mouth, which may explain the marked negative zone immediately south of the mouth of the river. This may also explain the absence of a positive signal about the inlet in the lowest discharge quartile in Fig. 10, as a rising tide could reduce outflow from small discharges.

4.5 Other Nearby Sources of Turbidity

There are multiple sources of turbidity in the coastal waters off northern California, including land runoff, bay outflow, wave-driven resuspension, and tidal resuspension. Tidal resuspension is not apparent in open waters outside of tidal bays like San Francisco Bay, but wave-driven resuspension of fine sediment is evident in nearshore waters along the coast of northern California, which is the focus of a companion study (Speiser et al, in prep.) – this is evident as high mean turbidity along the wave-exposed north shores of Bodega Head and Point Reyes (Fig. 4). Here our interest is in the effect of river plumes, which we explore through the Russian River case study. Patterns of turbidity-discharge correlation show a clear maximum close to the river mouth, weakening with distance away from the mouth due to decreasing turbidity and the importance of other processes and sources. Some alternative turbidity sources are evident in our study because discharge from nearby rivers (e.g., Gualala River) is correlated with that in the Russian River, thus accounting for the high turbidity-correlation values off the mouth of the Gualala River (38.77° N, Figs. 5, 7 and 8). The Gualala plume is visible on 28 February 2019 (Fig. 1b) and in a map of mean turbidity (Fig. 4).

High levels of turbidity in Bodega Bay and Tomales Bay, evident in the image from 28 February 2019 (Fig. 1C), are also associated with land runoff through smaller rivers including Estero Americano and Estero San Antonio that enter Bodega Bay and Walker Creek and Lagunitas Creek that enter Tomales Bay. Again, high discharge events occur simultaneously in these small rivers and the Russian River following rain events, thus accounting for high turbidity-discharge correlations in Bodega Bay (Fig. 5, 6, 7), which can merge with high correlations associated with the Russian River (Fig. 8) – and potentially misinterpreted as being due to the Russian River.

A third regional source of turbidity is outflow from San Francisco Bay, entering the ocean through its mouth south of Point Reyes (37.8°N). Although turbidity is lower than in river plumes (Fig. 1C), there is a coherent pattern of turbidity associated with northward transport past Point Reyes (Kaplan and Largier, 2006; Largier, 2020) that is evident during high-discharge events when the Bay outflow turns right under the influence of Coriolis forcing (Fig. 6) and that accounts for notably high turbidity-discharge correlations during southerly winds (Fig. 8) and markedly higher turbidities during stronger southerly winds (Fig. 9). These low-salinity events are recorded at Bodega Head (Ricart et al., 2024).

4.6 Implications of Plume Patterns

Satellite data on surface reflectance allows analysis of surface turbidity patterns that we have quantified and subsequently explained in terms of plume behavior. The analysis of turbidity is immediately valuable in providing insight to sub-surface light levels important for photosynthesis and insight to the fate of fine terrigenous sediment and sorbed materials that can include organics, metals, and pollutants. Further, the spatial extent (> 30 km) and temporal persistence (> 1 day) of the observed turbidity patterns indicate slow settling velocities so that the decrease in concentration away from the mouth of the river is likely controlled by mixing and dilution. In that case these patterns of turbidity are also a reasonable first estimate of patterns of dissolved material including salinity, nutrients, and carbon. The zone of impact (area where river-borne material is concentrated) varies with changes in discharge, winds, waves, and tides – but clear correlations emerge that can explain patterns of exposure to diverse river-borne constituents. There is growing interest in the exposure of shoreline environments (e.g., recreational beaches) and nearshore environments (e.g., kelp forests) to runoff, which may transport pathogens, e.g., toxoplasma gondii (Shapiro et al., 2015) and fecal coliform (Kim et al., 2004) and other pollutants (Rogowski et al., 2015). There is also growing interest in the role of river plumes in explaining kelp refugia amidst a catastrophic loss of kelp forests off northern California (Rogers-Bennett et al, 2019; Cavanaugh et al., 2023; Ricart et al, in review), in their potential role in ameliorating or exacerbating nearshore ocean acidification due to their high carbon content (Stets et al., 2017), and in their potential for explaining localized stratification and hypoxia. Shoreline attachment is shown to be strongest on the upcoast side of the Russian River mouth and this is generally expected. Stronger upwelling winds are anticipated with climate change (Garcia-Reyes et al., 2022) and that would reduce this effect, but at the same time more intense flow events are anticipated with more frequent atmospheric river events (Albano et al., 2020) and that would intensify the shoreline impacts upcoast of the mouth.

5. Conclusion

The long record of daily MODIS Aqua imagery of coastal waters off the Russian River offers a comprehensive overview of plume behavior, specifically identifying features characteristic of plumes formed off the mouth of Mediterranean-climate, small-mountainous-river-systems (SMRS). This expansive dataset, contextualized by coincident environmental monitoring data, corroborates several plume models and offers new insights into the interaction between buoyancy-Coriolis forcing with wind forcing, wave forcing, and tidal forcing.

Results from our study highlight the significant control of river outflow rate on plume size and shape and the contrast between small and large plumes. High discharge rates result in “large” plumes with significant Coriolis influence beyond the near field whereas low discharge rates result in “small” plumes subject to forcing by winds and tides. The spatial extent of the plume varies significantly, with the average alongshore extent of turbid plumes increasing from 14 km for the lowest discharge quintile to 77 km in the highest quintile. Similarly, the offshore extent increases from 3 km to 14 km across the same quintiles, and plume area increases from 20 km^2 to 698 km^2. In the highest quintile, outflow from the Russian River plumes coalesces with other regional outflows, obscuring the degree of individual contribution to coastal turbidity that extends throughout the study site.

Maps of the correlation of turbidity with observed environmental indices clarify the roles of wave, tide, and wind forcing. Wave forcing, quantified through the wave-outflow momentum balance parameter p, shows that plume-level turbidity is not observed more than 1 km offshore when $p > 41$, as wave radiation stress dominates river outflow momentum. For plumes with enough discharge momentum to overcome wave forcing, near-field dispersion is modulated by tidal forces, causing upcoast and downcoast deflection during rising and falling tides, respectively. The far-field plume is strongly controlled by wind direction, with discharge-correlated turbidity extending more than 30 km upcoast (and minimal downcoast signal) during southerly winds. During northerly winds, discharge-correlated turbidity extends 30 km downcoast with no upcoast signal. This demonstrates the dominance of wind over Coriolis forcing, except during weak winds or very high discharge. Onshore winds compress river sediment turbidity towards the shore.

Our analysis was limited to observing single-feature correlations and used multi-feature data subsetting to examine combined effects, rather than employing computationally expensive multivariate statistics. These limitations highlight the need for further studies using advancing computational techniques and higher-resolution datasets. Advanced techniques, particularly in machine learning and computer vision processing of high-resolution imagery, will help capture the fine, dynamic details needed to understand the controls on smaller outflows from SMRS. We are motivated by ever-growing high-resolution imagery datasets and developing capabilities in machine learning to continue research in these essential nearshore freshwater outflow processes. Nevertheless, these observations are invaluable in revealing the complexity of space-time patterns in land runoff and in ground-truthing recent numerical models. Our analysis of an immense number of plume visualizations under diverse discharge, wind, wave, and tide conditions provides novel insights that can guide future model and field experiments.

Author contribution

William Speiser designed and applied the remote sensing and data analysis methodology and wrote the first draft of the manuscript. John Largier assisted in project conceptualization, provided key insights into oceanographic and hydrologic processes, and revised the manuscript.

Acknowledgments

We are grateful for funding from the State of California (CA Ocean Protection Council grant) and the National Science Foundation (DISES Grant #2108002).

References

Albano, C. M., Dettinger, M. D., & Harpold, A. A. (2020). Patterns and drivers of atmospheric river precipitation and hydrologic impacts across the western United States. *Journal of Hydrometeorology*, *21*(1), 143-159.

Armi, L., and Farmer, D. M. (1986). Maximal two-layer exchange through a contraction with barotropic net flow. *Journal of Fluid Mechanics*, *164*, 27-51.

Aurin, D., Mannino, A., and Franz, B. (2013). Spatially resolving ocean color and sediment dispersion in river plumes, coastal systems, and continental shelf waters. *Remote Sensing of Environment*, *137*, 212-225.

Basdurak, N. B., Largier, J. L., and Nidzieko, N. J. (2020). Modeling the dynamics of small-scale river and creek plumes in tidal waters. *Journal of Geophysical Research: Oceans*, *125*(7), e2019JC015737.

Basdurak, N. B., and Largier, J. L. (2022). Wind effects on small-scale river and creek plumes. *Journal of Geophysical Research: Oceans*, *128*, e2021JC018381

Behrens, D. K., Bombardelli, F. A., Largier, J. L., and Twohy, E. (2013). Episodic closure of the tidal inlet at the mouth of the Russian River—A small bar-built estuary in California. *Geomorphology*, *189*, 66-80.

Del Castillo, C. E., and Miller, R. L. (2008). On the use of ocean color remote sensing to measure the transport of dissolved organic carbon by the Mississippi River Plume. *Remote Sensing of Environment*, *112*(3), 836-844.

Fernández-Nóvoa, D., Mendes, R. D., Decastro, M., Dias, J. M., Sánchez-Arcilla, A., and Gómez-Gesteira, M. (2015). Analysis of the influence of river discharge and wind on the Ebro turbid plume using MODIS-Aqua and MODIS-Terra data. *Journal of Marine Systems*, *142*, 40-46.

Fong, D. A., and Geyer, W. R. (2001). Response of a river plume during an upwelling favorable wind event. *Journal of Geophysical Research: Oceans*, *106*(C1), 1067-1084.

Fong, D. A., and Geyer, W. R. (2002). The alongshore transport of freshwater in a surface-trapped river plume. *Journal of Physical Oceanography*, *32*(3), 957-972.

Garvine, R. W. (1995). A dynamical system for classifying buoyant coastal discharges. *Continental Shelf Research*, *15*(13), 1585-1596. Gerbi, G. P., Chant, R. J., and Wilkin, J. L. (2013). Breaking surface wave effects on river plume dynamics during upwelling-favorable winds. *Journal of physical oceanography*, *43*(9), 1959-1980.

Geyer, W. R., Hill, P., Milligan, T., and Traykovski, P. (2000). The structure of the Eel River plume during floods. *Continental Shelf Research*, *20*(16), 2067-2093.

Griggs, G. B., and Hein, J. R. (1980). Sources, dispersal, and clay mineral composition of fine-grained sediment off central and northern California. *The Journal of Geology*, *88*(5), 541-566.

Hetland, R. D. (2010). The effects of mixing and spreading on density in near-field river plumes. *Dynamics of Atmospheres and Oceans*, *49*(1), 37-53.

Hickey, B. M. S. L., Geier, S., Kachel, N., and MacFadyen, A. (2005). A bi-directional river plume: The Columbia in summer. *Continental Shelf Research*, *25*(14), 1631-1656.

Horner-Devine, A. R., Jay, D. A., Orton, P. M., and Spahn, E. Y. (2009). A conceptual model of the strongly tidal Columbia River plume. *Journal of Marine Systems*, *78*(3), 460-475.

Horner-Devine, A. R., Hetland, R. D., and MacDonald, D. G. (2015). Mixing and transport in coastal river plumes. *Annual Review of Fluid Mechanics*, *47*, 569-594.

Kastner, S. E., Horner-Devine, A. R., and Thomson, J. M. (2019). A conceptual model of a river plume in the surf zone. *Journal of Geophysical Research: Oceans*, *124*(11), 8060-8078.

Kaplan, D. M., and Largier, J. (2006). HF radar-derived origin and destination of surface waters off Bodega Bay, California. *Deep Sea Research Part II: Topical Studies in Oceanography*, *53*(25-26), 2906-2930.

Kim, J. H., Grant, S. B., McGee, C. D., Sanders, B. F. and Largier, J. L. (2004). Locating Sources of Surf Zone Pollution: A Mass Budget Analysis of Fecal Indicator Bacteria at Huntington Beach, California *Environmental Science & Technology*, 38, 2626-2636, 10.1021/es034831r.

Largier, J. L., Magnell, B. A., and Winant, C. D. (1993). Subtidal circulation over the northern California shelf. *Journal of Geophysical Research: Oceans*, *98*(C10), 18147-18179.

Largier, J. L. (2020). Wind-Modulated Buoyancy Current Pulses Associated with Outflow from San Francisco Bay. In *Ocean Sciences Meeting 2020*. AGU.

Largier, J., Behrens, D., Hewett, K., Koohafkan, M., Robart, M., Dann, D. and Roettger R. (2020). Managing the mouth of the Russian River Estuary, California. In: *Complex Coastal Systems –*

Transdisciplinary Learning on International Case Studies. J. Slinger, S. Taljaard, F. d'Hont (eds), Delft Academic Press, pp 71-86.

Lentz, S. J., and Largier, J. (2006). The influence of wind forcing on the Chesapeake Bay buoyant coastal current. *Journal of Physical Oceanography*, *36*(7), 1305-1316.

Mazzini, P. L., Barth, J. A., Shearman, R. K., and Erofeev, A. (2014). Buoyancy-driven coastal currents off Oregon during fall and winter. *Journal of Physical Oceanography*, *44*(11), 2854-2876.

Mendes, R., Vaz, N., Fernández-Nóvoa, D., Da Silva, J. C. B., Decastro, M., Gómez-Gesteira, M., and Dias, J. M. (2014). Observation of a turbid plume using MODIS imagery: The case of Douro estuary (Portugal). *Remote sensing of environment*, *154*, 127-138.

Miche, M. (1944). Mouvements ondulatoires de la mer en profondeur constante ou décroissante. *Annales de Ponts et Chaussées, 1944, pp (1) 26-78,(2) 270-292,(3) 369-406*.

O'Reilly, W. C., Olfe, C. B., Thomas, J., Seymour, R. J., and Guza, R. T. (2016). The California coastal wave monitoring and prediction system. *Coastal Engineering*, *116*, 118-132.

Pullen, J., and Allen, J. S. (2001). Modeling studies of the coastal circulation off northern California: statistics and patterns of wintertime flow. *Journal of Geophysical Research: Oceans*, *106*(C11), 26959-26984.

Rennie, Sarah E., John L. Largier, and Steven J. Lentz. "Observations of a pulsed buoyancy current downstream of Chesapeake Bay." *Journal of Geophysical Research: Oceans* 104, no. C8 (1999): 18227-18240.

Ricart, A. M., Gómez, G. B., Karm, R. H., Largier, J. L., Souza, V., Dias, A. S., Velázquez, M. G., Nelson, T., Cavanaugh, K. C., Cavanaugh, K. C. and Hughes, B. B. (2024). Persistent kelp forests during a massive decline reveal the importance of land-sea connectivity. Ecology (submitted).

Rodriguez, A. R., Giddings, S. N., and Kumar, N. (2018). Impacts of nearshore wave-current interaction on transport and mixing of small-scale buoyant plumes. *Geophysical Research Letters*, *45*(16), 8379-8389.

Rogers-Bennett, L., and Catton, C. A. (2019). Marine heat wave and multiple stressors tip bull kelp forest to sea urchin barrens. *Scientific reports*, *9*(1), 15050. Q

Rogowski, P. A., Terrill, E., Schiff, K., and Kim, S. Y. (2015). An assessment of the transport of southern California stormwater ocean discharges. *Marine Pollution Bulletin*, *90*(1-2), 135-142.

Runyan, K., and Griggs, G. B. (2003). The effects of armoring seacliffs on the natural sand supply to the beaches of California. *Journal of coastal research*, 336-347.

Saldías, G. S., Sobarzo, M., Largier, J., Moffat, C., and Letelier, R. (2012). Seasonal variability of turbid river plumes off central Chile based on high-resolution MODIS imagery. *Remote Sensing of Environment*, *123*, 220-233.

Saldías, G. S., Largier, J. L., Mendes, R., Pérez-Santos, I., Vargas, C. A., and Sobarzo, M. (2016). Satellite-measured interannual variability of turbid river plumes off central-southern Chile: Spatial patterns and the influence of climate variability. *Progress in Oceanography*, *146*, 212-222.

Stets, E. G., Butman, D., McDonald, C. P., Stackpoole, S. M., DeGrandpre, M. D., and Striegl, R. G. (2017). Carbonate buffering and metabolic controls on carbon dioxide in rivers. *Global Biogeochemical Cycles*, *31*(4), 663-677.

Thomson, J., Horner-Devine, A. R., Zippel, S., Rusch, C., and Geyer, W. (2014). Wave breaking turbulence at the offshore front of the Columbia River plume. *Geophysical Research Letters*, *41*(24), 8987-8993.

Wang, M., Son, S., and Shi, W. (2009). Evaluation of MODIS SWIR and NIR-SWIR atmospheric correction algorithms using SeaBASS data. *Remote Sensing of Environment*, *113*(3), 635-644.

Warrick, J. A., DiGiacomo, P. M., Weisberg, S. B., Nezlin, N. P., Mengel, M., Jones, B. H., ... and Farnsworth, K. L. (2007). River plume patterns and dynamics within the Southern California Bight. *Continental Shelf Research*, *27*(19), 2427-2448.

Warrick, J. A. (2020). Littoral sediment from rivers: Patterns, rates and processes of river mouth morphodynamics. *Frontiers in Earth Science*, *8*, 355.

Warrick, J. A., and Farnsworth, K. L. (2017). Coastal river plumes: Collisions and coalescence. *Progress in oceanography*, *151*, 245-260.

Wheatcroft, R. A., Goñ i, M. A., Hatten, J. A., Pasternack, G. B., and Warrick, J. A. (2010). The role of effective discharge in the ocean delivery of particulate organic carbon by small, mountainous river systems. *Limnology and Oceanography*, *55*(1), 161-171.

Winter, S. A. (2020). A Investigation of the Closure Regimes of California's Bar-Built Estuaries. MS Thesis, UC Davis, 92 pages.

Wong, S. H., Monismith, S. G., and Boehm, A. B. (2013). Simple estimate of entrainment rate of pollutants from a coastal discharge into the surf zone. *Environmental science and technology*, *47*(20), 11554-11561.

CHAPTER 2

Remote Sensing of Nearshore Sea Surface Temperature Using Landsat Brightness Temperature Calibrated by MODIS Data

Abstract

Understanding and monitoring nearshore environments is essential, given that these fine-scaled ecosystems are integral to human well-being. While satellites offer an opportunity to gain synchronous and spatially extensive data of these understudied areas, calibrated satellite sea surface temperature (SST) measurements, which are essential for monitoring water quality, have only been available at coarse resolutions of 1 km or larger. In this study, we develop a novel methodology to create a simple linear equation to calibrate fine-scale Landsat thermal infrared radiation brightness temperatures, initially calibrated for land-sensing, to derive SST at a resolution of 100m. The constants of this equation are derived from correlations of coincident MODIS SST and Landsat data, which we filter to find optimal pairs. Our methodology allows us to filter calibrated Landsat data to find the most accurate, optimal data. Validation against in-situ measurements from buoys at varying distances from the shore in Northern California shows that our calibrated SST data greatly enhances accuracy compared to the original Landsat temperature data and demonstrates superior accuracy compared to coincident MODIS SST data. Root mean square error from the ordinary least squares equation within these validations for our minimally filtered dataset (n=557 images) ranges from 0.76 to 1.20 °C with correlation coefficients r=0.73 to 0.92, and from our optimal dataset (n=229 images) between 0.62 to 0.98 °C with correlations from r=0.83 to 0.92. Potential error sources, such as seasonality, are examined. We discuss the utility of our methodology for enhancing coastal monitoring efforts and capturing previously unseen spatial complexity. Testing the calibration methodology on Landsat images before and after the temporal bounds of accurate MODIS SST measurements shows successful calibration with lower errors than the off-the-shelf,

land-calibrated Landsat product, extending the applicability of our approach. This data calibration methodology is beneficial for calibrating cross-mission Landsat satellite data to derive SST within the nearshore region of our study site and has potential applicability to similar Mediterranean climate regions globally, contributing to improved coastal monitoring, management, and research.

1. Introduction

The ocean is vast and most human interactions are in nearshore waters, which also host the most productive ecosystems (Pauly & Christensen, 1995). There are relatively few data from the waters within a few kilometers of the land, which is a major oversight given the importance of these waters for ecosystems and humans (Muller-Karger et al., 2018), and it is often assumed that waters are quite uniform and like those further offshore over the continental shelf. While satellites offer an opportunity to gain synchronous and spatially extensive data of these understudied areas, there are no publicly available platforms that provide reliable surface properties at a spatial scale sufficient to resolve primary nearshore flow features and dynamics. Specifically, sea surface temperature (SST) is only available at a scale of 1 km or larger and these data are notorious for poor reliability within a pixel of the shoreline due to contamination (Feng and Hu, 2017). Through calibration of high-resolution Landsat brightness temperature data with concurrent low-resolution MODIS SST data, we develop a new method and data set that can effectively resolve the fine scale of SST in nearshore waters with high fidelity.

Nearshore water circulation differs markedly from offshore regions due to the proximity and shape of the shoreline and shoals. Phenomena include rip currents (MacMahan et al., 2006; Largier, 2022), large and small river outflow plumes (Basdurak et al., 2020; Horner-Devine et al., 2015; Speiser and Largier, in review), tidal jets (Chadwick and Largier, 1996; Wolanski and Elliott, 2015), internal wave shoaling (Lamb, 2014), the coastal boundary layer (Nickols et al., 2012), and small-scale wind effects (Lentz and Fewings, 2012). These flow features account for complex patterns in water properties, including temperature and salinity as well as biogeochemical (oxygen, pH, pCO_2, $N0_3$) and biological (phytoplankton, meroplankton, and pathogenic microbes) parameters. At times, these patterns are made visible by a concurrent turbidity or water-color signal, which can be detected by high-resolution optical satellite imagery (Speiser and Largier, in review). However, few reliable methods exist for obtaining satellite-based data on sea-surface temperature at sufficient spatial resolution, despite the ubiquity of thermal patterns in nearshore waters. While there is an increasing number of studies based on numerical experiments and in-situ field sensors (Gough et al., 2020), their scope is generally limited by scale and the full complexity of multi-scale nearshore circulation processes remains opaque (Largier, 2020).

The Landsat series of satellites operated by the United States Geological Survey (USGS) contain onboard thermal infrared radiation (TIR) sensors with a spatial resolution (60-120m) fine enough to resolve the primary nearshore circulation features with sub-kilometer scale. However, these satellites lack atmospheric self-correction capabilities owing to a limited number of TIR range bands, which precludes the conversion of TIR brightness values to sea surface temperature value without external, empirical calibration.

Prior studies have used several methods to extract SST information from Landsat TIR data. Some studies have used off-the-shelf, Landsat Level 2 brightness temperature data, calibrated by the USGS for land surfaces (Albanai et al., 2022). Other software packages like ACOLITE (Vanhellemont, 2020) derive surface temperatures from converting atmospherically corrected surface radiance using Planck's Law (see section 2.4) enhanced by radiative transfer models; however, these methods rely on accessing abundant coincidental data, which often complicates atmospheric correction. Other studies have been very local, calibrating brightness data with in-situ/buoy measurements (Wloczyk et al., 2006; Jang and Park, 2019). While prior studies have explored correlation of Landsat data with coincident satellite data from geostationary satellites (Kuroda and Toya, 2020) or polar orbiting satellites like MODIS and AHVRR (Thomas et al., 2002;

Fisher and Mustard, 2004; Snyder et al., 2017, Fu et al., 2020), these studies have been limited to less than 50 images, which is insufficient for capturing nearshore variability, and does not aggregate statistics to form generalized calibration constants which makes the methodology dependent on other satellite missions as well as their continuation for future calibrations. This becomes complicated as satellites eventually age past their expected mission lifetimes and subsequently experience issues with data degradation. Relevantly, MODIS is now past its expected mission lifetime and has been shown to have unreliable data quality for SST products past 2023 (Twedt et al., 2023). Further this methodology requires manual inspection and selection of data to avoid any sources of heterogeneity within images which is arduous and limits dataset size.

In this paper, we calibrate an extensive dataset of several hundred Landsat 7-9 images using coincidental MODIS SST (M_{SST}) data captured prior to 2023 for coastal waters off northern California. Our initial approach is to create a unique calibration equation for each image, and our final product is a single equation obtained from averaging the single-image calibrations, that can be applied to images outside of the sample set without having to do individual image calibrations. We test this sample calibrated Landsat SST data as well as Landsat SST data before and after MODIS operational dates against in-situ temperature measurements from 5 locations, showing the superior utility of the aggregate calibration equation for use in SST remote sensing, which also outperforms the use of off-the-shelf USGS land surface temperature measurements. The resultant high-resolution SST data will greatly advance the study of nearshore flow features, hydrodynamic processes, and habitat patterns.

2. Methods

This study investigates the efficacy of Landsat surface brightness temperatures calibrated with MODIS Terra Sea Surface Temperature data to produce high spatial resolution SST measurements. We test these calibrations performed between individual images and use aggregated calibration equations to create a generalized local calibration equation, made from constants derived from statistics gathered from those calibrations. These estimated SST data are validated using in-situ monitoring data taken throughout the study region, captured at the same time as satellite overpass.

2.1 Study Site

Data used for this study are captured within Landsat Worldwide Reference System (WRS) location path 45, row 33, spanning latitudinal coordinates from 37.90 to 39.95 (Fig. 1). This area extends from the inlet of the San Francisco Bay northward to Cape Mendocino, covering a geomorphologically and hydrodynamically diverse coastline that contributes to oceanic temperature mixing through phenomena such as runoff from ephemeral streams and small mountain river systems, tidal jets, and flow separation at headlands. The meteorology of this region is a typical "Mediterranean" climate, with seasonal precipitation occurring in winter months. Winter storms lead to seasonal freshwater runoff pulses and associated river plumes (e.g., off the Russian River, Gualala River, Big River, Noyo River, Albion River, and Navarro River (Fig. 1). During high river flow, freshwater buoyant plumes from these rivers extend tens of kilometers alongshore (Speiser and Largier, in review). In the dry season, these estuaries can be closed off from the ocean by sand berms (Behrens et al.,2013), cutting off surface exchange with the ocean.

Wind patterns in the region are also seasonal. From April to June, consistent northerly winds induce upwelling, followed by weaker winds from July to September, and more variable winds in the storm season from December to February (Garcia-Reyes and Largier, 2012). Spring upwelling causes nearshore cooling from offshore advection of warmer surface water. The most marked cooling from upwelling occurs in the region southward of Pt. Arena and northward of the Russian River estuary (Largier et al.,1993; Halle and Largier, 2011).

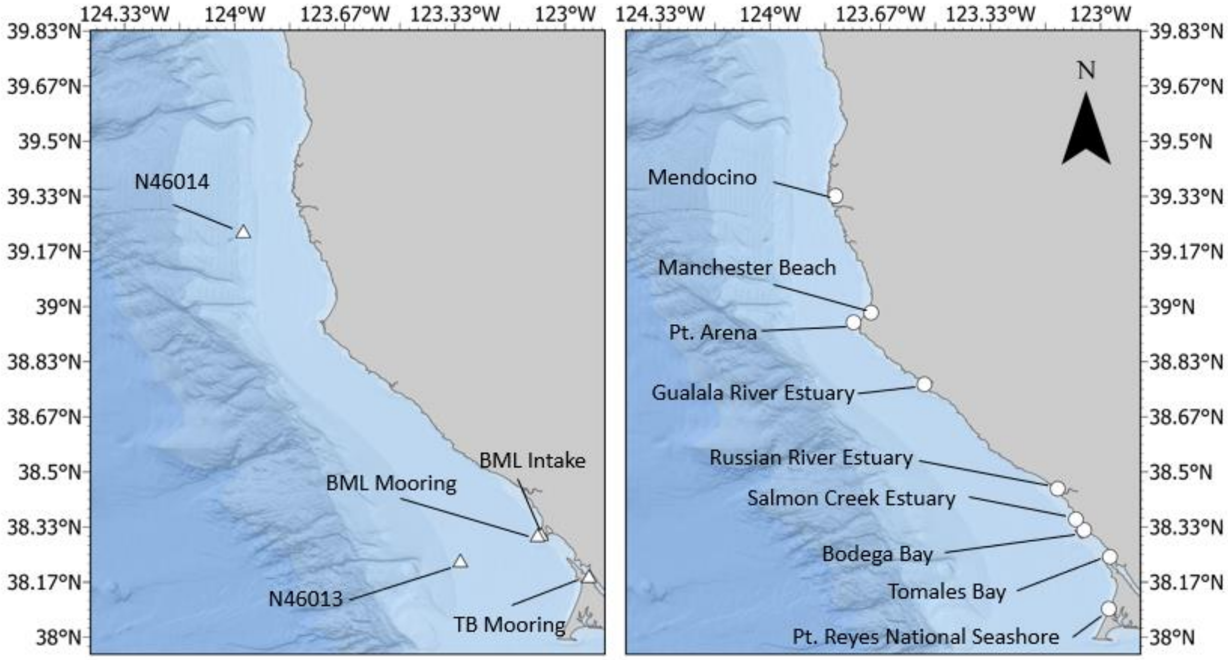

Fig. 1.: Map of study region in WRS path 45 row 33. (Left) Map of in-situ validation sites, from north to south: NOAA N46014 (buoy), BOON Intake (seawater intake), BML Mooring (buoy), NOAA N46013 (buoy), and BOON Tomales Bay (buoy). (Right) Map of geographical points of interest, from north to south: Mendocino, Manchester Beach, Pt. Arena, Gualala River Estuary, Russian River Estuary, Salmon Creek Beach, Bodega Bay, Tomales Bay, Pt. Reyes National Seashore.

2.2 Satellite Data

All Landsat 5-9 Level 2 (L2) (March 1984 to May 2023) thermal infrared radiation Landsat Brightness Temperature B_t data within the World Reference System (WRS) scene location at Path 45 Row 33 were collected from Google Earth Engine (Gorelick et al., 2017). For Landsat's L2 product, the USGS calibrates Landsat surface radiance to B_t, calibrated for land surface temperatures, by applying Planck's equation:

$$B_t = \frac{K_2}{ln\,(\frac{K_1}{L_S}+1)} \qquad \text{eq 1.}$$

where B_t= Brightness Temperature, K1 = (L7: 666.0900 ; L8: 774.8853; L9: 799.0284), K2=(L7:1282.7100; L8: 1321.0789; L9: 1329.2405), and Ls= surface radiance. These temperature data, in degrees Kelvin, are stored as values scaled by a factor of .00341802 and offset by a value of 149 to convert data to integers for more efficient storage. Clouds and cloud shadow detection within these images were performed using the CFMASK algorithm (Foga et al., 2017). This algorithm employs decision trees, validated by scene-wide statistics, to accurately label pixels affected by clouds and their shadows. These cloud-affected regions are further delineated based on cloud height and the solar angle, enhancing the precision of cloud and shadow detection. Land features were then masked from each image using the high-resolution NOAA Continually Updated Shoreline Product (NOAA CUSP: https://shoreline.noaa.gov/data/datasheets/cusp.html). This geospatial land dataset is derived from repositories of LiDAR data and individual shoreline datasets, estimates continental shorelines on a scale from 1:1000 to 1:24000.

Landsat 7 (L7), operational since 1999, features Band 6 (10.40-12.50 µm), which is specifically dedicated to collecting TIR readings with a resolution of 60m. However, L7 encountered a known issue with its Scan Line Corrector (SLC) in 2003, leading to data gaps in its imagery. Despite this, its high-resolution thermal data remains invaluable. L7 has a 16-day revisit cycle and typically overpasses a given location at 10:30 am, contributing to the temporal coverage of the study.

Both Landsat 8 (L8) and Landsat 9 (L9) are equipped with two TIR sensors of the same range, but temperature is typically derived with the Band 10 sensor (10.60-11.19 µm) due to its reduced sensitivity to stray light in contrast to the other TIR sensor from curvature of its lens (Montanaro et al., 2014; Snyder et al., 2017). L8, launched in 2013, and Landsat 9, launched in 2021 and follow a similar 16-day overpass cycle as L7, capturing data in the same mid-morning time window

To align the resolution disparities among the Landsat satellites, L7 images were resampled from their native 60m resolution to 100m using bilinear interpolation, matching the resolution of L8 and L9 images. Out of 705 images obtained across these missions, 659 images were used, the rest being omitted for having pixel count (n) <100 pixels or when coincident M_{SST} images had an n=0 pixel count. Statistics on pixel availability are displayed in Fig. 2, showing that on average the most available pixels are captured in April and September, while the least are captured in July and August, perhaps due to coastal fog that is prominent during summer months in the Northern California region (Johnstone and Dawson, 2010; Torregrosa et al.,2014).

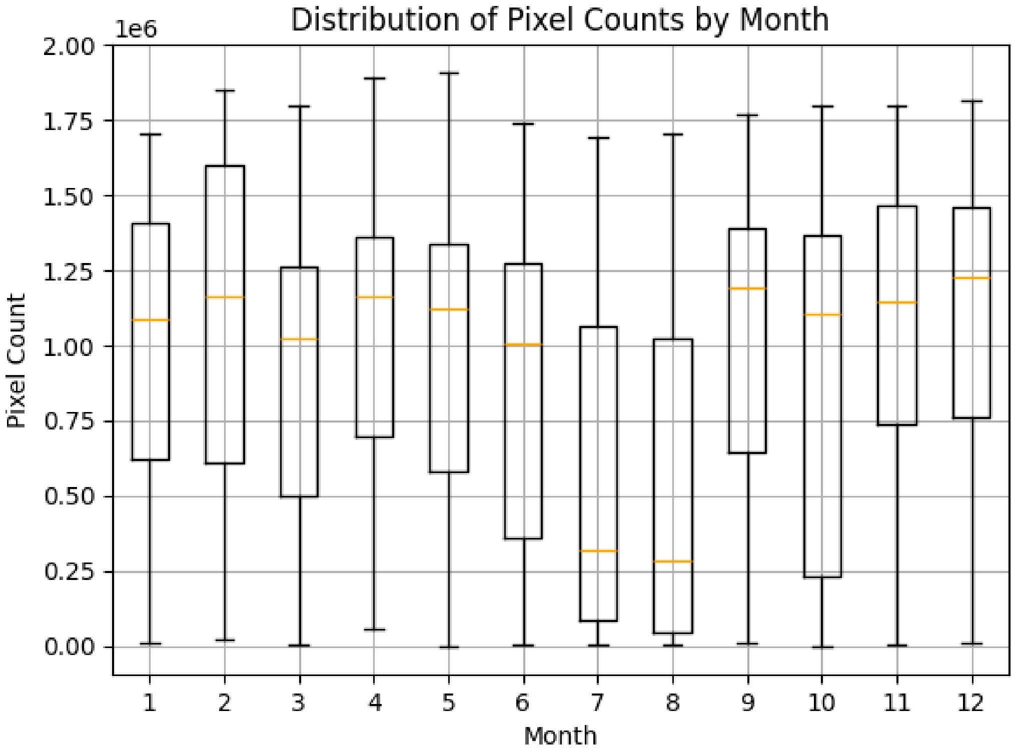

<u>Fig. 2</u>: (Top): Box and whisker plot pixel counts (y-axis) by month (x-axis) per-image in the dataset. Box margins are lower 25th percentile of data (lower) and 75th percentile of data (upper). Line in box is monthly median. Whiskers show minimum and maximum values.

Although Landsat 5 (operational from 1984 to 2013) captures TIR data in a similar spectral range and overpass window to L7 and has data during the timeframe available for this study, it has spatial resolution of 120m, which is coarser than the 100m that we resample images to for this study. Additionally, L5 experienced a gradual shift in its solar zenith angle over time due to changes in orbital altitude (Zhang et al., 2016). This led to its exclusion from initial data calibrations. Nonetheless, because of its spectral range, L5 data is used in this study as a blind dataset to test the generalizability of calibration constants derived from our methods for dates prior to the launch of MODIS Terra.

We accessed atmospherically corrected and cloud-masked MODIS Terra SST (M_{SST}) datasets from the NASA Ocean Color website (http://oceancolor.gsfc.nasa.gov/). These datasets, computed at a 1km resolution, are known for their efficacy and accuracy in measuring SST (Minnett, 2010). We specifically chose MODIS Terra over MODIS Aqua as its overpass (typically between 10:30-11:30 AM local time) overlaps that of L5, L7, L8, and L9. This ensures minimal temporal discrepancy, ranging from near-instantaneous to a maximum of about two hours, between the image captures of the two satellites. MODIS imagery past 2023 is unreliable due to orbital drift from superseding its expected operational lift time and running out of fuel for orbit adjustment (Twedt et al., 2023). As a result, we only calibrate images from the MODIS mission start date until January 1st, 2023.

2.3 Brightness Temperature to Sea Surface Temperature Calibration

In the first step of our method, we calibrate Landsat (L7, L8, & L9) B_t to SST using M_{SST} data from the same date. For each Landsat-MODIS image pair, we calculate Pearson's correlation coefficient r to assess the linear correlation between the SST value of each MODIS pixel and the median value of all spatial coinciding Landsat B_t pixels within that MODIS pixel's area. We then exclude any M_{SST}/B_t pairs that deviate by more than one standard deviation and recalculate the correlation. This process is iterated until the correlation coefficient stabilizes or decreases. Following this, we apply the derived best fit square linear equation to convert Landsat Bt data into SST images. To calculate the best fit linear equation, ordinary least squares (OLS) regression was used.

This first step builds on Thomas et al.,(2002) and Snyder et al.,(2017), differing by using the median Landsat pixel value within each MODIS pixel area, rather than pairing the nearest Landsat pixel to the nearest MODIS pixel, aiming to reduce pixel heterogeneity and improve accuracy. This calibration step is referred to as "per-image calibration" in this study.

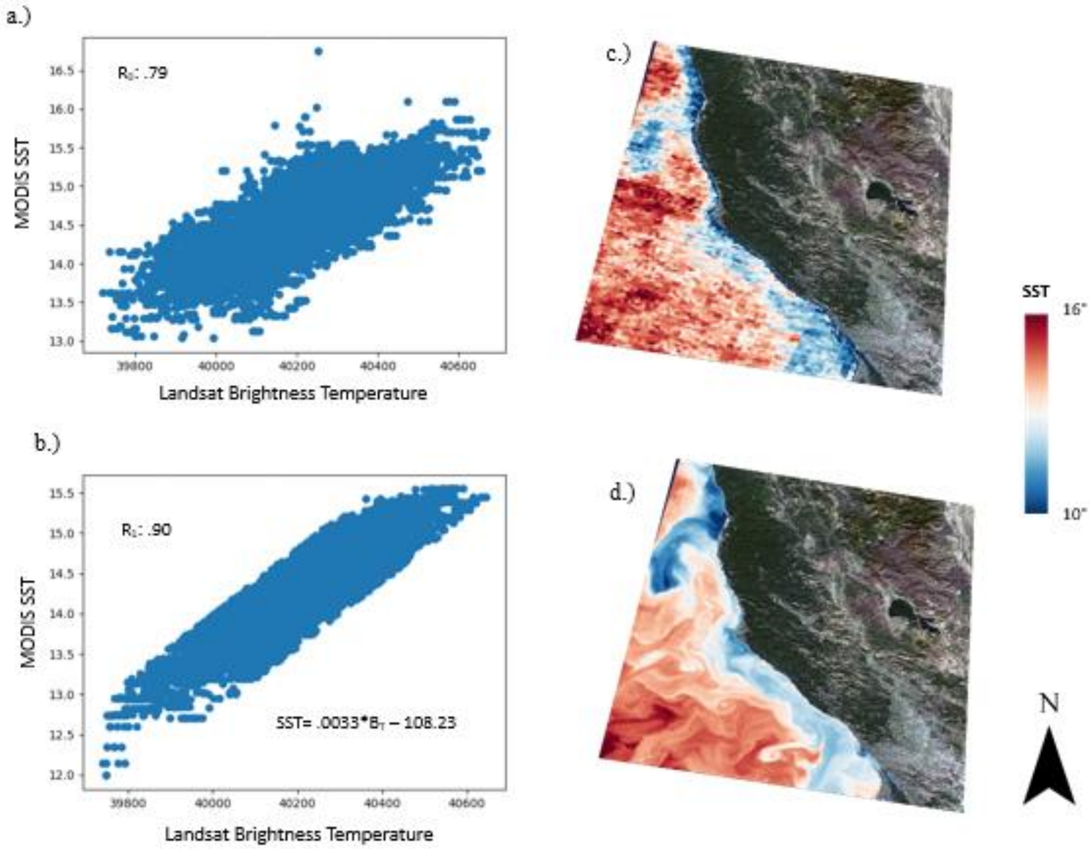

Fig. 3: Example of calibration methodology of Landsat B_t to SST using Coincidental MODIS Terra SST data from images captured on November 8, 2001. a.) Initial correlation between MODIS SST pixels and respective pixel-area median Landsat B_t pixel values from the 01/07/2015. b.) Final correlation after iterative outlier removal as outlined in section 2.3. c.) MODIS Terra SST Image from 01/07/2015. d.) Estimated Landsat SST obtained by calibrating Landsat Bt values with the best fit linear equation from plot b.

As noted in Snyder et al., 2017, this process assumes that atmospheric conditions are uniform across the Landsat scene and that atmospheric and oceanic conditions do not significantly vary between MODIS and Landsat image captures. Further, as each Landsat scene is captured in scans rather than instantaneously, this method assumes atmospheric and oceanic conditions do not significantly change during image collection, however scans last only a few seconds.

Using this process, we can categorize images as acceptable or not, by examining Bt-M_{SST} correlation strengths. For this study, we considered the image dataset in two groupings, one overall "all data" group and an idealized (R_0) group. For the "all" dataset, we use data in which the final r value between M_{SST} and B_t is above 0.7, therefore disregarding data that had too many image artefacts to successfully calibrate to SST from B_t. For R_0 data, we group calibrated Landsat images where the initial r value between M_{SST} and B_t is above 0.7, prior to iterative outlier removal. This differs from past uses of "per-image" calibration; we did not manually select images by visual inspection and instead conditionally removed or maintained within the dataset due to correlative strength, cutting down significantly on time spent on data curation and utilizing images that may have been overlooked.

The next step of the calibration methodology is creating a simple, linear general equation to apply to uncalibrated Landsat B_t images. This is done to resolve heterogeneity that may arise in the unsupervised "per-image" calibration leading to inadequate temperature calibration, due to outlier pixels not removed from the dataset. Further, it can be used to calibrate images outside of the sample dataset, as per-image calibration is computationally expensive and limited to times when MODIS data are available. This equation is aggregated from statistics of the M_{SST}-B_t normalized images from the per-image step to apply across all images. To do so, we use the median slope (m) and intercept (b) of all R_0 linear calibration equations to get:

$$SST = m * B_t + b \qquad \text{eq.2}$$

where SST is the estimated sea surface temperature and B_t is the brightness temperature at a given pixel position. This is the first time such a calibration method utilizing per-image calibration statistics has been employed that the study is aware of. This calibration method is referred to as "generalized calibration" within this study.

This generalized equation is applied to all L2 Landsat B_t images in the data set, as well as tested as a method to estimate Landsat derived SST on images outside of the dataset without coincident MODIS data (prior or past operational extent). For the latter application, we test data preceding the launch of MODIS Terra using L5 data and data using Landsat 8 and 9 data after January 1st, 2023. We resampled L5 resolution to 100m using bilinear interpolation prior to calibration to match the resolution of the study's Landsat 7-9 dataset. Calibrated Landsat 5 data were then compared with coincidental seawater temperature measurements at nearest pixel positions, see section 2.3 (Table 1.)

Name Coordinate Depth (D) Distance Offshore (Dist)	Type	Extent	Pixel	Count	r	$RMSE_{OLS}$	$RMSE_{1:1}$
N46014: 39.225 N, 123.980 W D: 2.0m Dist: 15.6km	Buoy	04/1981 - 05/2023	39.23078 N, 123.97424 W	All: 300 R_0:147 B_t: 323 M_{SST}:294	All: 0.83 R_0: 0.91 B_t: 0.75 M_{SST}: 0.70	All: .89 R_0: 0.62 B_t: 1.04 M_{SST}:1.13	All: 1.15 R_0: 1.06 B_t: 1.86 M_{SST}: 1.55
N46013: 38.235 N, 123.317 W D: 2.0m Dist: 23.0 km	Buoy	04/1981 - 05/2023	38.23544 N, 123.31667 W	All: 385 R_0:175 B_t:376 M_{SST}:376	All: 0.79 R_0: 0.87 B_t: 0.65 M_{SST}: .69	All: 1.04 R_0: 0.73 B_t: 1.30 M_{SST}:1.22	All: 1.25 R_0: 1.17 B_t:2.00 M_{SST}: 1.53
BML Mooring: 38.312 N, 123.083W D: 1.0m Dist: 1.0km	Buoy	09/2012 - 05/2023	38.31180 N, 123.08312 W	All: 67 R_0:40 B_t: 134 M_{SST}:40	All: 0.92 R_0: 0.92 B_t:0.87 M_{SST}: .87	All: 0.76 R_0: 0.65 B_t: 0.93 M_{SST}:0.92	All: 0.95 R_0: 1.00 B_t: 1.63 M_{SST}: 1.31
TB Mooring: 38.188 N, 122.928 W D: 1.0m Dist: 0.34km	Buoy	05/2013 - 10/2021	38.18783 N, 122.92771 W	All: 204 R_0:95 B_t: 220 M_{SST}:NA	All: 0.85 R_0: 0.92 B_t: 0.81 M_{SST} = NA	All: 1.25 R_0: 0.98 B_t: 1.41 M_{SST} = NA	All: 1.56 R_0: 1.42 B_t: 2.53 M_{SST} = NA

BML intake: 38.316 N, 123.070 W D: NA Dist: 0km	Intake	04/1988 - 05/2023	38.31539 N, 123.07324 W	All: 425 R_0:188 B_t: 451 M_{SST}:50	All: 0.73 R_0: 0.83 B_t: 0.62 M_{SST}: 0.80	All: 1.20 R_0: 0.89 B_t: 1.40 M_{SST}:1.17	All: 1.56 R_0: 1.58 B_t: 2.08 M_{SST}:1.95

Table 1. Table of buoy descriptions and respective results of comparisons between in-situ measurements and SST within MODIS (M_{SST}), all calibrated Landsat data (All) and selected optimal calibrated Landsat data (R_0) including the correlation (r) value between estimations and measurements, Root Mean Square Error of values against the Ordinary Least Square best fit line ($RMSE_{OLS}$), and Root Mean Square Error of values against the one-to-one line ($RMSE_{1:1}$). "NA" Is used as a placeholder for when category is inapplicable or data is unavailable.

2.4 Data Validation

Landsat SST derived from both per-image and generalized equation calibration steps are tested against in-situ seawater temperature (T_{insitu}) measurements from the NOAA National Data Buoy Center (NDBC) at buoys N46013 and N46013 (https://www.ndbc.noaa.gov/) and at buoys TB Mooring and BML Mooring as well as a seawater intake, BML Intake, operated by the University of California Davis, Bodega Marine Lab, Bodega Ocean Observing Node (BOON; https://boon.ucdavis.edu/) (Table 1). These buoys, which are mapped in Fig 1., are at varying distances offshore in order to capture variation within different marine bathymetries and environments (i.e. offshore, nearshore, at-shore, estuary). These distances are described in Table 1 measured to the nearest shoreline.

These in-situ data are calculated as hourly averages and compared against time series SST data from the 100m Landsat pixel position that the buoys are within. Seawater intake measurements at the BML Intake are compared against timeseries pixels nearest to the seawater intakes. From all in-situ datasets, temperature data collected closest to MODIS capture time for each date is considered in these validations. As all of these in-situ measurements are taken at depth (see Table 1), rather than at the surface, it is assumed that there will be discrepancy between the temperature of the sea water surface temperature and at in-situ sensor (Donlon et al., 2002). Further, it is assumed that sensors at further depth in the water column will have a more significant discrepancy with surface temperatures.

In lieu of those assumptions, to test the relative accuracy of our calibrations, we compare T_{insitu} with SST from the pixel position (table 1) closest to the buoy using Pearson's r correlation and with root mean square error (RMSE) from a y=x linear line ($RMSE_{1:1}$) and from the ordinary least squares (OLS) linear best fit line ($RMSE_{OLS}$) variables. We also compare in-situ measurements with surface temperature estimates from M_{SST} and B_T from coinciding dates to benchmark the relative performance of our methodology. We only use M_{SST} images from the same dates in which Landsat imagery is available in order to make a direct comparison. Landsat B_T data are not filtered by date.

We also tested the data quality across a given image by comparing the difference of T_{insitu} between buoy pairs with the difference in SST at the respective nearest pixel locations on the same dates (Fig. 9). These comparisons were then plotted to see how closely they adhered to a 1:1 relationship, with the logic that differences between T_{insitu} (ΔT_{insitu}) should be similar to those of SST (ΔSST) if data quality across an image is reliable. We tested the coherence of these pairings individually and as a combined dataset. Any data pairings with less than 10 points were omitted. This test assumes that temperature discrepancies between buoy locations should be mirrored by the discrepancies at the nearest SST pixel locations, resulting in a low RMSE1:1 or a best-fit OLS equation slope (m) close to one and intercept (b) close to zero.

3 Results

3.1 Sea Surface Temperature Calibration

Of the 659 images calibrated for SST from L7 to L9, 557 images are considered as viable for the larger “all data” dataset. On average, these images went through 9.23 iterations of outlier removal. There was no observable relationship between the number of data omission iterations and final Pearson’s r value. Of those images, 229 images were also in the “ideal” R_0 data set. Overall, initial and final correlation values between coincident B_t and M_{SST} values were generally strongest from April to September, i.e., during the spring and summer upwelling season in northern California (Fig. 4). Variation in OLS best fit linear equation constants between Landsat B_t and coincident M_{SST} were also generally lower in these seasons (Fig. 5). Similarly, slope and intercept values from these OLS best fit line equations were respectively lowest and closest to zero (closer to a 1:1 relation) during this season.

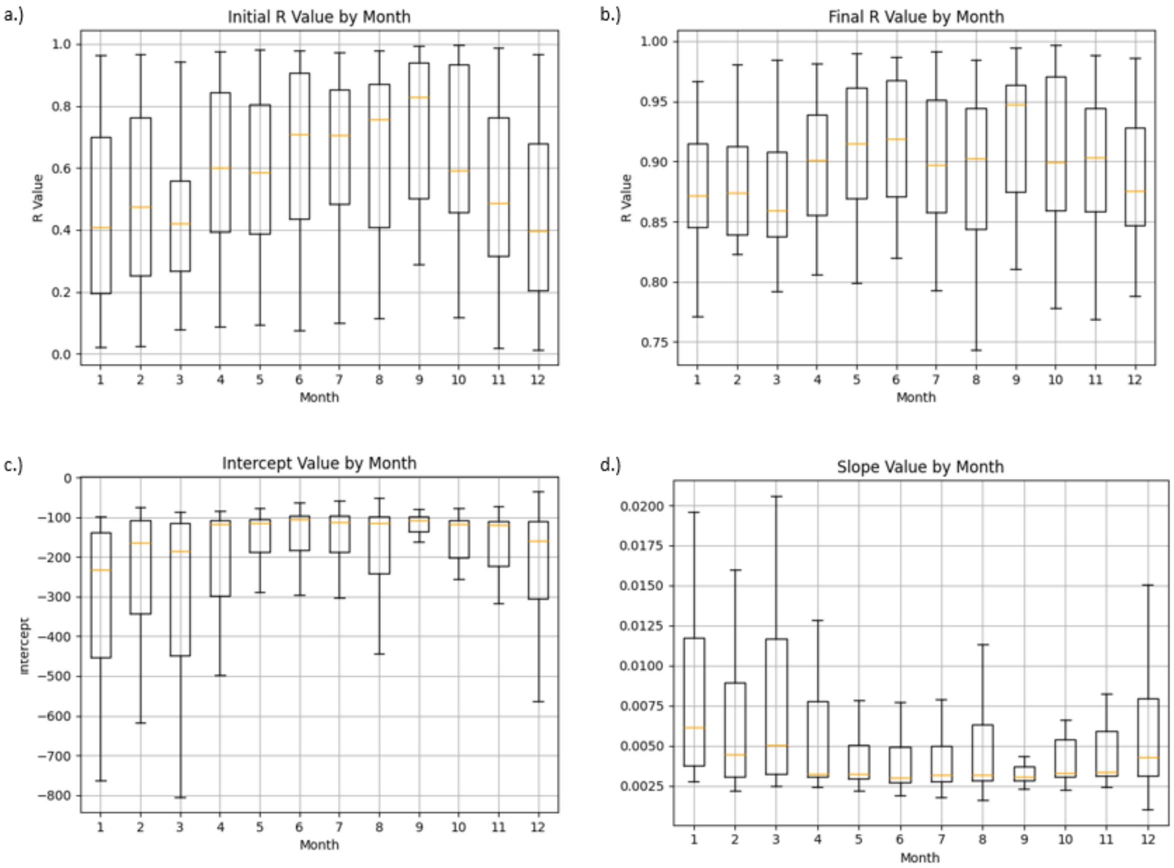

Fig. 4. Monthly box and whisker plots from calibration of all data. Box margins are lower 25th percentile of data (lower) and 75th percentile of data (upper). Orange line in box is monthly median. Whiskers show minimum and maximum values. X-axis is month in numerical format. Y axis is: (a.) Pearson's r correlation values from the first iteration of per pixel comparisons between Landsat B_t and M_{SST} (b.) Pearson's r correlation values from the final iteration of per pixel comparisons after iterative outlier removal between Landsat B_t and M_{SST} (c.) Intercept values from the OLS best fit linear equations from final iteration comparisons between Landsat B_t and M_{SST} (d.) Intercept values from the OLS best fit linear equations from final iteration comparisons between Landsat B_t and M_{SST}

The distribution of *m* and *b* values from the individual M_{SST}-B_t calibrations within the R_0 dataset are plotted in histograms in Fig. 5. From these calibrations, the median of slope values is *m*=0.00297 and the median of intercept values is *b*=105.879. These values are used in constants for Eq. 2., yielding the equation:

$$SST = .00297B_t - 105.88^{\circ}\mathrm{C} \qquad \text{eq.3}$$

This equation (Eq.3) is used to calibrate B_t to temperature within the generalized calibration step.

90% of slope and intercept values fall within 10% of each respective constant value.

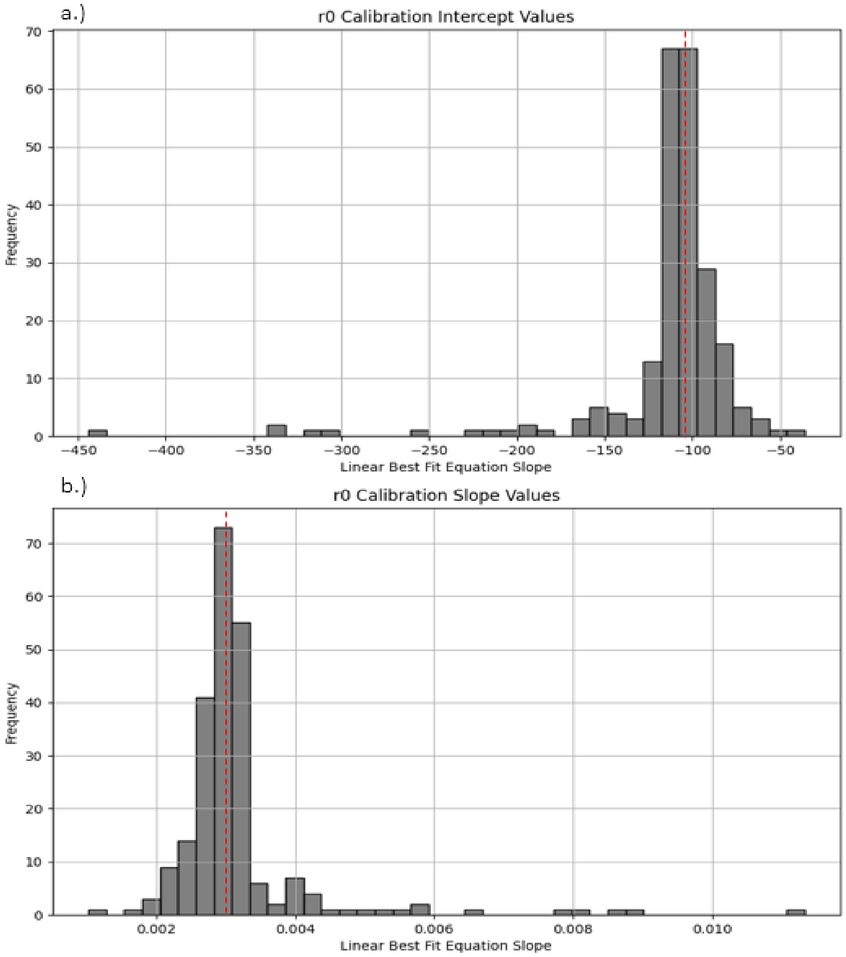

Fig. 5: (A) Histogram of intercept (b) values from per-image calibrations of R_0 data. (B) Histogram of slope (*m*) values from per-image calibrations of R_0 data. Red lines indicate distribution medians (*b*= -105.88; *m*= .00297)

3.2 Data Validation

To explore the effectiveness of calibrations from the per-image calibration step, SST from that step was compared with at each in-situ measurement location. The relative accuracy of SST , from the per-image calibration step, compared to T_{insitu} from coincidental sample measurements varies by site (Fig. 6). Within the "all" data group, performance seems to be strongest at the BML Mooring, where correlation is highest (r=0.79), error relative to the one to one line is lowest ($RMSE_{1:1}$ = 1.49°C), and error relative to the OLS line ($RMSE_{OLS}$=1.16°C) is nearly the lowest, seconded at N46014 ($RMSE_{OLS}$=1.14°C) by a difference of $RMSE_{OLS}$ =.02°C. Correlation in this group is lowest at N46013 (r=0.63), and both metric errors are highest at TB Mooring, where $RMSE_{OLS}$ =1.77°C, and $RMSE_{1:1}$ = 3.00°C. The performance of "all" data SST derived from the step is nearly comparable to B_t and M_{SST} estimates, with overall slightly lower correlation and higher error metrics except at BML Intake.

Performance of SST from the per-image step within the ideal R_0 group is notably stronger. Here, correlation is highest at both N46014 and TB Mooring (r=0.89), and error metrics are lowest at N46014 ($RMSE_{OLS}$ = 0.71°C ; $RMSE_{1:1}$ =1.04°C) Conversely, correlation with T_{insitu} is lowest at BML Mooring (r=0.82), and $RMSE_{OLS}$ (1.12°C) and $RMSE_{1:1}$ (1.36°C) are highest at TB Mooring (Fig. 6). These chosen idealized SST images are more relatively accurate against in-situ samples than temperatures from B_t and M_{SST} across all sites, with $RMSE_{OLS}$ and $RMSE_{1:1}$ being at least 0.4°C lower than either B_t or M_{SST} at most sites with the exception at the BML Mooring, where error are only 0.03°C and 0.02°C lower, respectively.

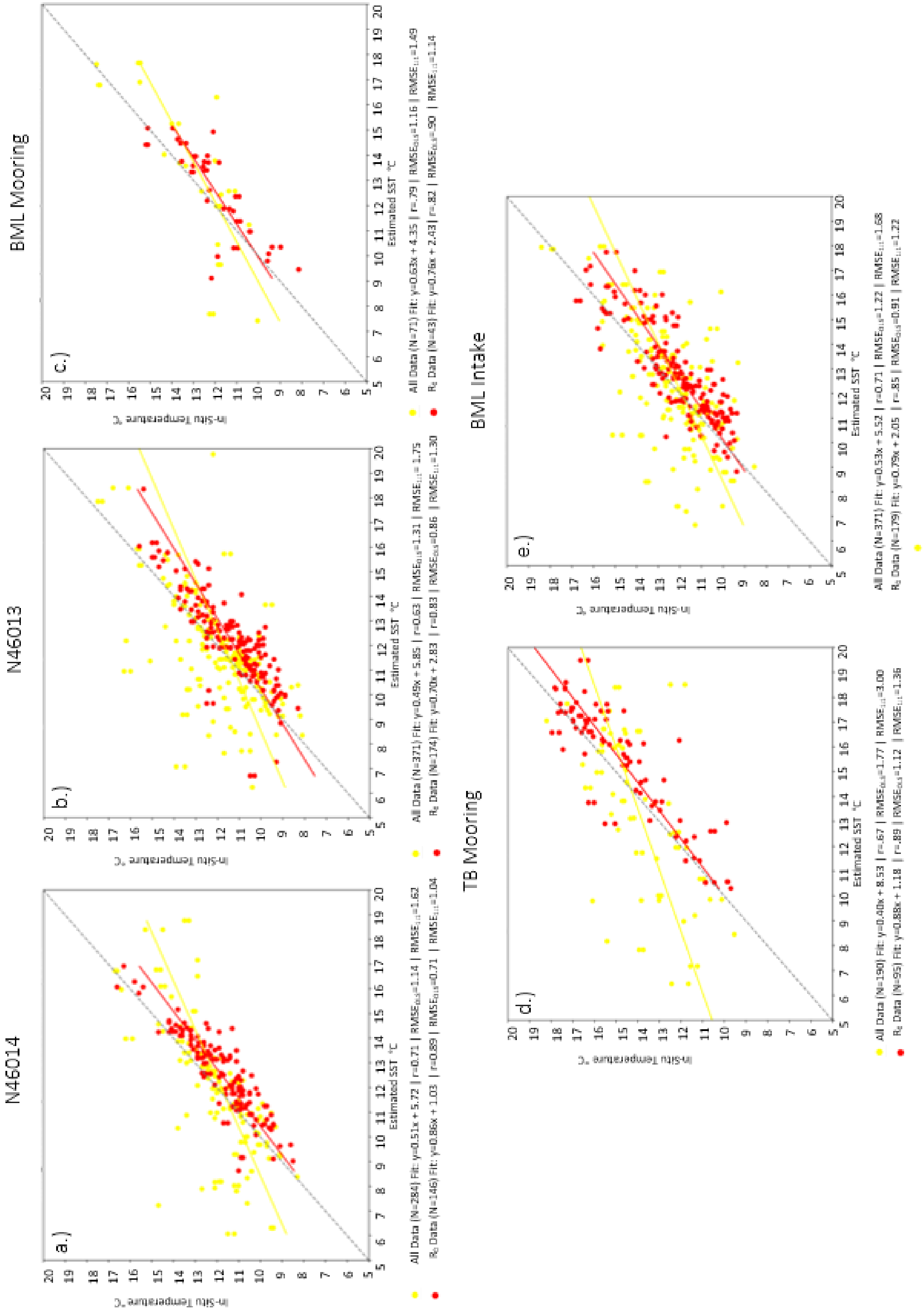

Fig. 6: SST values derived from Landsat data from the per-image calibration step plotted against water temperature measured by in-situ sensors: (a) N46014, (b) N46013, (c) BML Intake (d) TB Mooring, and (e) BML Mooring.

Validations of SST values derived from the final generalized calibration step by comparison with coincident T_{insitu} are shown in Fig 7 and Table 1, along with validation of coincidental values from B_t and M_{SST}. The performance of SST from both groupings from this step exceed those of the previous SST estimates. Within the "all" dataset, SST is most accurate with T_{insitu} values at BML Mooring, where correlation is strongest (r = 0.92) and error metrics are lowest ($RMSE_{OLS}$=0.76°C ; $RMSE_{1:1}$ =0.95°C). Correlation is weakest at N46013 (r=0.73) and error is highest at TB Mooring ($RMSE_{OLS}$=1.25°C; $RMSE_{1:1}$ =1.56°C). Performance across all metrics from this dataset outperform those from M_{SST} and Bt at each site except by $RMSE_{OLS}$ and r at BML intake.

As expected, performance is significantly stronger within the R_0 group. Correlation is strongest and at nearly the same value at sites BML Mooring, TB Mooring, and N46014 (respectively r=0.92, 0.92, 0.91). Error from the OLS line is lowest at N46014 ($RMSE_{OLS}$ = 0.62°C), only nearly succeeding data the BML Mooring ($RMSE_{OLS}$ = 0.65°C). Error relative to the one-to-one line is lowest at BML Mooring ($RMSE_{1:1}$=1.00). Correlation is weakest at BML intake (r=0.83), and error metrics are lowest at TB Mooring ($RMSE_{OLS}$ = 0.98°C) and BML Intake ($RMSE_{1:1}$ = 1.58°C). Performance across each metric is significantly stronger than that from M_{SST} or Bt at each site (Fig 7 & Table 1).

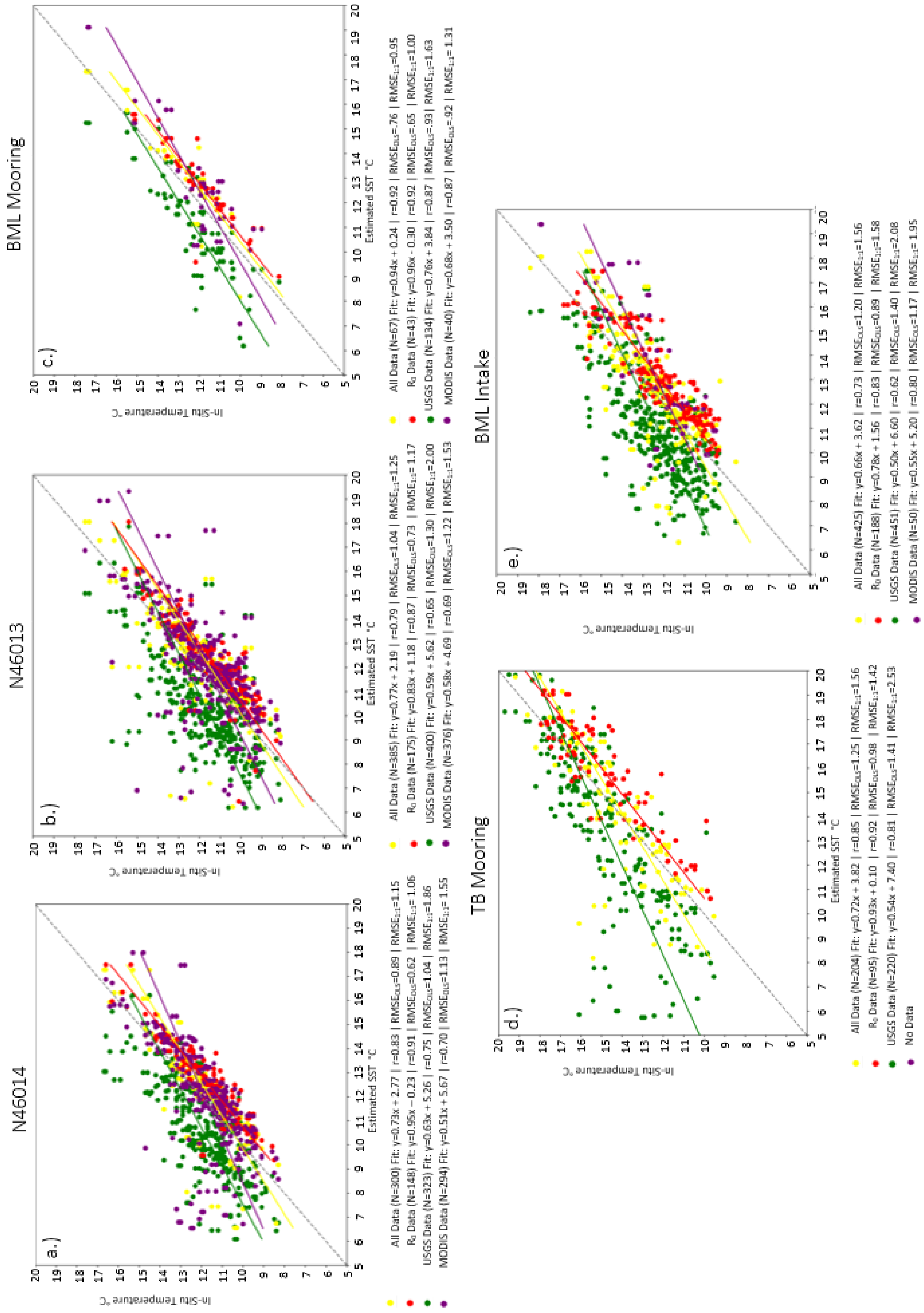

Fig. 7: SST values derived from Landsat data using aggregate calibration plotted against water temperature measured by in-situ sensors: (a) N46014, (b) N46013, (c) BML Intake (d) TB Mooring, and (e) BML Mooring.

Fig. 8 shows the differences between derived estimated SST data from the generalized calibration step and in-situ measured data at each buoy location and all buoy locations aggregated by month for both datasets.

In both datasets, across all buoys and months, SST is higher than T_{insitu}. Within the "all" dataset, across all sites, this difference is greatest within the summer months from June to August where median differences are ~1.5°C on average and smallest in December and January. TB Mooring (Fig. 8d) on a monthly basis has the highest deviation in SST-T_{insitu}, with the smallest being at N46013 (Fig. 8 b).

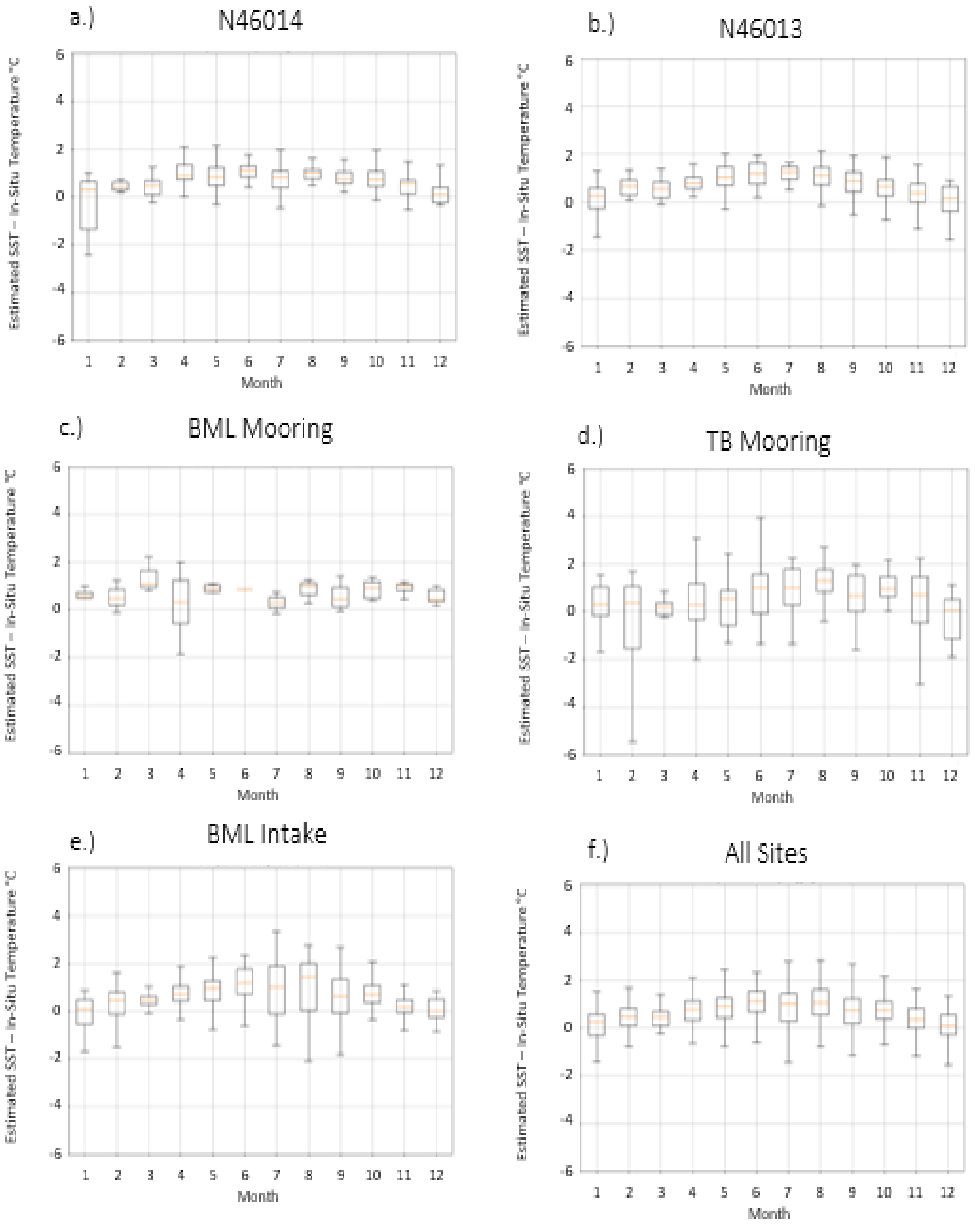

Fig. 8: Monthly box and whisker plots of difference between estimated SST and in-situ measurements across all data. Box margins are lower 25th percentile of difference (lower bound) and 75th percentile of difference (upper bound). Orange line in the box is the monthly median. Whiskers show minimum and maximum difference values. X-axis: month in numerical format. Y axis: difference between estimated SST and in-situ measurements at: (a) N46014, (b) N46013, (c) BML Intake, (d) TB Mooring, (e) BML Mooring, and (f) all buoy locations combined.

Results of in-image accuracy, examining coincident ΔT_{insitu} and respective ΔSST at given sampling sites, are shown in fig 9. As an overall comparison, differences between buoy pairs and respective pixel pairs across the “all” dataset had a correlation of r=0.84, errors of $RMSE_{1:1}$=1.23°C, and $RMSE_{1:1}$=1.31°C, and had an OLS *m*=0.88 and OLS *b*=0.36. These metrics are slightly stronger when isolated to the R_0 dataset, where r=0.88, $RMSE_{OLS}$=1.13°C, and $RMSE_{1:1}$=1.24°C. In both data groups, the site pair with the highest correlation between ΔT_{insitu} and ΔSST is between TB Mooring and N46013 (r_{all}=0.94; r_{R0} =0.91). The lowest error metrics are found between BML Intake-BML Mooring, however, most differences between the two sites are near zero, likely due to the close proximity of the two sites. In the “all” dataset, the spatially distributed site with the lowest error is BML Intake-N46014 ($RMSE_{OLS}$=1.96; $RMSE_{1:1}$=1.24°C), and in R_0 dataset, N46013-N46014 ($RMSE_{OLS}$=0.91 $RMSE_{1:1}$=0.99°C).

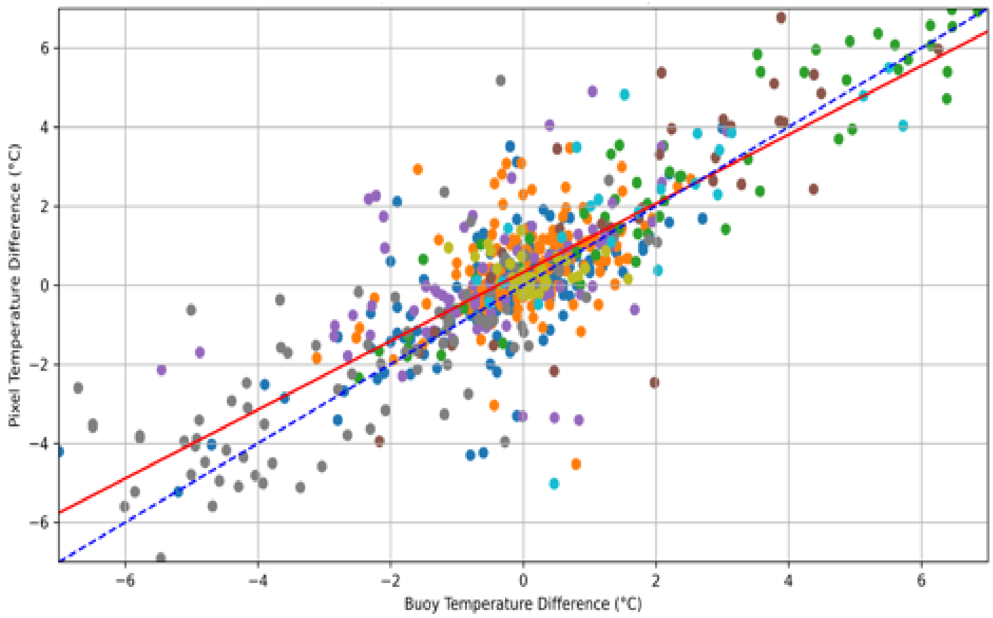

Buoy Pair	n	OLS Equation	R	$RMSE_{OLS}$	$RMSE_{1:1}$
● N46013 – N46014	All:130 R_0: 70	All: y=0.75x +.06 R_0: y=0.77x -.04	All: 0.72 R_0: 0.81	All: 1.02 R_0: 0.91	All: 1.09 R_0: 0.99
● BML Intake – BML Mooring	All: 35 R_0: 19	All: y=-0.08x +0.27 R_0: y=-0.07x +0.31	All: -0.11 R_0: : -0.11	All: 0.35 R_0: 0.39	All: 0.65 R_0: 0.75
● BML Intake – TB Mooring	All: 80 R_0: 39	All: y=0.76x -0.21 R_0: : y=0.70x -0.52	All: 0.77 R_0: 0.76	All: 1.41 R_0: 1.24	All: 1.54 R_0: 1.43
● BML Intake – N46013	All: 125 R_0: 64	All: y=0.55x +0.51 R_0: y=0.53x +0.70	All: 0.48 R_0: 0.49	All: 0.96 R_0: 0.97	All: 1.14 R_0: 1.23
● BML Intake – N46014	All: 85 R_0: 48	All: y=0.48x + 0.43 R_0: : y=0.53x + 0.57	All: 0.52 R_0: 0.68	All: 1.27 R_0: 1.04	All: 1.67 R_0: 1.57
● TB Mooring– N46013	All: 55 R_0: 24	All: y=0.96x +0.37 R_0: y= 1.01x +0.23	All: 0.94 R_0: 0.91	All: 0.90 R_0: 0.95	All: 0.95 R_0: 0.98
● TB Mooring– N46014	All: 36 R_0: 19	All: y=1.16x +0.18 R_0: : y=0.95x +0.78	All: 0.86 R_0: 0.86	All: 1.57 R_0: 1.39	All: 1.69 R_0: 1.23
● TB Mooring– BML Mooring	All: 21 R_0: 13	All: y=0.98 x+0.33 R_0: : y=0.86x + 0.62	All: 0.69 R_0: 0.84	All: 1.66 R_0: 1.03	All: 1.69 R_0: 1.12
All Pairs	All: 567 R_0: 296	All: y=0.88x + 0.36 R_0: y=0.88x + 0.41	All: 0.84 R_0: 0.88	All: 1.23 R_0: 1.13	All: 1.31 R_0: 1.24

Fig. 9: Plot and table of buoy respective closest pixel pair deviations. Plotted data points are colored by data pairings as indicated in the table. Table metrics include data count (n), the equation of the ordinary least squares (OLS) best fit linear equation line, the Pearson correlation between buoy and pixel differences (R), the root mean square error of points from the ordinary least squares line ($RMSE_{OLS}$), and the root mean square error of points from the one-to-one line ($RMSE_{1:1}$). In cells, metrics following “All” and “R_0” are derived from those respective datasets.

4. Discussion

4.1 Image Calibration

In our study, we develop and assess a methodology for aggregating and refining correlation data between ideal, coincidental Landsat and MODIS data to scale Landsat B_t data for enhanced SST remote sensing, particularly within nearshore environments where fine scale processes require such capabilities. Analyses comparing SST estimated by our study's methodology, standard MODIS SST data, and standard USGS Level 2 Landsat B_t data against coincident in-situ buoy and seawater intake data emphasize the effectiveness of our approach. This methodology not only enhances the overall estimation of SST in our region but also allows for the semi-objective selection of ideal imagery.

Per-image calibration, when applied as a standalone process to our minimally filtered dataset, showed mixed reliability. The correlation and $RMSE_{OLS}$ between T_{insitu} and SST from all per-image calibrated datasets (Figure 6) were comparable, if not slightly lower by a margin of hundredths, compared to land-calibrated B_T data. However, the $RMSE_{1:1}$ error from this dataset was generally lower than the B_T data, except at TB Mooring, where $RMSE_{1:1}$ was higher by 0.47 °C. Conversely, $RMSE_{1:1}$ at BML Mooring, which is only 1 km offshore, and BML Intake, located at the shoreline, was lower than B_T by -0.14 °C and -0.4 °C, respectively. Considering that past studies have employed similar calibrations to estimate T_{insitu} from SST, these results suggest that unsupervised per-image calibration may only conditionally yield lower error than using B_T data. However, accuracy should be applied with spatially diverse sampling, particularly in nearshore environments. Similarly, using minimally supervised per-image calibration is only conditionally advantageous over M_{SST} as a temperature gauge. However, it is useful in areas where data is unavailable from MODIS, such as at TB Mooring, or in very close shore environments like BML Intake, where SST from all per-image calibrated data is lower than M_{SST} by -0.27 °C. While M_{SST} has lower $RMSE_{1:1}$ than this dataset at the nearshore BML Mooring by -0.18 °C, it has lower data availability by n=21 dates.

However, with the selection of ideal images within the R_0 grouping, per-image calibration demonstrates higher accuracy, with increased correlation and reduced error compared to both USGS Level 2 BT data and MODIS SST (Figure 6). The correlation and $RMSE_{OLS}$ of SST compared to T_{insitu} are comparable to, or greater than, those of M_{SST} and B_T, and $RMSE_{1:1}$ is less than B_T at each sampling location. Notably, at closest to shore, TB Mooring and BML Intake, errors are lower than B_T by -1.17 °C and -0.86 °C, and lower than M_{SST} by -0.73 °C at BML Intake (with M_{SST} data unavailable at TB Mooring).

The per-image calibration step not only proved efficient for selecting ideal images to form the R_0 dataset—a task traditionally performed manually and often arduous—but also facilitated the creation of a second calibration step. SST from the generalized equation calibration step had superior accuracy with T_{insitu} across all metrics at each site in the "all" data set, and to an even greater success within the R_0 dataset, across areas offshore and nearshore compared to B_T and M_{SST} data. Again, $RMSE_{1:1}$ error at TB Mooring was especially lower, with a reduction of error by -1.11 °C. Overall, the generalized equation set had a more even performance of all data, contextualized by the R_0 dataset, in the second step as opposed to the first step of calibration. For instance, across the two SST datasets in the per-image step, R_0 had an average correlation of r=0.154 higher than the "all" dataset, reduction in $RMSE_{OLS}$ of -0.31°C, and reduction in $RMSE_{1:1}$ of -0.46°C. In the generalized equation step, R_0 had an average correlation of r=0.07 higher than the "all" dataset, reduction in $RMSE_{OLS}$ of -0.25°C, and reduction in $RMSE_{1:1}$ of -0.048°C. This indicates that selective image calibration may not be necessary once the generalized equation is formed, as results across most metrics do not become significantly more accurate. This greatly increases the scope of the dataset, which is necessary for fine nearshore environments that exhibit high variability (Speiser and

Largier, in submission). Further, this suggests that future data calibration could be conducted independently of MODIS data using these constants, extending to Landsat B_T data before the launch of the MODIS Terra satellite and after its reliable data quality window, as data selection using coincident MODIS becomes unnecessary. For example, as demonstrated in Fig. 10, we have applied the generalized equation calibration to Landsat 5 data spanning from 1984 to 2000, which predates the MODIS Terra launch, and to Landsat 8 and 9 data beyond 2023. Validations from in-situ buoy data in these plots show that these data, not used within the formation of the general calibration constants, are comparable in correlation, $RMSE_{1:1}$, and $RMSE_{OLS}$ with validations from the 2000-2023 dataset. Results within this figure show that hindcast Landsat 5 data is better fit with in-situ measurements than forecast data; however, the forecast dataset has a significantly smaller sample size, which may not be adequate for analysis of overall methodological success. Given the applicability of this methodology with data uninvolved in the creation of the calibration constants, one may assume that the application of this calibration equation may be applicable at sites similar to that of WRS tile path 45 row 33.

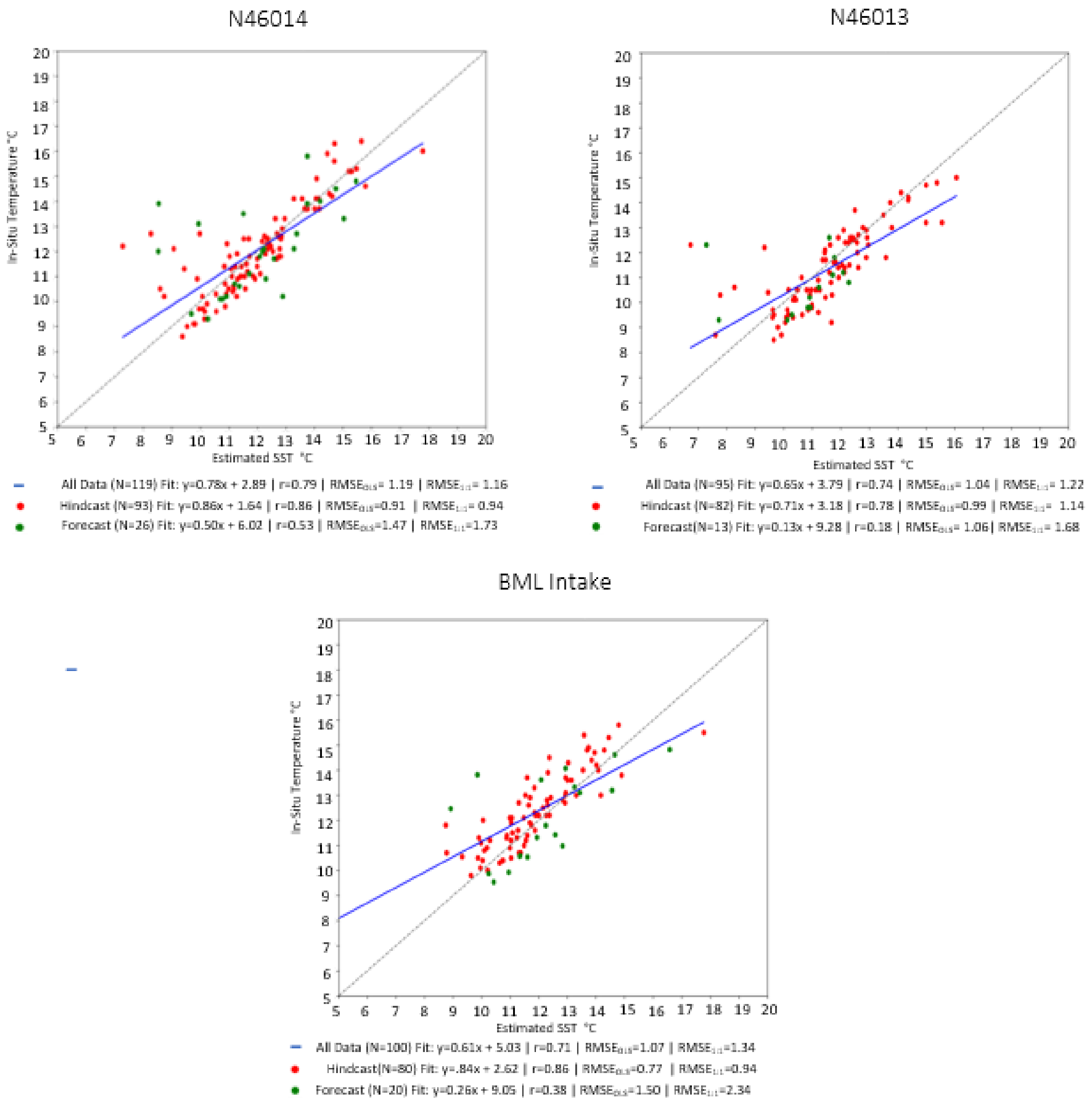

Fig. 9: Plots of general eq calibrated data applied to Landsat 5 BT data (x-axis) compared to in-situ measurements using the sensors noted in titles. Green data points are "forecast" data of L8 & L9 data captured after 2023. Red data points are "hindcast" data of L5 data captured prior to 2000. Blue trend line is the OLS best fit linear equation from both hindcast and forecast data.

Superior performance of a generalized empirical equation composited from information of ideal image pairs is expected, as any calibration equations that were ill-adjusted from unresolved artifacts are likely dampened when aggregated amongst other calibrations. This can perhaps be best seen in Fig. 4c and Fig. 4d, where although there may be large deviations within slope and intercepts of calibration equations, particularly within the winter months, which are seasons with higher cloud cover within the region, the mean of those distributions still lies relatively closer to those of the summer months which had lower deviation ranges. However, it should also be noted that there is less data within these latter summer months, as shown in Fig. 2.

This ability to retrospectively apply the generalized calibration constants to historical satellite data not only validates the robustness and utility of the derived calibration constants but also broadens the potential for enhancing the temporal scope of more accurate SST analyses. Such advancements can contribute to long-term climatological and environmental studies by providing more accurate SST measurements over extended periods, thereby offering valuable insights into historical ocean temperature patterns and trends.

Overall, there exists strong variation in accuracy between T_{insitu} and SST per site (Fig. 7) and by season (Fig. 8). However, this added context informs these results. The overall lowest correlation and highest error occurred at BML Intake. However, the intake is at a fixed depth that does not adjust with tidal level, so at maximum depth, temperature likely varies significantly from skin temperature (Donlon et al., 2002; Minnett et al., 2020). Further, the second-highest error exists at the TB Mooring in Tomales Bay, which is a low-inflow estuary. Beyond shallow bathymetry in the outer Bay, this site may experience heightened stratification due to decreased mixing from tides (Largier et al., 1997). Stratification may also be the reason for higher overall dataset error in summertime (Figure 8; Largier et al., 1993). Lack of variation in performance between the two highest-performing sites, the farthest offshore site, N46013, and the closest nearshore marine mooring, BML Mooring, which both have the highest correlations and lowest errors of any site, highlights the performance of our methodology in enhancing SST in both nearshore and offshore environments.

Tests of in-image accuracy in Fig. 9 were weaker than one might expect. However, it should be taken into consideration that in each site pair, sensor instrument methodology differs, making it likely that ΔT_{insitu}, measured at different depths by different instruments, behaves differently than ΔSST, which is all measured at the surface. Further, the only pair with the two same instruments and the largest sample size was N46013-N46014, which was the pair with the lowest error (besides TB Mooring-N46013, which had a significantly smaller sample size). Even then, the sites are far away from one another, so sensor-at-depth temperatures may vary with tide, and stratification effects at the two sites may act differently (Palacios et al., 2004)

This ability to retrospectively apply the generalized calibration constants to historical satellite data not only validates the robustness and utility of the derived calibration constants but also broadens the potential or enhancing the temporal scope of more accurate SST analyses. Such advancements can contribute to long-term climatological and environmental studies by providing more accurate SST measurements over extended periods, thereby offering valuable insights into historical ocean temperature patterns and trends.

4.2 Observation and Use Cases

High-resolution SST data allows the observation of small-scale, nearshore processes that are too fine for detection with moderate resolution data products like GOES or MODIS. This enhancement enables the study of phenomena such as rip currents and their impact on temperature patterns in the nearshore. Moreover, it facilitates the observation of various non-turbid dynamics, irrespective of their size, which are typically not observable in visual-optical/color satellite radiances. Examples include clear river plumes, tidal outflows from bays and estuaries, and fine-scale eddies.

Fig. 10d showcases these features, where cold plumes align with the shapes and locations of small, turbid rip currents visible in high resolution true color imagery along the Pt. Reyes Seashore.

The calibrated high-resolution SST in this figure also illuminates the shapes and extents of non-turbid mixing processes, manifesting as small, clear river plumes (Fig 10b) and tidal bay outflows (Fig 10c)

While these processes can be initially identified through gradients in uncalibrated brightness values, calibration allows estimates of the temperatures of these features. Additionally, it provides a clearer understanding of the magnitude of temperature differences between these mixing features and the surrounding marine waters, which could not be verified with uncalibrated brightness temperature values.

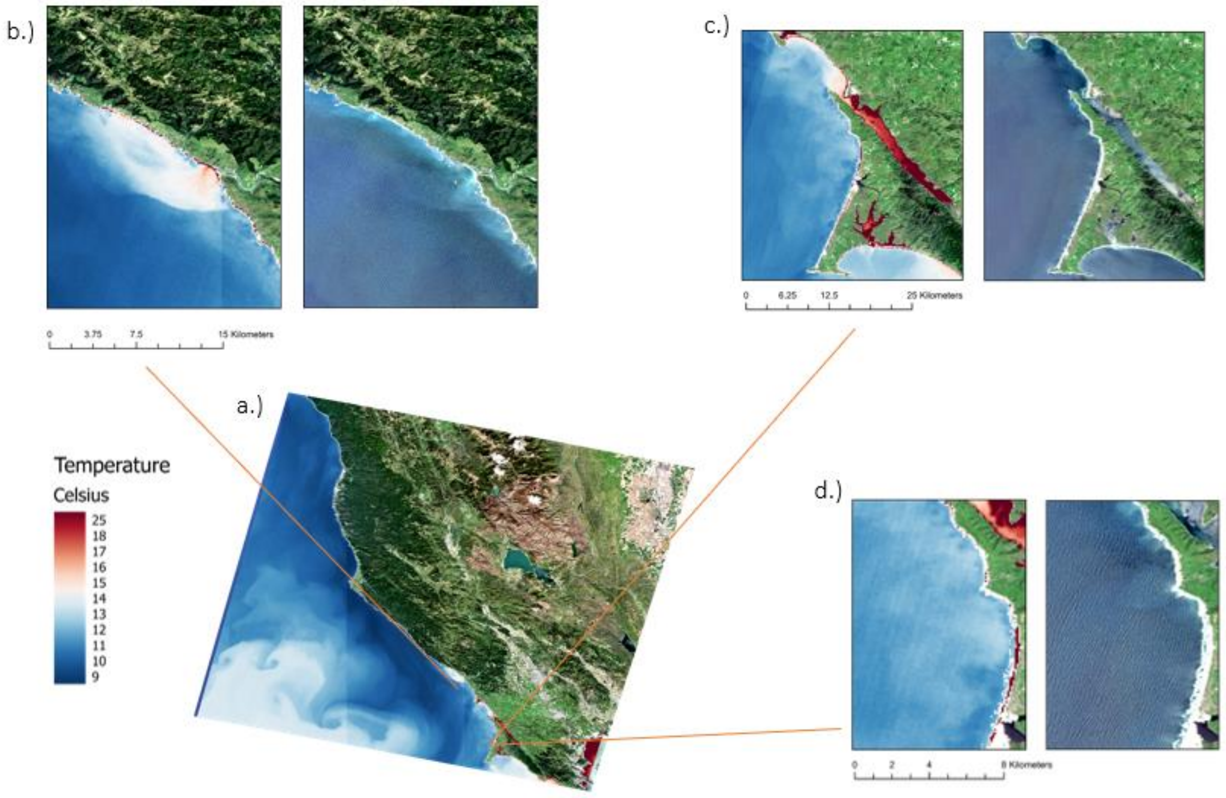

Fig. 10: Mapped temperature from 04/25/2019 vs true color values at zoomed in sites. Color scale adjusted to highlight all temperature features. a) entire calibrated SST image. b) zoomed in calibrated SST (left) and true color imagery (right) directly west of the Russian River estuary c) zoomed in calibrated SST (left) and true color imagery (right) North of the Pt. Reyes National Seashore and south of Bodega Bay. d) zoomed in calibrated SST (left) and true color imagery (right) of the north headland of Point Reyes national seashore

The capability to sample SST with high spatial resolution and moderate frequency enhances the ability to monitor regions where regular in-situ data collection is challenging, such as the immediate, and often rocky, nearshore areas. This facilitates novel observational studies and research projects, some of which might not have been feasible previously possible as unbeknownst to this study.

For instance, an application of this methodology where previous investigation is unknown to this study is the investigation of SST patterns and disparities between the close nearshore areas and further offshore. Fig. 11 showcases the potential of high-resolution SST towards such a subject, presenting plots of SST calculated with the per-image calibration methodology against distance offshore. These plots are based on a single cross-shore transect in Manchester Bay, observed in June across three different years using per-image temperature calibration. Interestingly, even though the observations were made at the same location and during the same season, the temperature gradients along this transect showed varying trends – warming, cooling, or displaying a parabolic shape with increasing distance from the shore.

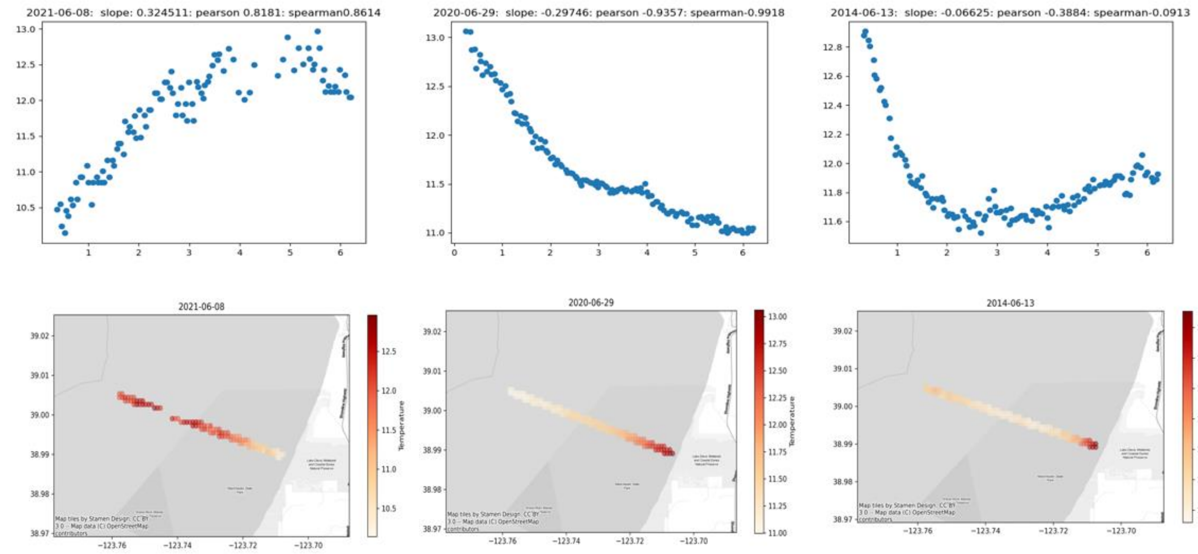

<u>Fig. 11:</u> Cross-shore temperature profiles from a transect at Manchester Beach, CA extending 6.5km offshore from a per-image calibrated images. **<u>Top:</u>** Plots of temperature (y-axis) vs distance (x-axis) **<u>Bottom:</u>** Mapped temperature values from dates respective to plots in the same column.

Utilizing high-resolution SST data that we can derive at various estimated accuracies and timescales as far back as 1984, we can discern detailed temporal patterns oceanography and potentially climatology across large regions by analyzing SST metrics at each pixel location. Fig. 12 illustrates this by presenting the mean SST at each pixel position of all calibrated L5 to L9 data.

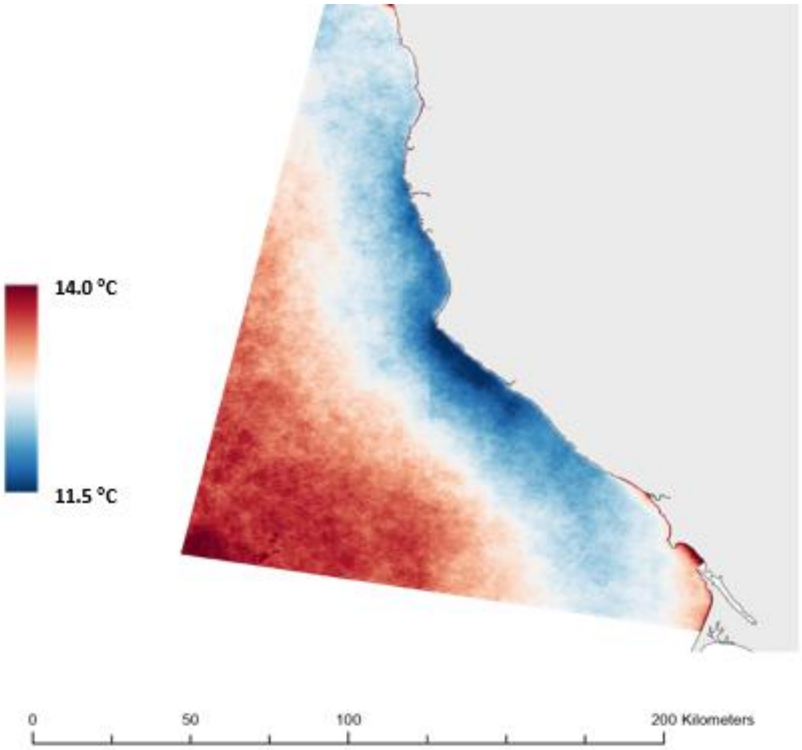

Fig. 12: Average temperature at each pixel position in Landsat data from 1983-2024 in degrees Celsius calibrated using general calibration equation constants.

From the results in Fig. 12, high-resolution data reveals areas with the warmest and coldest average SST derived from our methodology. From this one can make observations such a large cool region near Point Arena which aligns with a region of significant upwelling (Largier et al., 1993; Garcia-Reyes and Largier, 2012). This upwelling area is now mapped with an unparalleled resolution. Another cooler area, potentially linked to upwelling, is observed near Fort Bragg. Regions like the coast between Bodega Bay and north of Tomales Bay, and in front of the Russian River, and in front of Pt Reyes seashore, which is impacted by tidal outflow from Tomales Bay (Roughan et al., 2005), Bodega Bay (Morgan et al., 2021), and SF Bay (Wing et al., 1995) are discernibly warmer, emphasizing the influence of bays and estuaries with marine water mixing and temperature. The temperature gradients along broad, north-facing beaches such as Ten Mile, Manchester, Salmon Creek, and Point Reyes Seashore, all with warmer nearshore gradients, might indicate the role of fine-scale, nearshore processes in SST mixing or the effects of shallow bathymetry on local marine temperatures.

5. Conclusions

In our research, we develop, validate, and apply a two-step methodology for deriving water surface temperature from Landsat land brightness temperatures in WRS tile path 45 row 33 using associated MODIS Terra SST data. By deriving calibration constants from relationships between coincident MODIS Terra and Landsat data, we can calibrate data prior to, during, and after the operational extent of reliable MODIS Terra SST data. For validation, we tested our calibrated data against in-situ temperature measurements collected from sensors at various distances offshore within the study area and compared these validations against those with values from uncalibrated USGS Landsat Land brightness temperatures and coincident MODIS SST. We find success in these calibrations, with superior accuracy against in-situ measurements than the off-the-shelf USGS product and even coincident MODIS SST data. For a minimally filtered dataset (n=557 images), the RMSE against the OLS line ranges between 0.76 to 1.20 °C, the RMSE against the 1:1 line ranges between 0.95 to 1.56 °C, and correlation coefficients range from r=0.73 to 0.92. These metrics are further enhanced when looking at comparisons within our R_0 dataset (n=229), which consists of optimal images whose selection was enabled by our methodology. This dataset has an RMSE against the OLS line ranging between 0.62 to 0.98 °C, an RMSE against the 1:1 line ranging between 1.00 to 1.58 °C, and correlation coefficients ranging from r=0.83 to 0.92. Further, we find that error within images against in-situ data is temporal and regional, likely borne of local and seasonal effects such as stratification.

The first step of our method enhances existing techniques for calibrating single image Landsat brightness temperature to SST using coincident MODIS data and extends its application across hundreds of images rather than isolated dates. This "per-image" calibration approach, while showing variable performance across the dataset, was shown to be particularly beneficial for selecting and calibrating images with inherently higher correlations to MODIS data. This method allowed for significant improvements in SST estimation accuracy, achieving reductions in $RMSE_{OLS}$ and $RMSE_{1:1}$ and an increase in correlation at most in-situ measurement locations.

Moreover, the implementation of the second methodological step, a generalized equation calibration methodology based on constants derived from median statistics of the best-fit correlation equations from data derived from and selected with the first methodology, has uniformly enhanced data correlation across the dataset with buoy readings both nearshore and offshore. This methodology's strength lies in its ability to resolve inaccuracies potentially introduced by artifacts such as undetected clouds and shadows, which can adversely affect per-image calibrations. The resulting data quality, closely aligned with in-situ measurements, underscores the value of a generalized approach in achieving more consistent and accurate SST estimations. The use of optimal calibration constants for the study site that surpass the performance of standard B_t data presents a promising avenue for future SST measurement calibrations within the region. This strategy enables future calibrations to be conducted independently of MODIS data, potentially simplifying the calibration process, and extending its applicability to historical B_t data collected before the MODIS Terra satellite launch.

The goal of this paper is to provide an easily applied and replicable methodology for optimizing SST data for nearshore observation. Future work should focus on testing these calibration constants against similar regions to assess the broader applicability of this methodology for comparable climatic conditions. This would help validate the robustness of the approach and extend its utility to other coastal areas with similar oceanographic characteristics, such as upwelling regions along western continental boundaries. Additionally, further investigation into the impacts of stratification on the calibration methodology could help refine and enhance future efforts in deriving high-resolution SST data from satellite imagery. Understanding how vertical temperature gradients in the water column affect the relationship between satellite-derived SST and in-situ measurements at different depths would enable more accurate calibrations and improved error characterization. Using these calibrated datasets, potential use cases across various spatial and temporal scales are showcased, demonstrating promise for approaching questions previously unable to be effectively pursued, or enhancing the detail of prior knowledge obtained with coarser, moderate-resolution SST data. High-resolution SST data prove invaluable in observing lesser-known nearshore processes, which have significant implications for coastal water quality management. These showcased use cases can individually be expanded upon to address many specific, important, and understudied questions in future efforts.

Acknowledgements

Gonzalo Saldías and Yufang Jin are thanked for their feedback contributing to methodology within the manuscript.

References

Albanai, J. A., & Abdelfatah, S. A. (2022). Accuracy assessment for Landsat 8 thermal bands in measuring sea surface temperature over Kuwait and North West Arabian Gulf. *Kuwait Journal of Science*, *49*(1).

Basdurak, N. B., Largier, J. L., & Nidzieko, N. J. (2020). Modeling the dynamics of small-scale river and creek plumes in tidal waters. *Journal of Geophysical Research: Oceans*, *125*(7), e2019JC015737.

Behrens, D. K., Bombardelli, F. A., Largier, J. L., & Twohy, E. (2013). Episodic closure of the tidal inlet at the mouth of the Russian River—A small bar-built estuary in California. *Geomorphology*, *189*, 66-80.

Chadwick, D. B., Largier, J. L., & Cheng, R. T. (1996). The role of thermal stratification in tidal exchange at the mouth of San Diego Bay. *Buoyancy effects on coastal and estuarine dynamics*, *53*, 155-174.

Chadwick, D. B., & Largier, J. L. (1999). Tidal exchange at the bay-ocean boundary. Journal of Geophysical Research: Oceans, 104(C12), 29901-29924.

Donlon, C. J., Minnett, P. J., Gentemann, C., Nightingale, T. J., Barton, I. J., Ward, B., & Murray, M. J. (2002). Toward improved validation of satellite sea surface skin temperature measurements for climate research. Journal of Climate, 15(4), 353-369.

Feng, L., & Hu, C. (2017). Land adjacency effects on MODIS A qua top-of-atmosphere radiance in the shortwave infrared: Statistical assessment and correction. *Journal of Geophysical Research: Oceans*, *122*(6), 4802-4818.

Fisher, J. I., & Mustard, J. F. (2004). High spatial resolution sea surface climatology from Landsat thermal infrared data. Remote Sensing of Environment, 90(3), 293-307.

Foga, S., Scaramuzza, P. L., Guo, S., Zhu, Z., Dilley, R. D., Beckmann, T., Schmidt, G. L., Dwyer, J. L., Hughes, M. J., & Laue, B. (2017). Cloud detection algorithm comparison and validation for operational Landsat data products. Remote Sensing of Environment, 194, 379-390.

Fu, J., Chen, C., Guo, B., Chu, Y., & Zheng, H. (2020). A split-window method to retrieving sea surface temperature from Landsat 8 thermal infrared remote sensing data in offshore waters. *Estuarine, Coastal and Shelf Science*, *236*, 106626.

Garcia-Reyes, M., & Largier, J. L. (2012). Seasonality of coastal upwelling off central and northern California: New insights, including temporal and spatial variability. Journal of Geophysical Research: Oceans, 117(C3).

Gorelick, N., Hancher, M., Dixon, M., Ilyushchenko, S., Thau, D., & Moore, R. (2017). Google Earth Engine: Planetary-scale geospatial analysis for everyone. Remote Sensing of Environment, 202, 18-27.

Halle, C. M., & Largier, J. L. (2011). Surface circulation downstream of the Point Arena upwelling center. *Continental Shelf Research*, *31*(12), 1260-1272.

Horner-Devine, A. R., Hetland, R. D., & MacDonald, D. G. (2015). Mixing and transport in coastal river plumes. Annual Review of Fluid Mechanics, 47, 569-594.

Jang, J., & Park, K. A. (2019). High-resolution sea surface temperature retrieval from Landsat 8 OLI/TIRS data at coastal regions. Remote Sensing, 11(22), 2687.

Johnstone, J. A., & Dawson, T. E. (2010). Climatic context and ecological implications of summer fog decline in the coast redwood region. Proceedings of the National Academy of Sciences, 107(10), 4533-4538.

Kuroda, H., & Toya, Y. (2020). High-resolution sea surface temperatures derived from Landsat 8: a study of submesoscale frontal structures on the Pacific shelf off the Hokkaido coast, Japan. *Remote Sensing*, *12*(20), 3326.

Largier, J. L., Magnell, B. A., & Winant, C. D. (1993). Subtidal circulation over the northern California shelf. Journal of Geophysical Research: Oceans, 98(C10), 18147-18179.

Largier, J. L. (2020). Upwelling bays: how coastal upwelling controls circulation, habitat, and productivity in bays. Annual review of marine science, 12, 415-447.

Largier, J. L. (2022). Rip currents and the influence of morphology on wave-driven cross-shore circulation.

Lamb, K. G. (2014). Internal wave breaking and dissipation mechanisms on the continental slope/shelf. *Annual Review of Fluid Mechanics*, *46*(1), 231-254.

Lentz, S. J., & Fewings, M. R. (2012). The wind-and wave-driven inner-shelf circulation. Annual Review of Marine Science, 4, 317-343.

MacMahan, Jamie H., Ed B. Thornton, and Ad JHM Reniers. "Rip current review." *Coastal engineering* 53.2-3 (2006): 191-208.

Minnett, P. J. (2010). The validation of sea surface temperature retrievals from spaceborne infrared radiometers. *Oceanography from Space: Revisited*, 229-247.

Minnett, P. J., Kilpatrick, K. A., Podestá, G. P., Evans, R. H., Szczodrak, M. D., Izaguirre, M. A., ... & Williams, E. (2019). Skin sea surface temperature from VIIRS on Suomi-NPP—NASA continuity retrievals. Remote Sensing, 11(24), 3025.

Montanaro, M., Gerace, A., Lunsford, A., & Reuter, D. (2014). Stray light artifacts in imagery from the Landsat 8 Thermal Infrared Sensor. Remote Sensing, 6(11), 10435-10456.

Muller-Karger, F. E., Hestir, E., Ade, C., Turpie, K., Roberts, D. A., Siegel, D., ... & Zhu, Z. (2018). Satellite sensor requirements for monitoring essential biodiversity variables of coastal ecosystems. Ecological Applications, 28(3), 749-760.

Nickols, K. J., Gaylord, B., & Largier, J. L. (2012). The coastal boundary layer: predictable current structure decreases alongshore transport and alters scales of dispersal. *Marine Ecology Progress Series*, *464*, 17-35.

Pauly, D., & Christensen, V. (1995). Primary Production required to sustain global fisheries. *Nature*, 374(6519), 255-257

Palacios, D. M., Bograd, S. J., Mendelssohn, R., & Schwing, F. B. (2004). Long-term and seasonal trends in stratification in the California Current, 1950–1993. Journal of Geophysical Research: Oceans, 114(C10).

Roughan, M., Mace, A. J., Largier, J. L., Morgan, S. G., Fisher, J. L., & Carter, M. L. (2005). Subsurface recirculation and larval retention in the lee of a small headland: a variation on the upwelling shadow theme. *Journal of Geophysical Research: Oceans*, *110*(C10).

Snyder, J. N., Bell, T. W., Siegel, D. A., Nidzieko, N. J., & Cavanaugh, K. C. (2020). Sea surface temperature imagery elucidates spatiotemporal nutrient patterns for offshore kelp aquaculture siting in the southern california bight. *Frontiers in Marine Science*, *7*, 22.

Thomas, A., Byrne, D., & Weatherbee, R. (2002). Coastal sea surface temperature variability from Landsat infrared data. *Remote Sensing of Environment*, *81*(2-3), 262-272.

Torregrosa, A., O'Brien, T. A., & Faloona, I. C. (2014). Coastal fog, climate change, and the environment. *Eos, Transactions American Geophysical Union*, *95*(50), 473-474.

Twedt, K., Xiong, X., Geng, X., Wilson, T., & Mu, Q. (2023, October). Impact of satellite orbit drift on MODIS Earth scene observations used in calibration of the reflective solar bands. In *Earth Observing Systems XXVIII* (Vol. 12685, pp. 158-167). SPIE.

Vanhellemont, Q. (2020). Automated water surface temperature retrieval from Landsat 8/TIRS. Remote Sensing of Environment, 237, 111518.

Wing, S. R., Botsford, L. W., Largier, J. L., & Morgan, L. E. (1995). Spatial structure of relaxation events and crab settlement in the northern California upwelling system. *Marine Ecology Progress Series*, *128*, 199-211.

Wloczyk, C., Richter, R., Borg, E., & Neubert, W. (2006). Sea and lake surface temperature retrieval from Landsat thermal data in Northern Germany. International Journal of Remote Sensing, 27(12), 2489-2502.

Wolanski, E., & Elliott, M. (2015). Estuarine ecohydrology: an introduction. Elsevier.

CHAPTER 3

Characterizing Wave-Driven Nearshore Transport of Surface Turbidity Across Diverse Coastal Geomorphology using High Resolution Remote Sensing and Environmental Data

Abstract

Rip currents play a critical role in cross-shore mixing, sediment transport, and coastal morphology. However, their dynamics in rocky shore environments remain understudied due to the predominant focus on sandy beaches. While remote sensing offers promise for studying these environments, the fine-scale resolution required to observe rip currents using satellites presents unique challenges due to the heterogeneous nature of nearshore waters. In this study, we utilized data from a deep learning-based, satellite image processing and coastline detection python package, CoastSeg, to resolve nearshore heterogeneity in hundreds of high-resolution Sentinel-2 (10m) images. This enabled the accurate extraction of red water-leaving radiances (Rhow_{665}) as a proxy for turbidity in the nearshore waters off Northern California, spanning from San Francisco Bay to the Gualala River. We contextualized these Rhow_{665} data using coincidental wave model data from CDIP MOP, tide data, and high-resolution (2m) bathymetric data. Analysis included creating pixelwise time series correlation maps and calculating the average cross-shore decay of turbidity at 31 sites with distinct geomorphologies. We specifically examined decay equation coefficients C_0 (initial shoreline turbidity concentration) and b^{-1} (inverse decay rate) across different wave climates and their correlations with site-specific bathymetries. Our findings indicate that smooth bathymetries, typical of sandy beaches, exhibit high C_0 values, reflecting high shoreline sediment erodibility and mobility. However, these areas generally showed limited b^{-1} due to the lack of bathymetric complexity necessary to sustain large rip currents, especially in low wave energy conditions. Conversely, rocky shores with high bathymetric roughness supported stronger b^{-1} values in low wave climates, and particularly so in low water levels, but lacked sufficient C_0 to generate significant turbidity signals under these conditions. Notably, sites with rocky shores near

sediment-rich estuaries, sandy embayments, headlands, and kelp forests exhibited the highest C_0 and b^{-1} values, resulting in the most extensive offshore turbidity transport. In addition to providing novel quantitative insights into wave-driven transport in rocky shore environments, this research contributes a quantitative framework for assessing how geomorphology and wave dynamics influence turbidity transport, offering valuable guidance for coastal management and conservation efforts.

1. Introduction

Rip currents play crucial roles in cross-shore mixing (Smith & Largier, 1995), sediment transport (Aagaard et al., 1997), and coastal geomorphology (Wright & Short, 1984; Castelle & Masselink, 2023). These currents are typically induced by the interaction of hydrodynamic processes with morphological features, such as flow separation on headlands and channelized flow through rocky bathymetry (MacMahan et al., 2006; Castelle et al., 2016; Largier, 2022). The shear stress generated by rip currents mobilizes sediment, altering beach slope, seabed morphology, and nearshore chemical and temperature gradients (Smith & Largier, 1995). Suspended sediments in these flows impact nearshore chemistry, biology, and geomorphology, as well as light attenuation and primary productivity (Lawson et al., 2007).

Rip currents are typically induced by the interaction of hydraulic flow with morphological features, such as flow separation on headlands and sea stacks or channelized flow through gaps in longshore sandbars and rocky bathymetry (MacMahan et al., 2006; Castelle et al., 2016; Largier, 2022; MacMahan et al., 2023). In some cases, rip currents can also result from instabilities in longshore flow (Noyes et al., 2004). The unique characteristics of each shoreline, including wave climate, beach slope, and geomorphology, contribute to the high diversity of rip currents (Largier, 2022). This diversity ranges from dissipative sandy beaches to reflective rocky shores, with headlands of varying shapes and sizes that influence cross-shore sediment transport (George et al., 2015; Castelle et al., 2016; George et al., 2019). Rip current characteristics also vary with factors such as sediment granulometry and availability (Jaffe et al., 1984). Fig 1 illustrates some of this variability, displaying rip currents at three different sites with varying geomorphic facies and sediment availability.

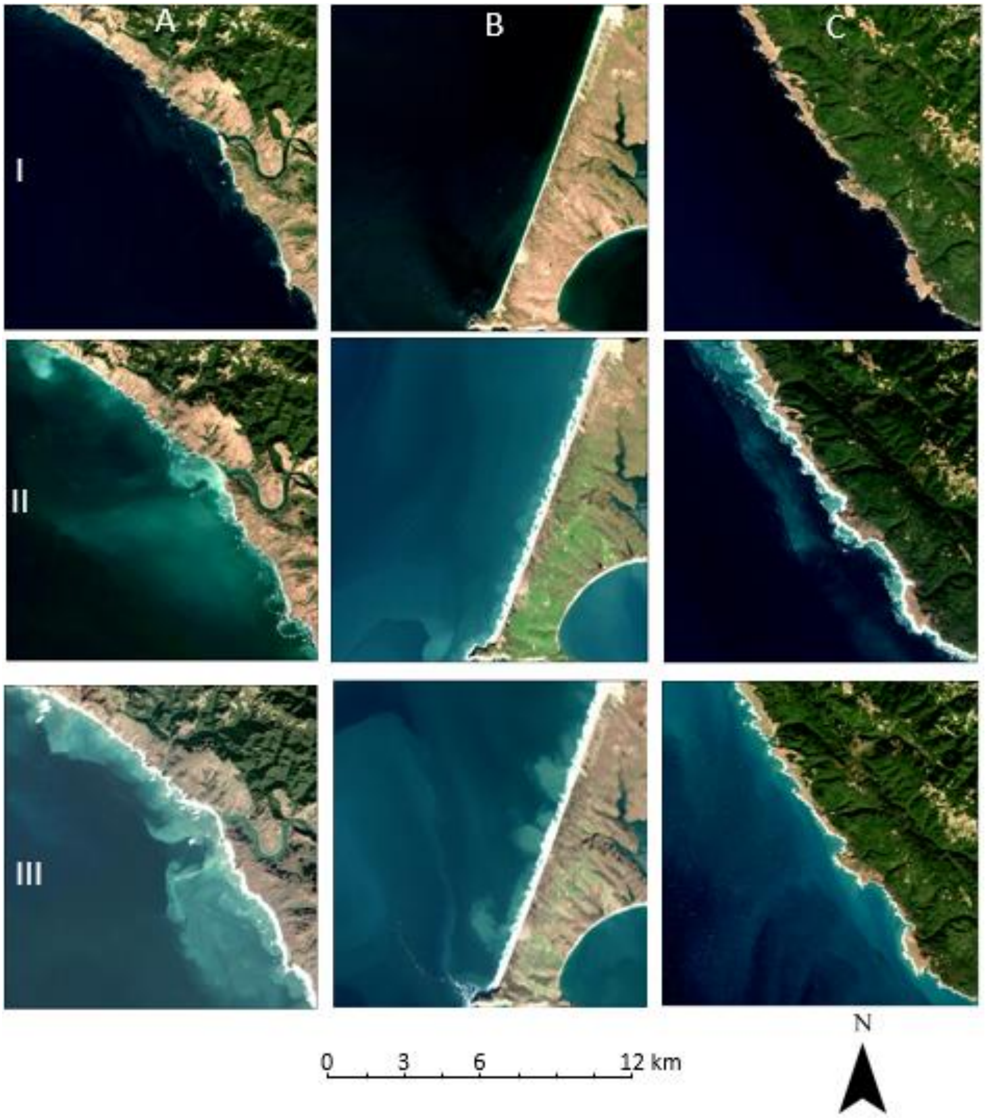

Fig 1: Examples of rip currents from 3 locations in our study site. Column A: Extent overlooking the Russian River between Wrights Beach and Timber Gulch. Column B: Extent overlooking Pt Reyes National Seashore between Pt Reyes and Point Reyes Beach IV. Column C: Extent overlooking Salt Point State Park; Rows I-III, examples with offshore turbid signal from waves within respectively further offshore extent.

Despite their diversity, most rip current studies have focused on recreational beaches with an emphasis on swimmer safety (Brander & Scott, 2016), resulting in a knowledge gap regarding their behavior in rocky shore environments (Largier, 2022). These complex, rocky settings present unique challenges for in-situ monitoring due to hazardous conditions and limited accessibility (Gallop et al., 2018). However, understanding rip current dynamics in these environments is crucial for predicting sediment transport, coastal erosion, and the overall functioning of nearshore ecosystems (Loureiro et al., 2012).

Satellite remote sensing offers a promising methodology for monitoring rip currents, as it overcomes the safety challenges associated with these fast offshore flows, particularly in rocky shore environments. However, limited research has been conducted on quantitatively observing rip currents using satellite remote sensing. Until recently, the surface extent of these features was small relative to the resolution of available satellite data (Holman & Haller, 2013). Moreover, the nearshore environment is highly heterogeneous presenting unique challenges in image processing. These factors present significant challenges for accurately detecting and quantifying rip currents using remote sensing techniques.

This project aims to develop remote sensing methodologies for processing and analyzing imagery to quantitatively observe rip currents using high-resolution Sentinel-2 imagery, coincidental monitoring and modeled data, and local high-resolution bathymetric data. By gathering statistics on wave driven transport in different geomorphological and hydrodynamic contexts, we seek to better understand the controls that constrain sediment mobilization and transport in rip currents, both ubiquitously and dichotomously, examining how controls vary with differing geomorphologies (i.e. rocky and sandy shores, complex vs uniform coastline shape). The use of Sentinel-2 imagery, with its high spatial and temporal resolution, provides an opportunity to study rip currents at a regional scale and in diverse coastal settings. Combining this satellite data with coincidental/local environmental data and statistical analysis enables comprehensive understanding of rip current dynamics and their variability across environments.

2. Methods

2.1 Study Site

Overall Site:

The region of study, located in Northern California just north of San Francisco Bay, lies between 37.5° to 38.5° N and -123.45° to -122.55°W within the Sentinel-2 tile 10SDH. This area geomorphically diverse, making it ideal for maximum variability. The shoreline throughout the region includes various sand-fronted facies such of varying length, width, area, and shoreface angle. Between these areas lie ephemeral sandy berms that appear at low tidal levels, pocket beaches, and seacliff and sea stack-fronted shores. The region also features kelp forests with varying canopy coverage by year (Bell et al., 2015; Bell et al., 2020) The presence of kelp forests can influence nearshore hydrodynamics and sediment transport, as they can attenuate wave energy and alter current patterns (Gaylord et al., 2012).

The region experiences a Mediterranean climate, with intense winter rainfall events (i.e., atmospheric rivers) and relatively dry conditions throughout the rest of the year (Wheatcroft et al., 2010; Dettinger et al., 2011). Winds exhibit seasonal patterns, with strong northerly winds driving coastal upwelling in spring and summer (April to June), southerly wind events during winter storms (December to February), and weaker winds in the fall (August to October) (Garcia-Reyes and Largier, 2012). This seasonal storm pattern also controls the influence of turbidity from buoyant freshwater outflow, primarily from the Russian River (Speiser and Largier, in review) and smaller rivers like the Gualala River, Salmon Creek, and ephemeral rivers and runoff. Outside of storm season, these locations are often closed off from the ocean by sandy berms (Behrens et al., 2013). Littoral cells in the region are largely supplied by these rivers, with over 80% of the sediment coming from major river outflows (Griggs and Hein, 1980; Runyan and Griggs, 2003). Finer sediments can travel tens of kilometers alongshore (Speiser and Largier, in review), while coarser sediments deposit closer to shore and are transported within and between littoral cells via longshore transport (Patsch and Griggs, 2007).

Shoreline morphology in the region is also seasonal, with low-sloped, dissipative beaches and fine-grained sands during the summer, and high-sloped, reflective beaches during the winter, influencing cross-shore flow (Wright and Short, 1984). Sand berm morphology is inherently tied to this process, providing sediments to sandy shores during the summer and being refed by sediments from the shoreline during the winter, impacting rip current dynamics (Masselink and Short, 1993; Castelle et al., 2016). Changing morphology alters wave setup for rip currents (MacMahan et al., 2006). Many of these sandy beaches are also fronted by nearshore sea stacks, which inherently impact wave hydraulics.

Rocky shores, sea stacks, and complex seacliff morphologies in the region create headlands of diverse sizes and complex, stable bathymetries (Largier, 2022). These headlands and sea stacks of different sizes act as boundaries for littoral cells with varying sediment residency times and contribute to the diversity of hydrodynamics, causing flow separation and setup for rip currents (George et al., 2015; George et al., 2019). The complex bathymetry and headland structures can also influence the formation and persistence of rip currents, as well as the exchange of water and sediment between the surf zone and the inner shelf (Castelle et al., 2016).

Individual Sites:

Thirty-one sites of interest were chosen throughout the study region where the Sentinel-2 tile is in full on all dates. These regions were grouped by landmarks and obvious headlands. Regional groups and site descriptions are as follows:

North Fort Ross: This region starts north of Ross Reef (site 4), characterized by rocky shore platforms and small embayments fed by ephemeral runoff. The largest embayment is Timber Cove (site 2), a ~1000m wide cove sheltered by ~400m headlands. Sites: North Fort Ross (1), Timber Cove (2), Central Fort Ross (3), Ross Reef (4).

South Fort Ross: A thin (~25m wide) shoreline with dispersed boulders and short sea stacks breaking the surface at low tide, with gulches, Timber Gulch (site 1) and Jewell Gulch (site 3). Kelp forest is observable through true color imagery and in historical kelp data from the California Department of Fish and Wildlife (CDFW) aerial imagery surveys, particularly in Sites 5 and 6 . Berm discontinues in a series of boulders in the middle of site 3 and ends in a headland in site 4, ~150m upcoast of the sites downcoast extent. Sites: Timber Gulch (5), Timber/Jewell Gulch (6), Jewell Gulch (7), Meyer Gulch (8).

Russian River Area: Notable for the Russian River Estuary (site 12), which is south-bound by Goat Rock. Estuary is fronted by a 2km long sandy beach berm with several sea stacks in the nearshore. North of the estuary, are with several pocket beaches/sandy embayments separated by small headlands and seacliffs with sea stacks. The embayment with the largest berm is within Russian Gulch (Site 10). Sites: (9) North of Russian Gulch , (10) Russian Gulch, (11) Jenner Headlands, (12) Russian River Estuary.

Wrights Beach Area: South of the Russian River Estuary, separated by Goat Rock, north of Site 13. Sites are primarily seasonally sandy embayments separated by headlands, with many sea stacks in the nearshore, and a few seacliff-fronted shores in site 14. The widest beach berm (~250m wide) is in site 16, Wrights Beach, which ends southward at a small headland. Sites: (13) <u>South of Russian/Goat Rock</u>, (14) <u>Shell Beach</u>, (15) <u>North Wrights Beach</u>, (16) <u>Wrights Beach</u>

Salmon Creek Beach Area: Includes sites distributed around the Salmon Creek Estuary, with Portuguese Beach (site 17) to the north. Sites 19 and 20 have a shared berm backed by dunes and have no sea stacks in the nearshore. Site 18, is where the berm ends north of the estuary, and is seacliff backed with sea stacks. Portuguese beach is separated by seacliff and has sea stacks. Sites 19 and 20 face northwest. <u>Sites</u>: Portuguese Beach (17), North Salmon Creek Beach (18), Central Salmon Creek Beach (19), South Salmon Creek Beach (20).

Bodega Marine Lab: Located on west-facing seacliffs on the Bodega Bay headland, oriented nearly 90° from Salmon Creek Beach, fronted by platforms. Notable is "Horseshoe Cove" a 150m wide, 300m deep with sandy shore in site 21 and small sandy embayments in the southern portion of in site 22, which shares a headland with the Bodega Bay inlet. <u>Sites</u>: (21) Bodega Marine Lab, (22) Bodega Head.

Bodega Bay: Situated between Bodega Bay and Tomales Bay and influenced by tidal outflows, which are occasionally turbid. Estero Americano (site 23) is fronted by a berm, with another berm southward separated by seacliffs. Site 24 is 1.5km north of estero San Antonio. Both sites have nearshore sea stacks and boulders. <u>Sites</u>: Estero Americano (23), Estero Americano/San Antonio (24).

Tomales Point: These sites are on the seaward extent of the Tomales Bay spit and include bluffs, cliff-backed with tidal beaches, and some sheltered persistent pocket beaches and platform beaches. Nearshore sea stacks are in each site. 500m south of site 27 is a 2km nearly continuous berm), McClures Beach, that faces northwest. Sites: (25) Tomales point (26) Elk Reserve (27) North of McClures Beach

Point Reyes National Seashore: Stretching along a 19km long, 100m wide berm with no sea stacks, these sites transition from berms backed by dunes to cliffs. The farthest north site (site 29) is in front of Abbott's lagoon, a permanently closed lagoon, with the widest berm. ~4km downcoast of site 31, the berm ends at the Pt Reyes headland. Sites: Pt Reyes Beach I (28), Pt Reyes Beach II (29), Pt Reyes Beach III (30), Pt Reyes Beach IV (31).

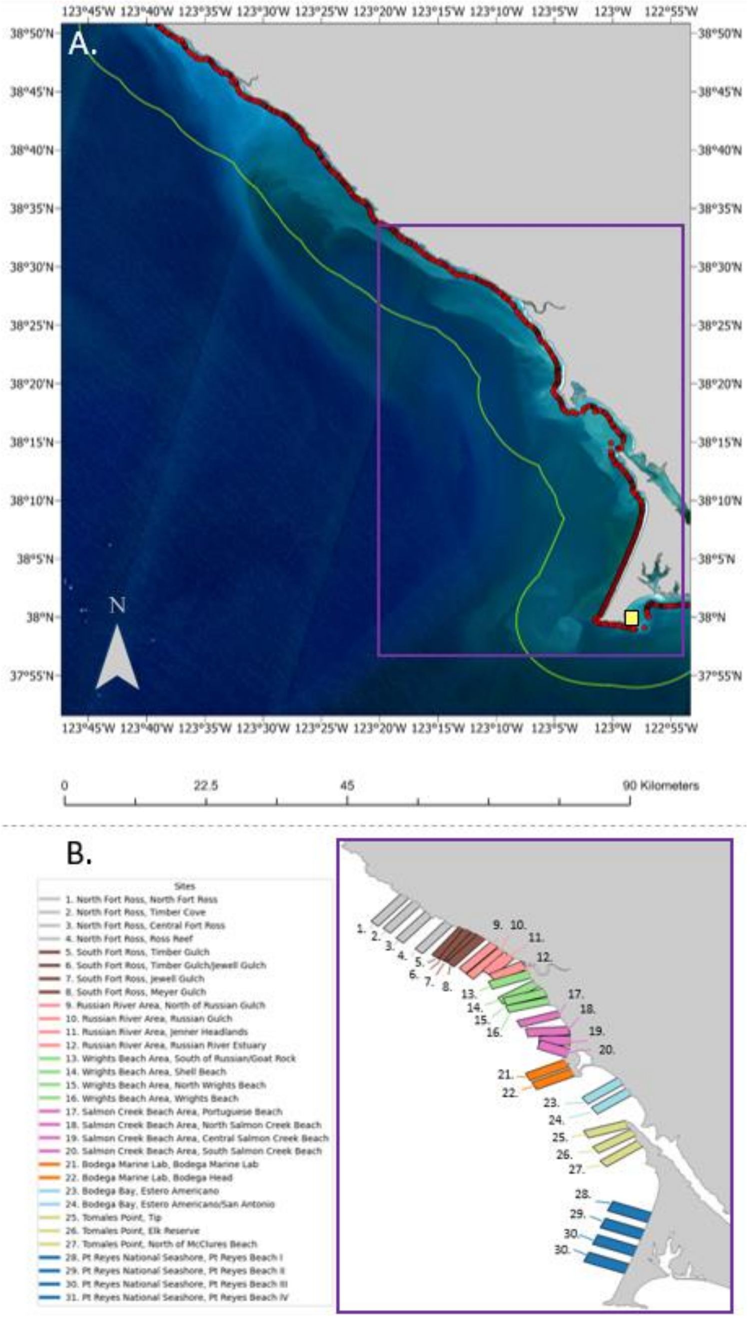

Fig 2: Maps of Study Region: A.) Entire region of study. Green line is extent of data considered, 10km offshore. Red dots are CDIP MOP wave energy modeling points at 10m isobath. Yellow square is NOAA Tide Gauge #9415020. Purple square is extent of map: B) Map of study sites as outlined in Methods 2.2. Site rectangles are colored by same regional group.

2.2 Environmental Data

In this study, we statistically contextualize reflectance from high-resolution satellite imagery with coincidental local monitoring, modeling data, and bathymetric data. Hourly wave height (H_s), direction (D_a), and Period (T_a) data were gathered from the Coastal Data Information Program (CDIP; https://cdip.ucsd.edu/), generated using a linear, spectral refraction wave model driven by offshore wave buoy observations (O'Reilly et al., 2016). This wave data is measured at the 10m isobath and estimated every 100m alongshore (Fig 2), providing a detailed spatial representation of wave conditions in the nearshore zone (Adams et al., 2011; Orzech et al., 2010; Vos et al., 2019).

Ocean water level data referenced to MLLW were obtained from the Point Reyes tide gauge (NOAA #9415020) (Fig 2). Data from this gauge is known to represent tides at the Russian River mouth with negligible phase and amplitude differences (J.L. Largier and D.S. Behrens unpublished data). For regions closer to Fort Ross than Pt Reyes, water level was offset by .96 feet, low tide by -30 minutes, and high tide by -51 minutes, as recommended by NOAA. This data is captured in 15-minute bins, providing a high temporal resolution for analyzing tidal influences on nearshore processes (Largier et al., 1993).

Bathymetric data, acquired by the Seafloor Mapping Lab of California State University Monterey Bay in 2010 using multibeam sonar and backscatter imagery, are provided at a 2m resolution. This high-resolution bathymetric data allows for detailed analyses of seafloor morphology and its influence on nearshore hydrodynamics.

Kelp forest canopy data from the California Department of Fish and Wildlife (CDFW) aerial imagery surveys (2010, 2013-2016) were also explored for discussion of the role of kelps in sediment supply and transport. This dataset was chosen due to its high-resolution capture, which enables the observation of kelp forests coverage in close nearshore. However, it should be noted that this dataset ends at 2016 and has an incomplete extent in the years not used.

2.3 Satellite Data

Unprocessed Sentinel-2 (S2) Level 1C satellite data were accessed through the SentinelHub API (https://www.sentinel-hub.com) to capture small-scale signatures of rip currents. The S2 constellation collects imagery in 13 spectral bands at 10, 20, and 60m resolutions, with a combined revisit time of 5 days (Drusch et al., 2012; European Space Agency, 2015). Data from 06/2015 to 05/2023 were collected for the study area, from S2 tile 10SDH, accounting for 758 total images. S2 are sun synchronous and overpass areas at 10:30AM local solar time, so coincidental temporal data (CDIP MOP and NOAA Tide data) was captured within the 9:00AM to 10:00AM local solar time and averaged as an hourly bin. Tile 10SDH is in the edge of Sentinel-2 swath, so occasionally data from the site is incomplete, accounting for missing data in half the extent as seen with missing pixels in Fig 4, (European Space Agency, 2015).

ACOLITE (https://odnature.naturalsciences.be/remsem/software-and-data/acolite) was used for atmospheric correction to water leaving reflectance and initial masking of image artifacts such as clouds, glints, sea stacks, boulders, boats, and shadows from topography and clouds. ACOLITE atmospherically corrects to water leaving radiances in two steps, first using Rayleigh correction to correct for scattering, then using short wave infrared radiation data to correct for aerosols over water (Vanhellemont & Ruddick, 2015; Vanhellemont, 2019).

Red (665 nm) and near-infrared (NIR, 842 nm) wavelengths from Sentinel-2 (S2) satellites are well-established proxies for sediment turbidity in water quality monitoring (Lahet & Stramski, 2010; Saldías et al., 2016). These wavelengths are sensitive to suspended sediments due to strong scattering by particles and low absorption by water molecules (Nechad et al., 2010). To validate their use in our study region, we compared atmospherically corrected water-leaving radiance (Lw) in NIR (Rhow842) and red (Rhow665) bands with coincidental turbidity measurements from the Hacienda Bridge gauge (USGS #11467000) in the Russian River, using the average of all values between the river mouth and the gauge (Fig 3). Rhow665 showed a logarithmic correlation (Spearman's rho=0.88) with turbidity, consistent with the saturation effect at high sediment concentrations observed in previous studies (Nechad et al., 2010; Dogliotti et al., 2015). Rhow842 exhibited a linear correlation (Pearson's r=0.87). Given its stronger correlation and sensitivity at high radiances, Rhow665 was used as a proxy for suspended sediment concentration.

Discharge data from the Hacienda Bridge gauge were used to filter out dates when coastal turbidity might be influenced by freshwater outflow, following the methodology of Speiser and Largier (in review). This approach isolated dates when wave momentum was sufficient to trap turbid outflow within the surf zone, preventing its transport to the coastal shelf. 299 out of 403 non-cloudy image dates surpassing this threshold were used in the analysis (Fig 4).

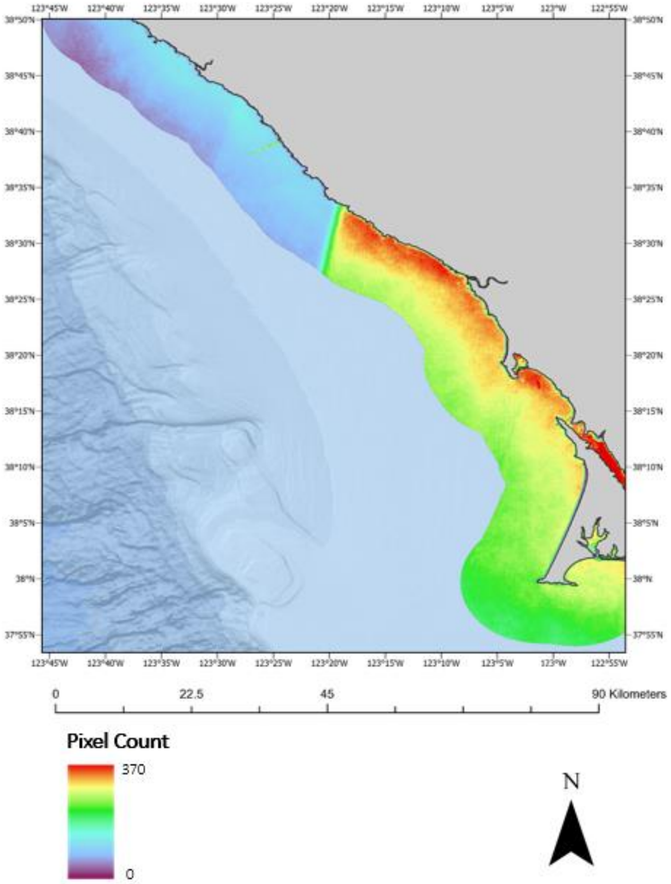

Fig 4: Count of available pixels at each position, surpassing river momentum dominance threshold, after cloud clipping and whitewater removal.

Foam from breaking waves, wave caps (Gordon & Wang, 1994), and foam lines (Killeen et al., 2023), while sometimes incidentally masked in atmospheric correction (likely due to cloud masking), vary in position and presence geographically from image to image due to changing tides and wave climatology. These white features have very high albedo and can significantly skew statistical metrics if included in a dataset in which reflectance is being observed as a proxy for suspended sediment (Shi & Wang, 2009). To mask out these features, we developed a methodology using the package CoastSeg (Buscombe, 2023; Fitzpatrick et al., 2024), which includes segmentation models with a class representing "whitewater" within images. The workflow consisted of the following steps: 1) running the model on each true color satellite image, 2) removing land using a static land mask, 3) applying a 5-pixel radius disk kernel to each pixel classified as white water (falling within the softmax threshold) to find probable white water pixels, 4) applying gap filling, 5) applying a morphological closing operation using another 5-pixel radius disk kernel, 6) manually inspecting the results to confirm the effectiveness of the methodology in isolating shore-parallel foam from breaking waves, and 7) extracting all Rhow$_{842}$ pixels from each atmospherically corrected NIR image and determining the median value of those pixels to be the maximum pixel value for non-foam radiance (Rhow833= .0111 L_W). For any image, any zone where Rhow833 > .0111L_W is masked. Manual inspection of images confirmed the effectiveness of this methodology, and a total of 17,675,010 pixels were removed from the already masked Acolite images. Because land features are more reflective than foam features in NIR, any remnant artefacts, such as sea stacks, not captured from the 20m feature masking from ACOLITE were also removed from the dataset (Fig 5).

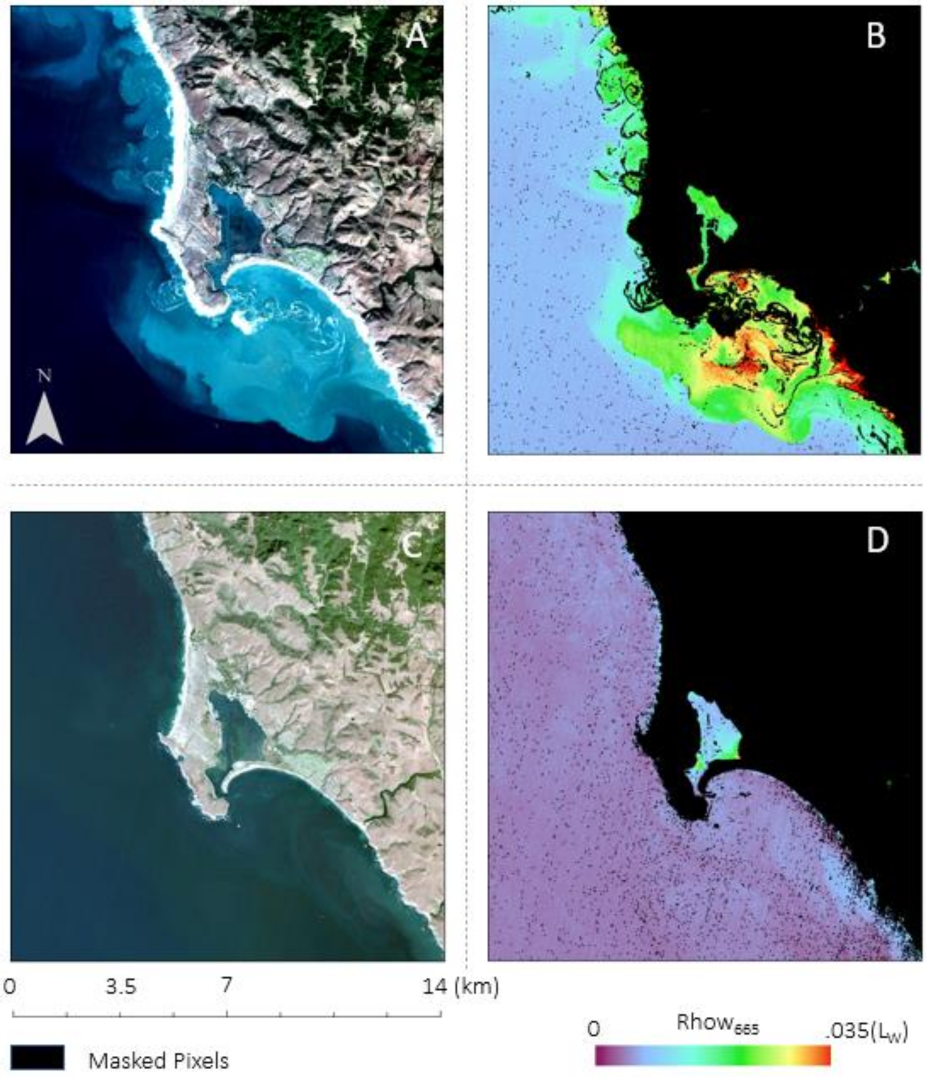

Fig 5: True color Images from dataset overlooking Bodega Bay (A: 12/08/2020, C: 09/24/2020) and their respective Rhow_{665} data after pixel masking for land and white water (B:12/08/2020, D: 09/24/2020). (A &B) are from a date with higher wave energy with a lot of white water and (C & D) are a low energy date. Black data in Rhow_{665} are masked pixels.

To differentiate between water made turbid by sediments from wave resuspension and "clear" water, we examined the distribution of pixel values from all cloudless images (manually inspected) within a $5\mathrm{km}^2$ region offshore, outside the visible influence of turbidity from breaking waves (Fig 6). The 97th percentile Rhow_{665} value, .0088 L_W, of these pixels was considered the maximum value for non-turbid water ($C_{\mathrm{threshold}}$), with the logic that higher values must be under the influence of a turbid transport process. This threshold is consistent with similar approaches used in previous studies to differentiate between turbid and clear water (e.g., Saldías et al., 2012; Mendes et al., 2014; Saldías et al., 2016). While this threshold may not perfectly capture all instances of turbid water, it provides a reasonable and conservative estimate for the purposes of this study.

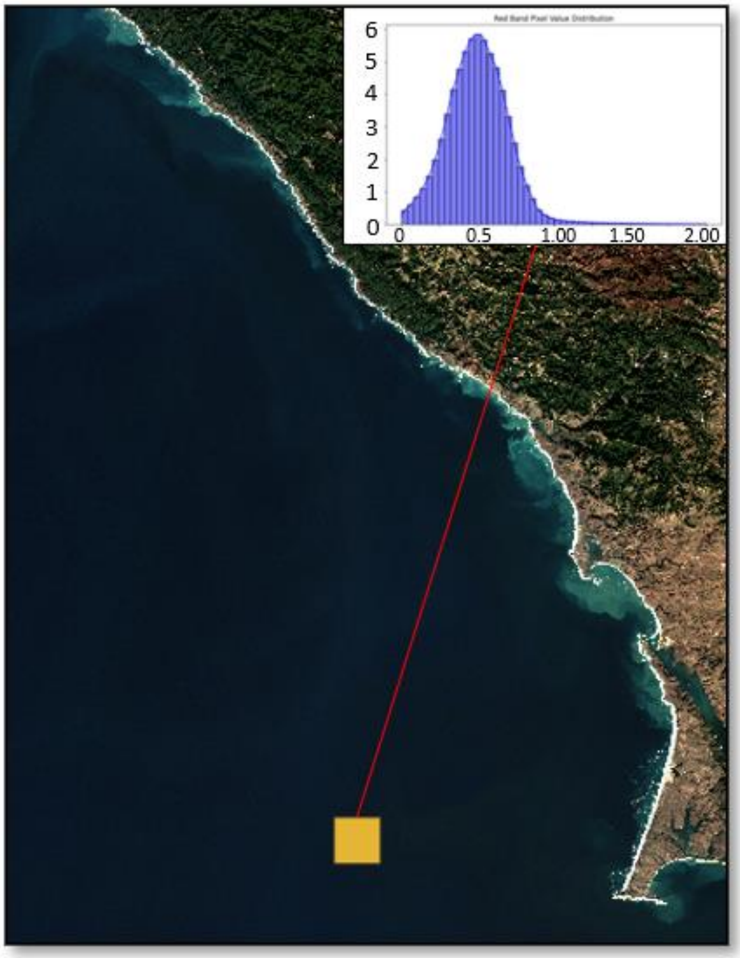

Fig 6: Bounding box (yellow) for extent of pixels extracted to calculate clear water threshold and histogram of pixel values (y-axis is pixel count (1e6) and x axis is Rhow_{665} value (L_W)). Background image is Sentinel-2 image from the study site from 12/08/2020.

2.4 Statistical Analyses

Maps of reflectance statistics at pixel positions were created to observe trends in nearshore turbidity and their correlation with environmental controls. To compare pixels with coincidentally measured wave variables, we found the closest CDIP MOP wave modeling point for each pixel position within images using the haversine equation for distance on a sphere (Sinnott, 1984). Reflectance values at each pixel were then matched with model variables for coincidental times, allowing for direct comparison between satellite-derived turbidity and wave conditions.

We generated maps showing the count and median of Rhow665 values at each location to assess average turbidity distribution and variance. To examine changes in turbidity under varying wave energy, we recalculated median Rhow_{665} statistics for satellite images subset by Hs data at the nearest buoy, using different wave energy percentiles (below 50th, above 50th, 75th, and 95th). This approach provided insights into the role of wave forcing on sediment resuspension and transport. Contours were drawn with a base at $C_{\text{threshold}}$ to mark the offshore extent of wave-impacted turbidity. Contours with surface areas below 1.6km^2 were excluded from the dataset. This approach assumes that pixels beyond the threshold were outside the influence of rip currents.

We adapted the methodology of Speiser and Largier (in review) to estimate wave and tidal control on turbidity at each pixel. Maps of correlation at each pixel between Rhow_{665} and and wave parameters (H_s, D_a, T_a) modeled at coincidental times at the nearest buoy location were created using Spearman's rho rank correlation (ρ) to account for non-linear relationships and outliers arising from incidental processes (Mukaka, 2012; Schober et al., 2018; Speiser and Largier, in review). These correlations were mapped at the resolution of pixel data (10m), and contours were created to describe the regional influence of waves and tides on turbidity, following Speiser and Largier (in review). Correlation strength classes are shown are consistent with Speiser and Largier, shown in Table 1. Contours smaller than 1.6km^2 in extent were removed from the dataset. The value ranges for these classes are determined to the second decimal (i.e., 0.394 falls in the "weak correlation class", while 0.395 is rounded to 0.40 and falls in the "moderate correlation" class).

Absolute value of Rho	*Interpretation*
0.00-0.10	Negligible Correlation
0.10-0.39	Weak Correlation
0.40-0.69	Moderate Correlation
0.70-0.89	Strong Correlation
0.90-1.00	Very Strong Correlation

Table 1: Correlation strength classes from Schober et al., 2018. Table is from Speiser and Largier, in review.

To model rip current activity at 31 sites (Fig 1), pixels were binned by cross-shore shore-normal angle transects (3km cross shore by 1km alongshore rectangles). Location of backbeach and shore-normal angle were determined from CDIP data points. For each image capture date, median Rhow_{665} values every 10m along the midline of the shore-normal transect were plotted against distance offshore (d), and the best fit was calculated using an exponential decay equation:

$$C_{(x)} = C_0 \cdot e^{(-b\,x)} \qquad \text{eq 1.}$$

where in this case, $C_{(x)}$ is $Rhow_{665}$ at offshore distance x, C_0 is the initial value at x = 0km, and *b* is the decay coefficient. This exponential decay equation is regularly used to describe distance and and other water quality measures throughout a variety of hydrologic contexts. Examples of $Rhow_{665}$ images with respective best turbidity concentration decay equations are shown in Fig 6. Only equations with high-quality fits with $R^2 \geq .9$ were included (3710 out of 5369 total equations) ensuring robust data, but it is acknowledged that this may also exclude some legitimate data points. Decay constants C_0 and *b* were averaged across all dates and in dates grouped by quartiles of wave and tidal conditions and were compared between sites. Quartile ranges calculated as global values across all sites so that wave and tidal feature subset bounds are consistent for each site. Wave variables were gathered from the modeling points closest to the site's midline. The equation $C_0.e^{-b.d} = C_{threshold}$ was used to estimate the estimate offshore extent of wave-driven turbidity (d).

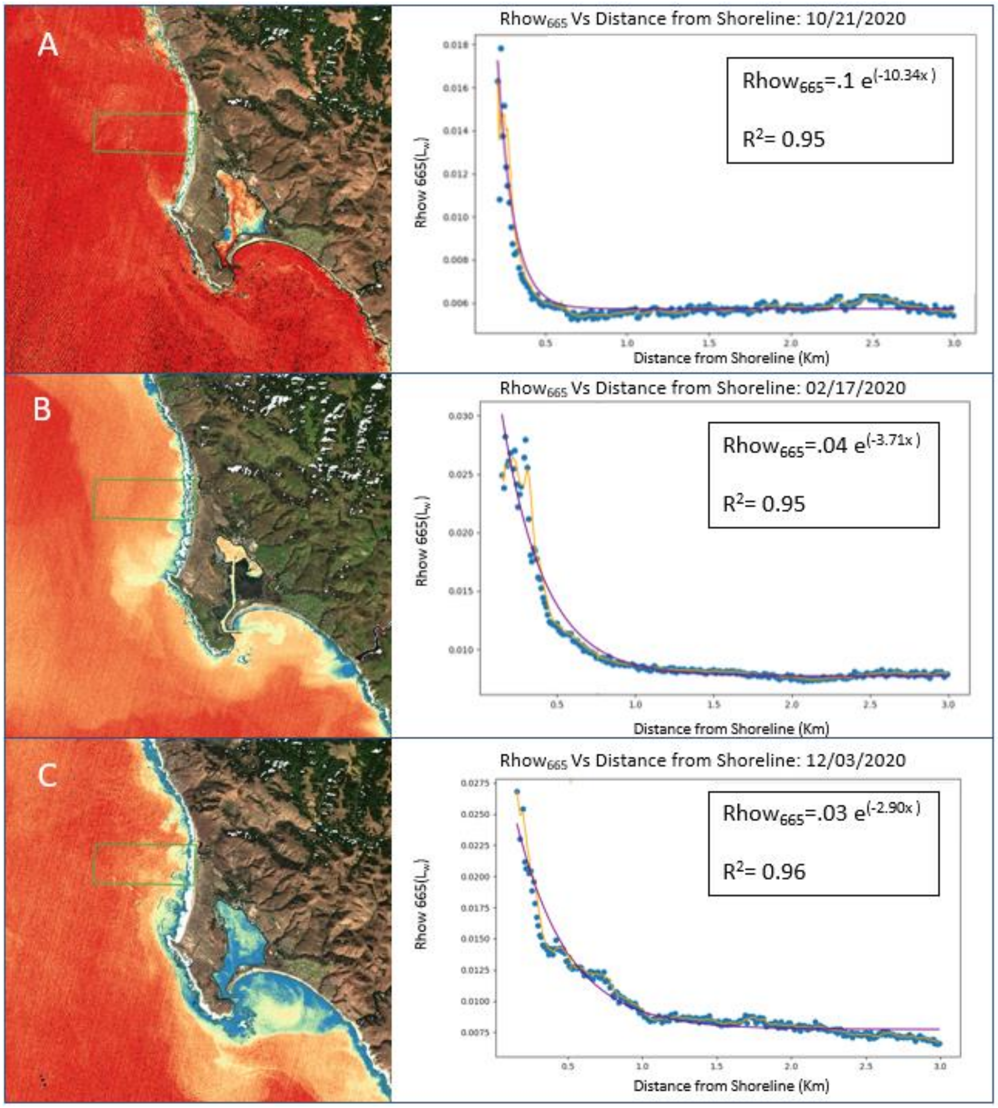

Fig 7: Rhow$_{665}$ data a small extent of Bodega Bay and the site bounds for the Central Salmon Creek Beach site, site 19 (green rectangle) on three separate dates (A: October 21, 2020; B: February 17,2020; C: December 3, 2020). Plot points are respective average Rhow665 (y axis) versus distance offshore along the site extent midline (x axis), binned every 10m. In each plot is the equation of the best fit decay line (in purple) as well as goodness of fit (R^2).

Bathymetry data were binned using the same methodology to characterize each site's bathymetry. Depth was averaged every 2m along the midline, and roughness (standard deviation) was calculated alongshore and cross-shore as an approximation of rugosity. When applicable, data were detrended using SciPy (Virtanen et al., 2020). Metrics were averaged in distance bins from the shoreline (0.5km 1.0km, 1.5km, 2.0km, 2.5km, and 3.0km) to capture bathymetric changes with distance: a.) alongshore roughness (ε_a), calculated as the standard deviation of depth values parallel to the shoreline within each distance range b.) cross-shore roughness (ε_c), computed as the standard deviation of depth values perpendicular to the shoreline within each distance range, c.) detrended alongshore roughness (ε_{da}), derived by removing the linear trend from the depth profile parallel to the shoreline and calculating the standard deviation of the residuals d.) detrended cross-shore roughness (ε_{dc}), obtained by detrending the depth profile perpendicular to the shoreline and computing the standard deviation of the residuals, e.) mean depth ($\bar{h}$), the average depth within each distance range f.) depth change (Δh), calculated as the difference between the maximum and minimum depths within each distance range, g.). All depths and metrics relating to depth are absolute values.

These bathymetric variables were compared with the sites' average decay coefficients (C_0, b) and turbidity extent (d), as well as averages from wave and tidal parameter subsets, particularly examining Q1 and Q4 extremes. Distance bins at 1.0km received extra scrutiny to evaluate nearshore bathymetric control on wave energetics. Spearman rank correlation was used to compare metrics, and the results were visualized using heatmaps to identify patterns between bathymetric characteristics (sandy vs. rocky) and turbidity decay in different hydrodynamic conditions.

3. Results

3.1 Region-wide Analyses

This section reviews the spatial patterns of turbidity across the study region and examines their relationship with model wave variables. For geographic site names and boundaries, refer to Fig 2.

Fig 7 shows the median of $rhow_{665}$ values across the observed dataset, along with the turbid contour where pixels surpass the $C_{threshold}$. In the Pt Reyes National Seashore region (Fig 7A), the turbid contour parallels the coastline but varies in cross-shore extent, reaching up to 0.4km offshore north of the southward Pt Reyes Headland and decreasing to 0.15km seaward nearly 11km upcoast. The contour abruptly ends at the south face of Pt Reyes. At Tomales Point, the contour is less consistent and fragmented, extending between 0.1-0.4 km seaward. Fig 7B shows the contour extending further offshore, especially near Bodega Bay esteros (0.73 km), Mussel Point (0.8 km), the Jenner Estuary (2.7 km), and in front of Timber and Jewell Gulch in the South of Fort Ross region. The contour is interrupted at Bodega Head, south of Wrights Beach, and at the midpoint between Fort Ross and the Russian River estuary, as well as just north of Timber Gulch. Further north (Fig 7C), median turbidity surpasses $C_{threshold}$ only in small, headland-protected coves, with the largest contour extending 0.3 km offshore in north-facing coves. The most prominent feature in Fig C is a 2 km-long contour extending 0.8 km offshore from the Gualala Estuary, with a consistent parallel contour extending 0.5 km offshore along the remaining coastline, becoming fragmented at a headland.

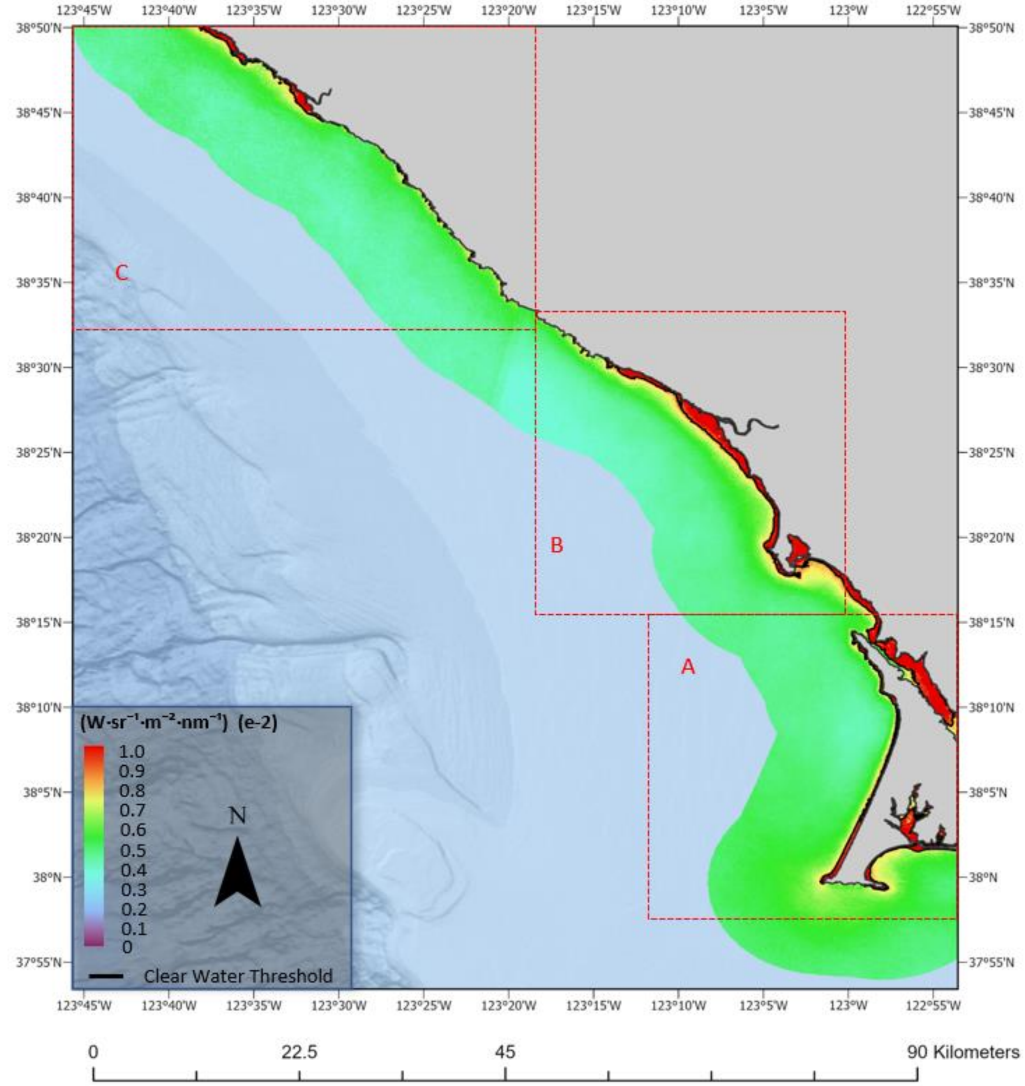

<u>Fig 7.:</u> Median of examined Rhow$_{665}$ values at each pixel location over the region of study. Contour's base is at the established clear water threshold value. Red squares on overall map correspond with zoomed in maps with respective letterings. Zoomed in maps are of the same extent.

Fig 8 compares the median turbid contour with the median turbid contours of all pixels when subset to dates below and above the 50th percentile of H_s at the nearest buoy locations. In the southern region (Fig 8A), the below-average H_s contour extends furthest offshore within bays and south of Drake's Estero, forming a narrow band of 0.05 km alongshore in front of Point Reyes Seashore and small pockets along Tomales Point. In above-average wave conditions, the turbid contour becomes more extensive throughout Fig8A, forming a shore-parallel feature extending 0.5 km offshore, uniform across the Pt Reyes Seashore except for the south-facing Pt Reyes.

In the central region (Fig 8B), the below-average H_s contour extends up to 0.8 km offshore in front of the Russian River estuary, bounded by its northern and southern headlands. Other notable below-average H_s contours lie within between the esteros in Bodega Bay, .1km offshore around Salmon Creek and Wrights Beach (and bound by their headlands), and a 3.5 km-long band south of Fort Ross, reaching 0.4 km offshore at Timber Gulch. The above-average Hs contour extends throughout the region up to the northern Fort Ross area, with maximum offshore distances of 2.1 km south of Doran Beach, 2.2 km at Jenner Headlands, and 1.6 km between Timber and Jewell Gulch. The difference in offshore extent between median and above-average conditions is generally uniform, ranging from 0.5 to 0.8 km, with a maximum of 1.5 km south of Doran Beach.

In the northern region (Fig 8C), the largest below-average Hs contour lies in front of the Gualala Estuary and a cove immediately southward, extending 0.3 km offshore, with smaller contour features appearing in northwest-facing coves 7km upcoast of the estuary. The above-average Hs contour is continuous until 3.5 km south of the Gualala Estuary, where separate features occupy embayment. The above-average contour nearly parallels the median condition turbidity contour, mostly ranging between 0.5-0.8km in further offshore.

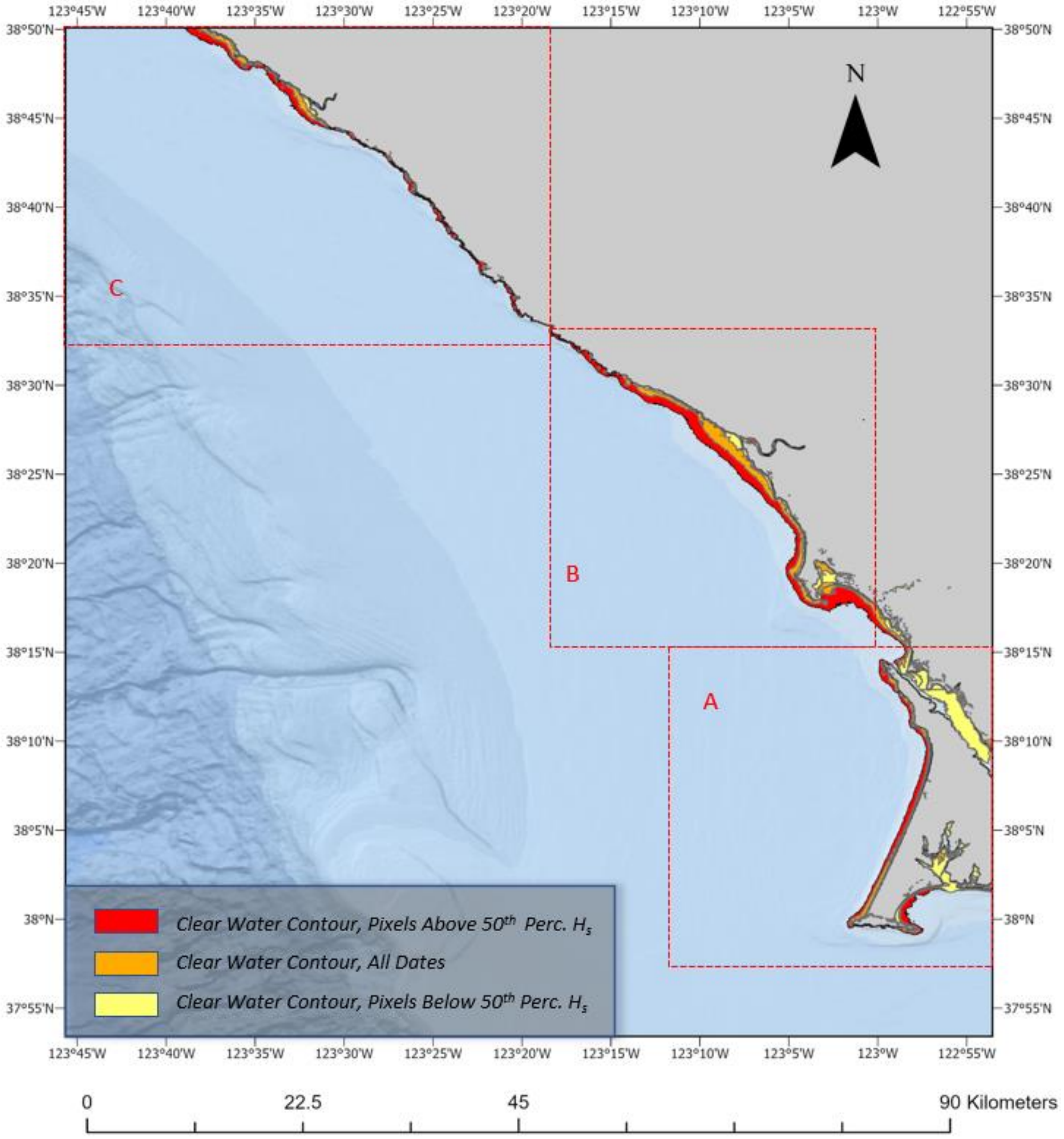

Fig 8: Map showing the position of the contour with its base at the established clear water threshold value mapped when pixels are in their median condition or the median condition to when they are subset between by date where the nearest modeled wave height is above or below its 50th percentile. Red squares on overall map correspond with zoomed in maps with respective letterings. Zoomed in maps are of the same extent

Fig 9 illustrates the per-pixel correlation between rhow665 and coincident Hs at the nearest wave energy modeling location. A continuous weak correlation contour spans the entire study region, generally following the coastline and ranging from 5.0 to 8.0 km offshore. Similarly, A mostly continuous moderate strength contour is present in the nearshore throughout the entire study region. In Fig 9A, this moderate contour starts at Pt Reyes Headland, forming a uniform 0.6 km wide band across the Point Reyes National Seashore, and unevenly extending ~1 km offshore along Tomales Point. In Fig 9B, the moderate contour nearly spans the entire site, terminating north of Fort Ross, with maximum seaward extents off Doran Beach (2.9km), the Russian River Estuary (2.6km), and Timber Gulch (1.8km). Fig 9C shows a moderate contour extending 21.7 km northward from the start of the extent, reaching 0.7 km offshore. A second contour forms 7.5km south of the Gualala Estuary and extends through the rest of the study region, reaching ~1.5km offshore in most areas north of the estuary.

Dispersed "strong" correlation contours are also present. In Fig 9A, few small 0.1km diameter contours are scattered across Tomales Point, with none in front of the Point Reyes National Seashore. In Fig 10B, these contours are clustered between the Bodega Bay esteros, in front of Bodega Marine Lab, in rocky regions between Salmon Creek Beach and the Russian River Estuary, 0.8 km offshore of the Russian River Estuary, in rocky headlands north of the river, 0.1 km offshore of Timber Gulch, and in front of Ross Reef and Timber Cove. South of the Gualala River Estuary, these features are primarily found in small coves, with the largest in the cove directly south of the estuary. Starting 5 km north of the Gualala Estuary, relatively larger strong correlation features are closely distributed, extending throughout the rest of the study region, and reaching ~0.25 km offshore.

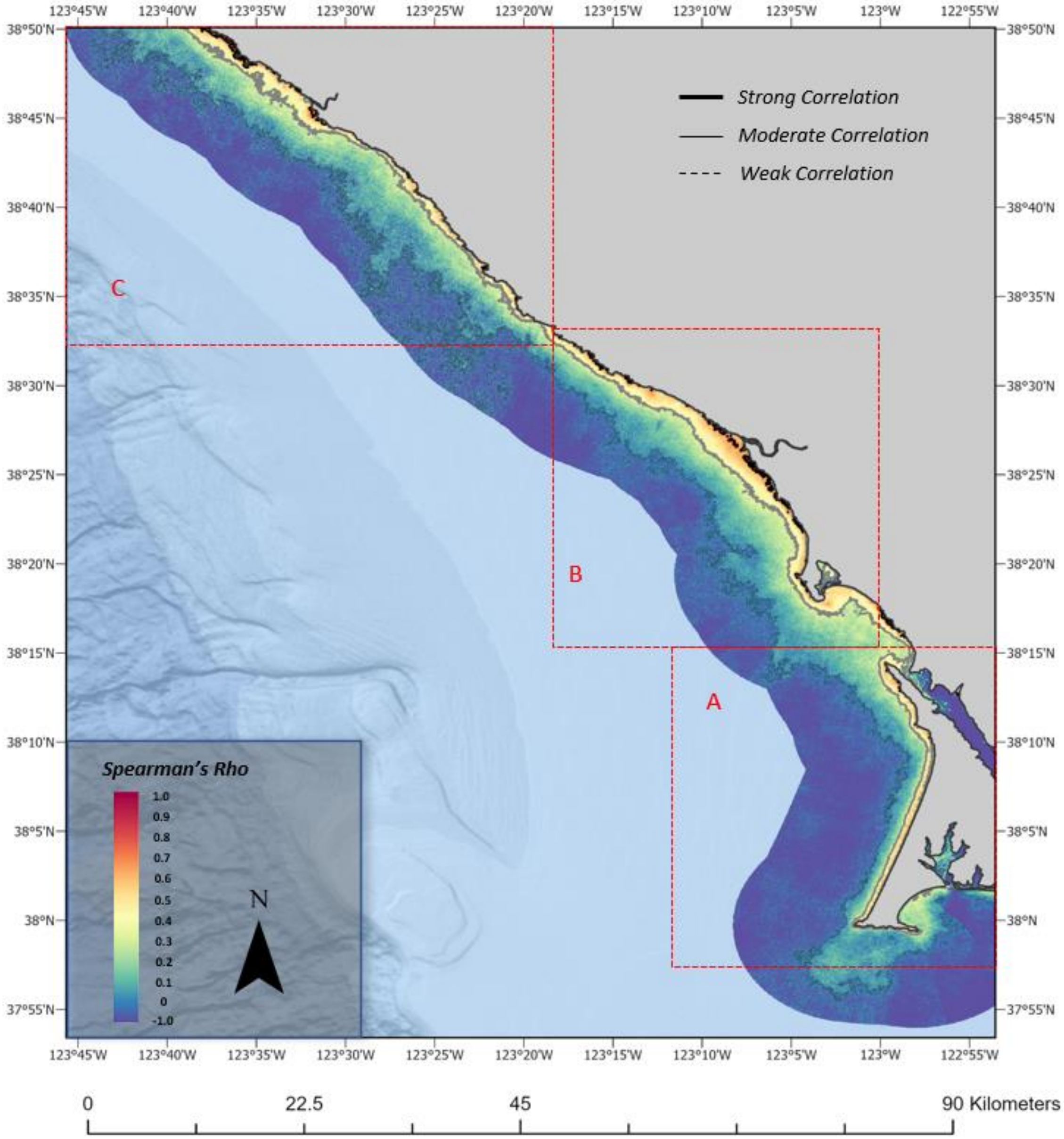

Fig 9: Pixel-wise correlation coefficients between Rhow$_{665}$ and coincident hourly Hs modeled at the nearest wave energy modeling buoy location. Contours are based at correlation strength class range minimums, described in Table 1.

The relationship between Rhow$_{665}$ and wave angle D_a, as well as H_s and T_a normalized to wave angle D_a, were also mapped at each site. However, these results are not reported due to the complexity of the analysis. The relationship between wave angle and seasonal southward currents associated with the largest waves made the isolation of Da as a standalone wave component difficult. Further, the intricate coastline of rocky coastal regions, made it challenging to accurately measure shore angle on a pixel-by-pixel basis, particularly for offshore positions. We also investigated the standard deviation of $Rhow_{665}$ values at each pixel location. The mapped results nearly mirrored those of the median results (high variation at all locations with high median, vice versa) and were not found to add or detract from findings in the study. These results can be found in Appendix I. Similarly, the relationship between $Rhow_{665}$ and coincident wave period, T_a, were also mapped but did not produce any findings that added or detracted from the findings of this study. In these maps, correlations were highest in small regions immediately offshore of estuaries, and lowest in regions that did not correspond to wave models (such as waters within Tomales Bay). These results can be found in Appendix II.

3.2 Sitewise Analyses

When turbidity at different site bins was fit to average best fit equation decay equations as a function of distance in 10m across-shore bins, the C_0 and b coefficients of those equations varied at each site, as seen in the table and plots in Fig 10. South Fort Ross, Jewell Gulch had the highest average C_0 (0.093 Lw), while North Fort Ross, Timber Cove had the lowest average C_0 (0.0126 Lw). Ross Reef had the highest average b^{-1} (.903), and Salmon North Salmon Creek Beach had the lowest average decay b^{-1} (0.158). Decay coefficients within different regional site groups varied within groupings. For instance, sites in the Fort Ross group varied widely across average decay b but not with average C_0, sites along the Pt Reyes National Seashore varied in average C_0 increasing with northward position, and regions like the Russian River Area and South Fort Ross varied widely in both. Other regional groups such as Wright Beach and Tomales Point had smaller distributions of decay coefficients.

When solving for offshore distance of $C_{threshold}$, d (Fig 10C), Timber Gulch, South Fort Ross (d=1.635km), and Russian River Estuary (d=1.520 km) had the highest offshore distances. North Salmon Creek Beach (d=.379 km), Reyes Beach IV, and North Fort Ross (d=0.450km) had the lowest average offshore distances of turbidity. South Fort Ross had the highest variability in average distance of offshore sediment transport among the regional groupings, with Δd_{max} - Δd_{min} = 0.958km. Tomales Point and Pt Reyes National Seashore, the two southward regions, had low inner-site variability, with Δd_{max} - Δd_{min} = 0.109km and 0.117km, respectively.

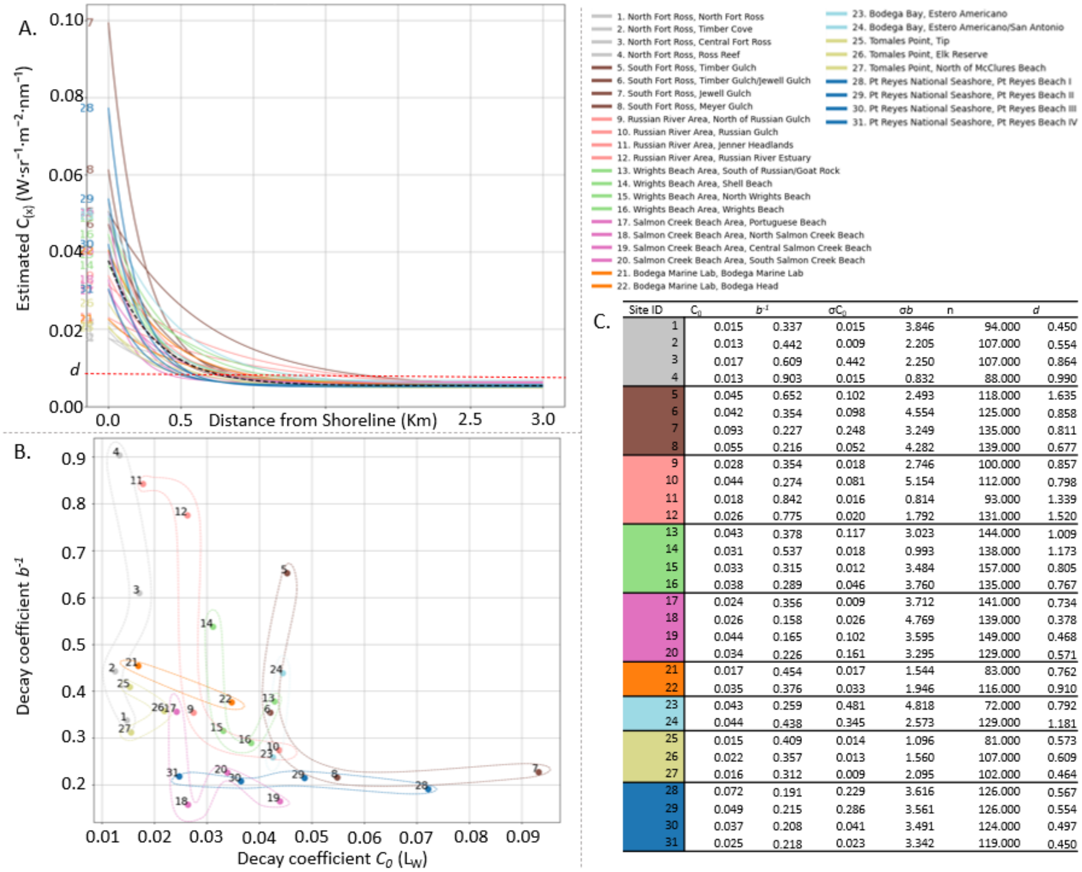

Site ID	C_0	b^{-1}	σC_0	σb	n	d
1	0.015	0.337	0.015	3.846	94.000	0.450
2	0.013	0.442	0.009	2.205	107.000	0.554
3	0.017	0.609	0.442	2.250	107.000	0.864
4	0.013	0.903	0.015	0.832	88.000	0.990
5	0.045	0.652	0.102	2.493	118.000	1.635
6	0.042	0.354	0.098	4.554	125.000	0.858
7	0.093	0.227	0.248	3.249	135.000	0.811
8	0.055	0.216	0.052	4.282	139.000	0.677
9	0.028	0.354	0.018	2.746	100.000	0.857
10	0.044	0.274	0.081	5.154	112.000	0.798
11	0.018	0.842	0.016	0.814	93.000	1.339
12	0.026	0.775	0.020	1.792	131.000	1.520
13	0.043	0.378	0.117	3.023	144.000	1.009
14	0.031	0.537	0.018	0.993	138.000	1.173
15	0.033	0.315	0.012	3.484	157.000	0.805
16	0.038	0.289	0.046	3.760	135.000	0.767
17	0.024	0.356	0.009	3.712	141.000	0.734
18	0.026	0.158	0.026	4.769	139.000	0.378
19	0.044	0.165	0.102	3.595	149.000	0.468
20	0.034	0.226	0.161	3.295	129.000	0.571
21	0.017	0.454	0.017	1.544	83.000	0.762
22	0.035	0.376	0.033	1.946	116.000	0.910
23	0.043	0.259	0.481	4.818	72.000	0.792
24	0.044	0.438	0.345	2.573	129.000	1.181
25	0.015	0.409	0.014	1.096	81.000	0.573
26	0.022	0.357	0.013	1.560	107.000	0.609
27	0.016	0.312	0.009	2.095	102.000	0.464
28	0.072	0.191	0.229	3.616	126.000	0.567
29	0.049	0.215	0.286	3.561	126.000	0.554
30	0.037	0.208	0.041	3.491	124.000	0.497
31	0.025	0.218	0.023	3.342	119.000	0.450

Fig 10: A: Average decay equations at each site of equations where $r^2>.9$. Numbers adhere to site number, color is by regional group. Dotted red line is at clear water threshold marking distance *d*; B: Plot of average b^{-1} (y axis) C_0 (x axis) of each site's respective average decay equation. Numbers adhere to site number, color is by regional group. C) Table of average C_0, b^{-1}, standard deviation (σ) of both coefficients (C_0 and b), count of decay equations where $r^2>.9$, and distance of clear water threshold on average decay equation.

The C_0 and *b* coefficients were examined when dates were subset to wave quartiles (Q), as shown in the plots in Fig 11 and the table in Appendix III. The impact of H_S and WL on C_0 and *b* was investigated by calculating the average decay equation for each site within the following ranges:

- H_S: 0.44m to 1.11m (HsQ1), 1.11m to 1.48m (H_sQ2), 1.48m to 1.96m (H_sQ3), 1.96m to 5.03m (H_S Q4)
- WL: -0.23m to 0.84m (W_LQ1), 0.84m to 1.19m (W_LQ2), 1.19m to 1.48m (W_LQ3), 1.48m to 2.08m (W_LQ4)

All sites in the North Fort Ross region had the lowest C_0 values within the first quartile for all parameters. Ross Reef had the lowest C_0 for Hs (Q1Hs, C_0 = 0.0068 Lw), and North Fort Ross had the lowest C_0 for WL (Q1WL, C_0 = 0.0095 Lw). No regional group consistently had the highest C_0 across all sites, but Jewell Gulch had the highest C_0 for all both parameters (Q1Hs, C_0 = 0.0096 Lw; Q1WL, C_0 = 0.1296 Lw) (Appendix III).

Between Hs Q1 and Q4, Ross Reef and North of Russian Gulch (albeit a low image count of n=2 in HsQ4) saw the highest percent increase in C_0 (246.73% and 244.69%), while Timber Gulch/Jewell Gulch and Jewell Gulch had the largest decreases (-51.04% and -40.64%). Timber Cove had the smallest change (-0.64%). For b^{-1}, South Salmon Creek Beach (note low image count of n=1 in HsQ4) and North Wrights Beach had the highest increases (895.94% and 418.52%, respectively), while Elk Reserve was the only site with a decrease (-13.09%), and Bodega Head had the smallest change (4.02% decrease). On average, b increased by 153.83% and C_0 by 65.26% across sites between Hs Q1 and Q4.

Between WL Q1 and Q4, North of Russian Gulch and Ross Reef saw the highest C_0 increases (123.15% and 76.29%), while Pt Reyes Beach II and Timber Gulch had the largest decreases (-52.42% and -55.64%). Central Salmon Creek Beach and Tomales Point, Tip had the smallest changes (1.28% and -1.98%). For b^{-1}, Timber Gulch and Central Salmon Creek Beach had the highest increases (210.48% and 82.64%), while Timber Cove and North Fort Ross had the largest decreases (-26.49% and -31.50%). Jewell Gulch, South Salmon Creek Beach, and North of Russian Gulch saw minimal changes (2.39%, 2.25%, and -3.38% increase). On average, b increased by 47.71% and C_0 by 14.63% across sites between WL Q1 and Q4.

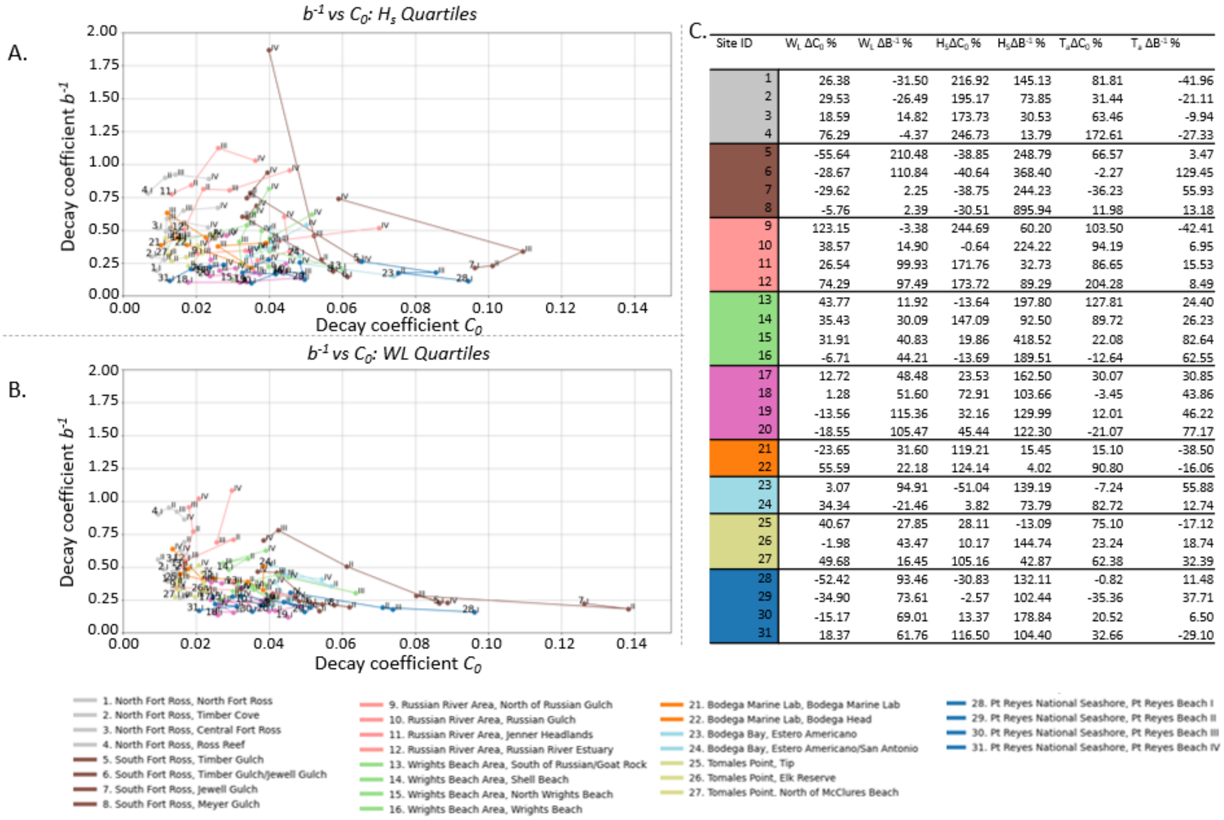

Site ID	W_L ΔC_0 %	W_L ΔB^{-1} %	$H_S \Delta C_0$ %	$H_S \Delta B^{-1}$ %	$T_a \Delta C_0$ %	T_a ΔB^{-1} %
1	26.38	-31.50	216.92	145.13	81.81	-41.96
2	29.53	-26.49	195.17	73.85	31.44	-21.11
3	18.59	14.82	173.73	30.53	63.46	-9.94
4	76.29	-4.37	246.73	13.79	172.61	-27.33
5	-55.64	210.48	-38.85	248.79	66.57	3.47
6	-28.67	110.84	-40.64	368.40	-2.27	129.45
7	-29.62	2.25	-38.75	244.23	-36.23	55.93
8	-5.76	2.39	-30.51	895.94	11.98	13.18
9	123.15	-3.38	244.69	60.20	103.50	-42.41
10	38.57	14.90	-0.64	224.22	94.19	6.95
11	26.54	99.93	171.76	32.73	86.65	15.53
12	74.29	97.49	173.72	89.29	204.28	8.49
13	43.77	11.92	-13.64	197.80	127.81	24.40
14	35.43	30.09	147.09	92.50	89.72	26.23
15	31.91	40.83	19.86	418.52	22.08	82.64
16	-6.71	44.21	-13.69	189.51	-12.64	62.55
17	12.72	48.48	23.53	162.50	30.07	30.85
18	1.28	51.60	72.91	103.66	-3.45	43.86
19	-13.56	115.36	32.16	129.99	12.01	46.22
20	-18.55	105.47	45.44	122.30	-21.07	77.17
21	-23.65	31.60	119.21	15.45	15.10	-38.50
22	55.59	22.18	124.14	4.02	90.80	-16.06
23	3.07	94.91	-51.04	139.19	-7.24	55.88
24	34.34	-21.46	3.82	73.79	82.72	12.74
25	40.67	27.85	28.11	-13.09	75.10	-17.12
26	-1.98	43.47	10.17	144.74	23.24	18.74
27	49.68	16.45	105.16	42.87	62.38	32.39
28	-52.42	93.46	-30.83	132.11	-0.82	11.48
29	-34.90	73.61	-2.57	102.44	-35.36	37.71
30	-15.17	69.01	13.37	178.84	20.52	6.50
31	18.37	61.76	116.50	104.40	32.66	-29.10

Fig 11: A & B: Average decay coefficients b^{-1} (y axis) vs C_0 when equations are subset to different quartiles of Hs (A) and WL (B) (x axis). Quartiles are marked by roman numerals above points in plot. Numbers adhere to site number, color is by regional group. C) Table of percent change C_0 and b^{-1} between quartiles 1 & 4 for each respective parameter.

The position of the $C_{threshold}$ was examined when applied to the decay equations derived within the quartiles of H_s and WL (see Fig 12 and Appendix IV). For Hs Q1, the shortest offshore distances were at North Fort Ross and Pt Reyes Beach IV (0.13 km), while Jenner Headlands had the longest (0.98 km). In WL Q1, North Salmon Creek Beach had the smallest distance (0.27 km), while Estero Americano had the largest (1.31 km).

In Hs Q4, Pt Reyes Beach IV had the shortest distance (0.54 km), while North Wrights Beach, North of Russian Gulch, and Jewell Gulch had the longest (2.54 km, 4.14 km, and 5.59 km, respectively). In WL Q4, North Fort Ross had the shortest distance (0.42 km), and Russian River Estuary the longest (2.17 km). Estero Americano had no data in WL Q4, as all data points surpassed the turbid threshold, adjusting the entire equation above the asymptote of $C_{threshold}$.

The impact of subsetting sites by wave parameters on *d* varied at each site. Between WL Q1 and Q4, the largest increase in offshore distance was at Central Salmon Creek Beach (195.01%), while Estero Americano saw a decrease (-8%). For Hs, North Wrights Beach had the largest increase (903.09%), and Elk Reserve the smallest (52.43%). Notably, the changes in C_0, b, and turbidity transport distance offshore were often non-linear between the first and fourth quartiles across many sites (Fig 13).

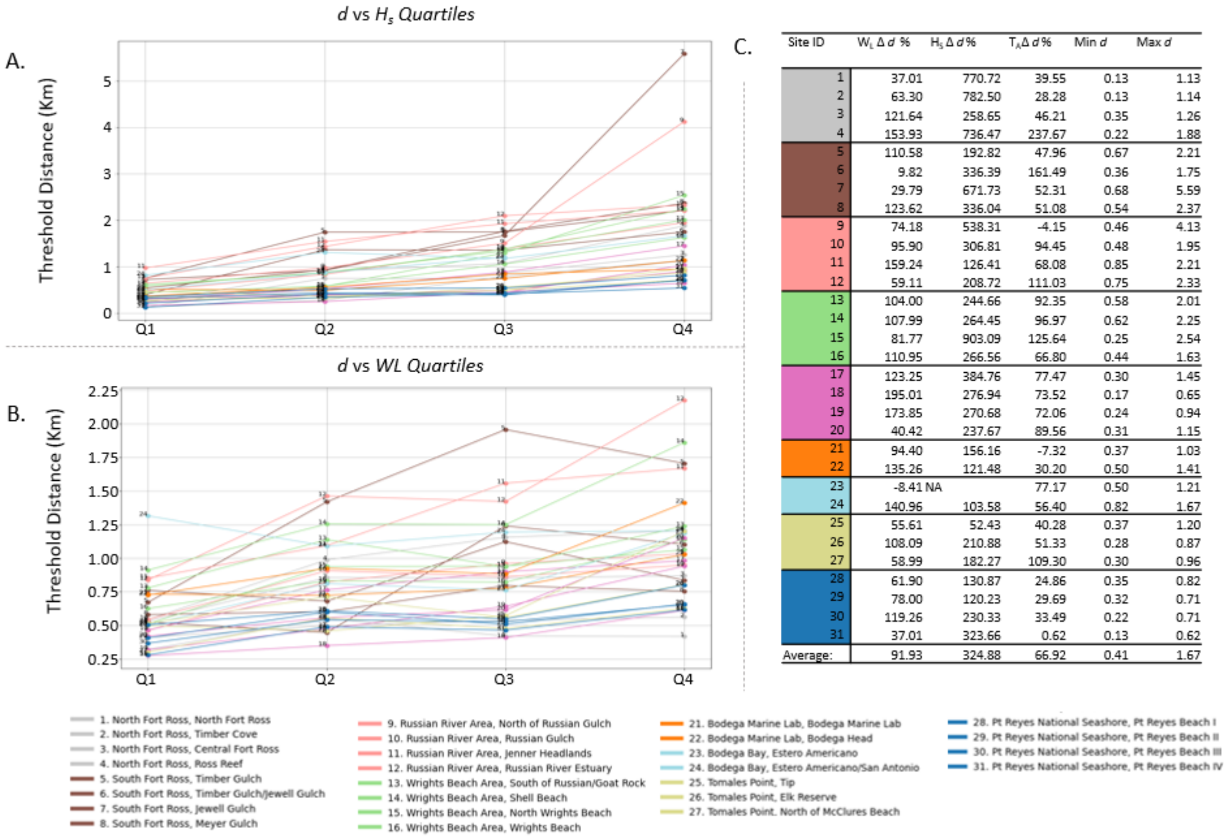

Site ID	W_L Δ *d* %	H_s Δ *d* %	T_A Δ *d* %	Min *d*	Max *d*
1	37.01	770.72	39.55	0.13	1.13
2	63.30	782.50	28.28	0.13	1.14
3	121.64	258.65	46.21	0.35	1.26
4	153.93	736.47	237.67	0.22	1.88
5	110.58	192.82	47.96	0.67	2.21
6	9.82	336.39	161.49	0.36	1.75
7	29.79	671.73	52.31	0.68	5.59
8	123.62	336.04	51.08	0.54	2.37
9	74.18	538.31	-4.15	0.46	4.13
10	95.90	306.81	94.45	0.48	1.95
11	159.24	126.41	68.08	0.85	2.21
12	59.11	208.72	111.03	0.75	2.33
13	104.00	244.66	92.35	0.58	2.01
14	107.99	264.45	96.97	0.62	2.25
15	81.77	903.09	125.64	0.25	2.54
16	110.95	266.56	66.80	0.44	1.63
17	123.25	384.76	77.47	0.30	1.45
18	195.01	276.94	73.52	0.17	0.65
19	173.85	270.68	72.06	0.24	0.94
20	40.42	237.67	89.56	0.31	1.15
21	94.40	156.16	-7.32	0.37	1.03
22	135.26	121.48	30.20	0.50	1.41
23	-8.41	NA	77.17	0.50	1.21
24	140.96	103.58	56.40	0.82	1.67
25	55.61	52.43	40.28	0.37	1.20
26	108.09	210.88	51.33	0.28	0.87
27	58.99	182.27	109.30	0.30	0.96
28	61.90	130.87	24.86	0.35	0.82
29	78.00	120.23	29.69	0.32	0.71
30	119.26	230.33	33.49	0.22	0.71
31	37.01	323.66	0.62	0.13	0.62
Average:	91.93	324.88	66.92	0.41	1.67

Fig 12: A & B: Average distance of offshore turbidity d (y axis) when equations are subset to different quartiles of Hs (A) and WL (B) (x-axis). Quartiles are marked by roman numerals above points in plot. Numbers adhere to site number, color is by regional group. C) Table of percent change in *d* between quartiles 1 & 4 for each respective parameter.

Fig 13 compares the averaged 2-dimensional bathymetric characteristics of each site, binned to 1 km offshore (see Appendix V for 0.5 km and 3.0 km binnings). The North Fort Ross group exhibits the highest cross-shore (ε_c) and alongshore roughness (ε_a), followed by South Fort Ross, Timber Gulch/Jewell Gulch, and Bodega Marine Lab sites. Pt Reyes National Seashore has the lowest roughness, with South Fort Ross, Timber Gulch showing even lower values, though data availability is limited in the 1 km bin (n = 317 pixels, compared to n = 172,576 pixels for Pt Reyes Beach IV). When considering the full 3 km bin, South Fort Ross, Timber Gulch ranks among the highest in roughness. After detrending, regional distinctions are more apparent, with North Fort Ross remaining the roughest, and South Fort Ross, Timber Gulch/Jewell Gulch having the second-highest roughness. Pt Reyes National Seashore sites display less uniform rugosity despite uniform shoreline geometry. North Fort Ross and Pt Reyes National Seashore have the highest depth change (Δh) and mean depth ($\bar{h}$), with North Fort Ross, North Fort Ross and Pt Reyes National Seashore, Pt Reyes Beach IV having the highest values within their respective groups.

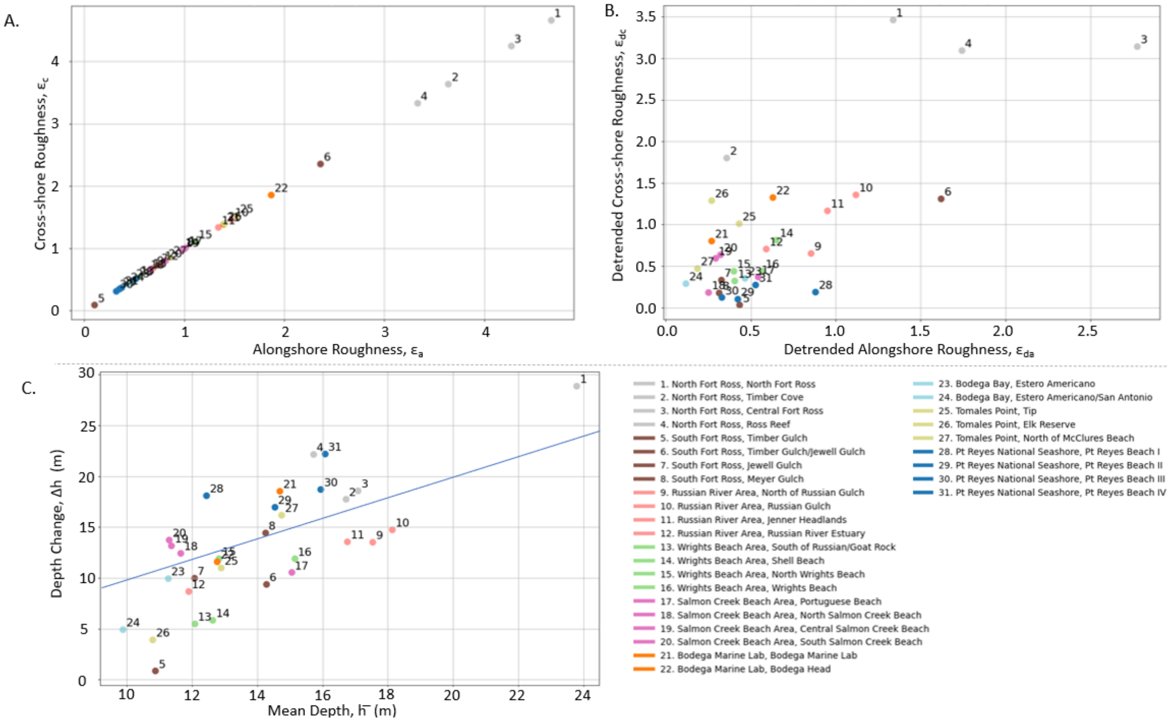

Fig 13: Various maps comparing the value of bathymetric statistics at each site binned below 1km offshore. A: Cross-shore roughness (y axis) vs alongshore roughness (x axis); B: Detrended cross-shore roughness (y axis) vs detrended alongshore roughness (x axis); C: Change in depth between shoreline and 1km point (y axis) vs average depth (x axis), both in absolute value. Blue line is 1:1 line between both variables.

The Spearman rank correlations between bathymetric variables and turbidity decay coefficients (C_0, b^{-1}, and d) from mean decay equations in different subsets of oceanographic parameter quartiles (H_s, WL) reveal intricate relationships that vary with distance from the shoreline and wave conditions, particularly in highest and lowest conditions (Q1 and Q4), as illustrated in heat maps in Fig 14a, 14b, and 14c.

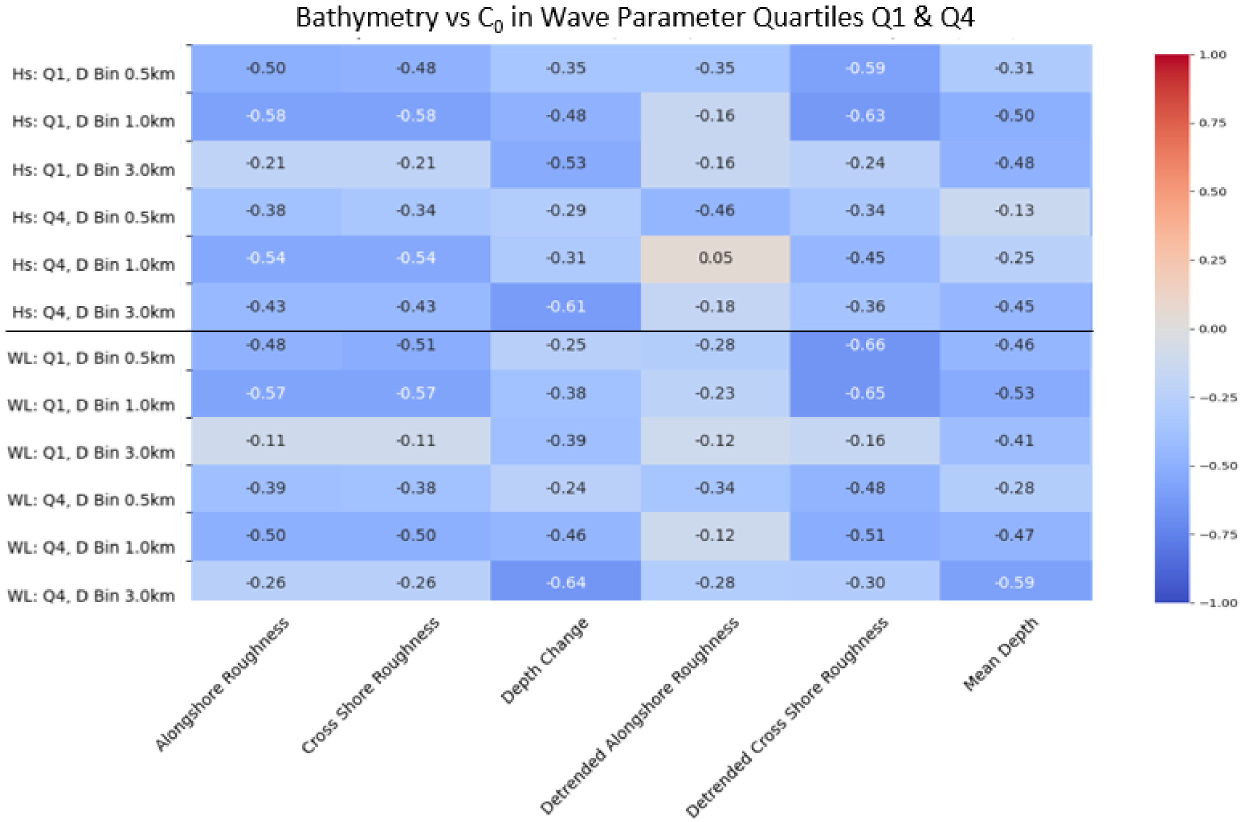

	Alongshore Roughness	Cross Shore Roughness	Depth Change	Detrended Alongshore Roughness	Detrended Cross Shore Roughness	Mean Depth
Hs: Q1, D Bin 0.5km	-0.50	-0.48	-0.35	-0.35	-0.59	-0.31
Hs: Q1, D Bin 1.0km	-0.58	-0.58	-0.48	-0.16	-0.63	-0.50
Hs: Q1, D Bin 3.0km	-0.21	-0.21	-0.53	-0.16	-0.24	-0.48
Hs: Q4, D Bin 0.5km	-0.38	-0.34	-0.29	-0.46	-0.34	-0.13
Hs: Q4, D Bin 1.0km	-0.54	-0.54	-0.31	0.05	-0.45	-0.25
Hs: Q4, D Bin 3.0km	-0.43	-0.43	-0.61	-0.18	-0.36	-0.45
WL: Q1, D Bin 0.5km	-0.48	-0.51	-0.25	-0.28	-0.66	-0.46
WL: Q1, D Bin 1.0km	-0.57	-0.57	-0.38	-0.23	-0.65	-0.53
WL: Q1, D Bin 3.0km	-0.11	-0.11	-0.39	-0.12	-0.16	-0.41
WL: Q4, D Bin 0.5km	-0.39	-0.38	-0.24	-0.34	-0.48	-0.28
WL: Q4, D Bin 1.0km	-0.50	-0.50	-0.46	-0.12	-0.51	-0.47
WL: Q4, D Bin 3.0km	-0.26	-0.26	-0.64	-0.28	-0.30	-0.59

Fig 14a. Heatmap showing the nonlinear correlation between bathymetry (x axis) and decay coefficient C_0 when decay equations are averaged within subsets of wave parameter (Hs & WL) quartiles 1 (Q1) and 4 (Q4) when bathymetric variables are subset to offshore distance bins (D Bin) 0.5km, 1.0km, and 2.0km.

For C_0, the strongest correlations in the 1 km distance bins are observed with detrended cross-shore roughness (ε_{dc}), which are consistently negative, especially in Q1 quartiles across oceanographic wave parameters. For example, ε_{dc} shows strong negative correlations with C_0 for Hs: Q1 at 1 km (ρ = -0.63) and WL: Q1 at 1 km (ρ = -0.66). These results suggest that smoother, shallower bathymetry promotes higher C_0, particularly under low wave energy and water levels. In the offshore bin (3 km), Δh shows moderate negative correlations with C_0 in Q4 conditions. In the 3 km, Δh shows moderate negative correlations with C_0 for each Q4 oceanographic parameter. However, these correlations are weaker in the 1km and under lower wave energy and tidal conditions. Mean depth $\bar{h}$ has stronger negative effects on C_0 in the 3km bins and under higher tidal levels. Collectively, these results indicate that smoother, shallower bathymetry promotes higher C_0, particularly under low wave energetics. However, bathymetry seems to have weaker control in higher wave energies and higher water level.

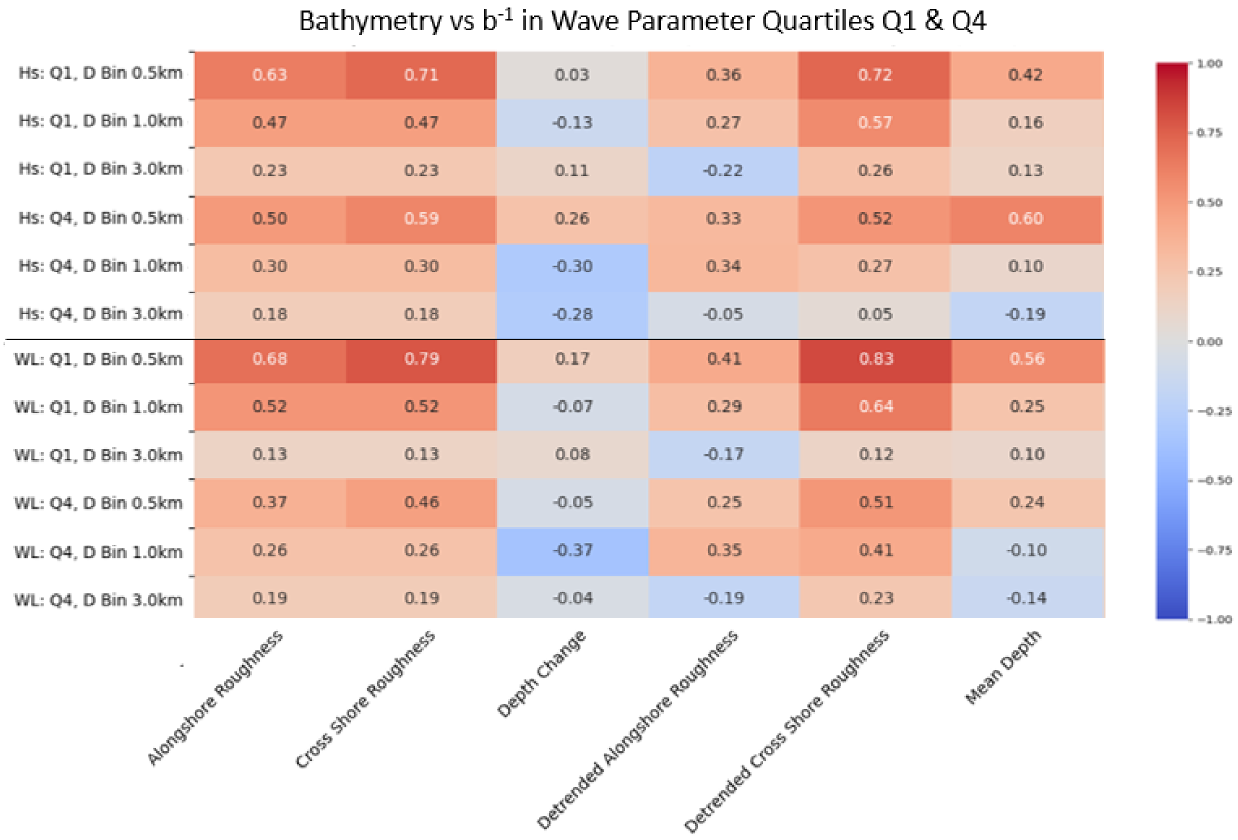

Fig 14b. Heatmap showing the nonlinear correlation between bathymetry (x axis) and decay coefficient b^{-1} when decay equations are averaged within subsets of wave parameter (Hs & WL) quartiles 1 (Q1) and 4 (Q4) when bathymetric variables are subset to offshore distance bins (D Bin) 0.5km, 1.0km, and 2.0km.

b^{-1} is most strongly influenced by roughness variables, especially in the nearshore bins under Q1 wave variable conditions, particularly under low water levels (Fig 14b). For example, εa shows strong negative correlations with b^{-1} for Hs: Q1 at 1 km (ρ = -0.71) and WL: Q1 at 1 km (ρ = -0.83). This suggests that rougher bathymetry results in a less steep cross-shore decay of turbidity. However, the significance of roughness weakens significantly at larger bins beyond the nearshore, particularly in higher quartiles. Conversely, Δh has a negative correlation with b^{-1} particularly in high wave energy and water level conditions. Correlations between $\bar{h}$ and b^{-1} are more strongly positive in the nearshore bins under low water levels and Hs conditions but become negligible to negative in other conditions.

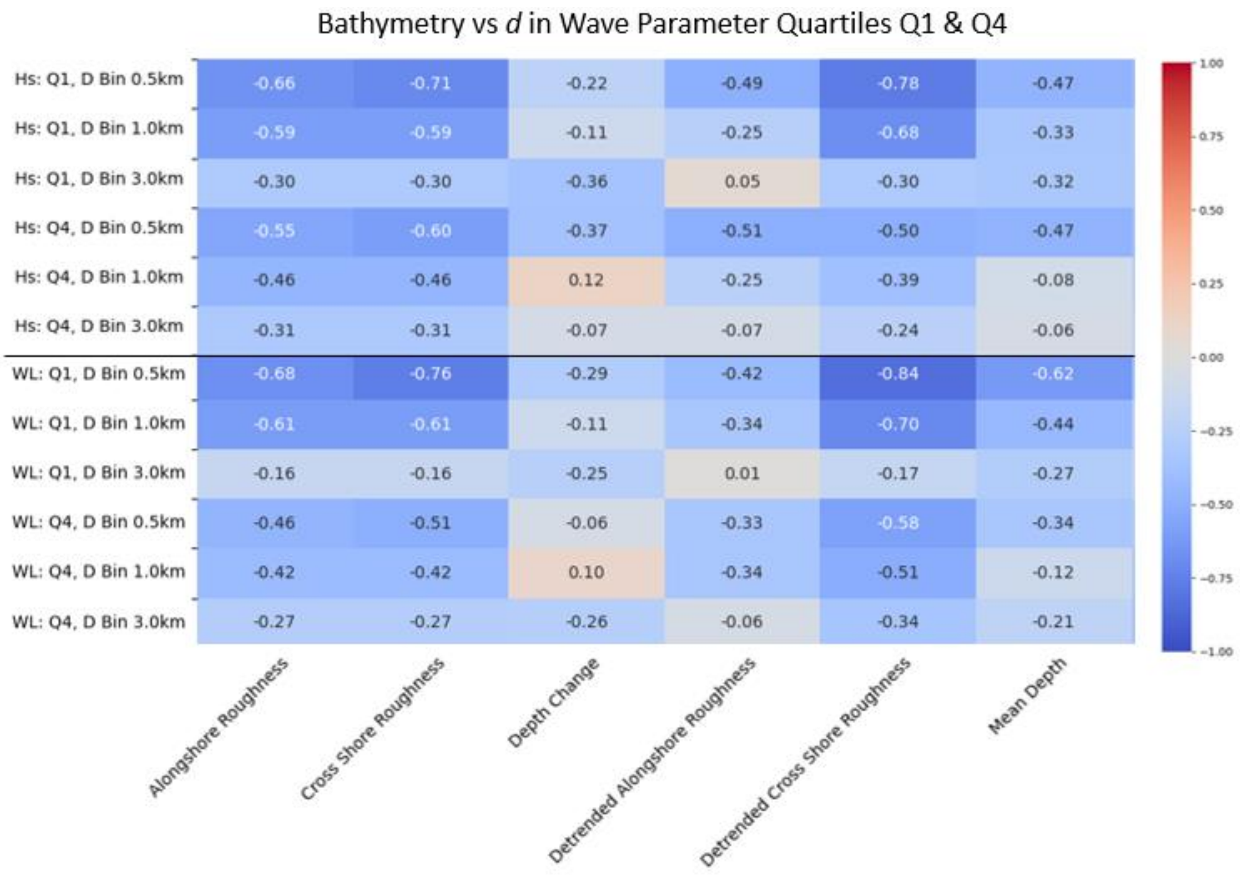

	Alongshore Roughness	Cross Shore Roughness	Depth Change	Detrended Alongshore Roughness	Detrended Cross Shore Roughness	Mean Depth
Hs: Q1, D Bin 0.5km	-0.66	-0.71	-0.22	-0.49	-0.78	-0.47
Hs: Q1, D Bin 1.0km	-0.59	-0.59	-0.11	-0.25	-0.68	-0.33
Hs: Q1, D Bin 3.0km	-0.30	-0.30	-0.36	0.05	-0.30	-0.32
Hs: Q4, D Bin 0.5km	-0.55	-0.60	-0.37	-0.51	-0.50	-0.47
Hs: Q4, D Bin 1.0km	-0.46	-0.46	0.12	-0.25	-0.39	-0.08
Hs: Q4, D Bin 3.0km	-0.31	-0.31	-0.07	-0.07	-0.24	-0.06
WL: Q1, D Bin 0.5km	-0.68	-0.76	-0.29	-0.42	-0.84	-0.62
WL: Q1, D Bin 1.0km	-0.61	-0.61	-0.11	-0.34	-0.70	-0.44
WL: Q1, D Bin 3.0km	-0.16	-0.16	-0.25	0.01	-0.17	-0.27
WL: Q4, D Bin 0.5km	-0.46	-0.51	-0.06	-0.33	-0.58	-0.34
WL: Q4, D Bin 1.0km	-0.42	-0.42	0.10	-0.34	-0.51	-0.12
WL: Q4, D Bin 3.0km	-0.27	-0.27	-0.26	-0.06	-0.34	-0.21

Fig 14c. Heatmap showing the nonlinear correlation between bathymetry (x axis) and the offshore distance of the clear water threshold when decay equations are averaged within subsets wave parameter (Hs & WL) quartiles 1 (Q1) and 4 (Q4) when bathymetric variables are subset to offshore distance bins (D Bin) 0.5km, 1.0km, and 2.0km.

Similarly, the strongest correlations between bathymetric variables and d are found in the nearshore bins and under less energetic wave and lower water level conditions (Fig 14c.). Alongshore roughness and cross-shore roughness exhibit strong negative correlations with d, particularly for Hs: Q1 at 1 km ($\rho = -0.80$) and WL: Q1 at 1 km ($\rho = -0.84$). These correlations weaken in higher wave energy scenarios, larger offshore bathymetry bins, and high-water levels. Positive correlations are observed between Δh and d in high wave energy and water level scenarios, suggesting that greater depth changes combined with stronger wave energies positively influence the offshore extent of turbidity. Overall, these correlations imply that in lower wave conditions, interaction areas with high roughness have limited offshore extent of turbidity. However, under high wave energy scenarios, roughness has negligible effects on the offshore reach of turbidity.

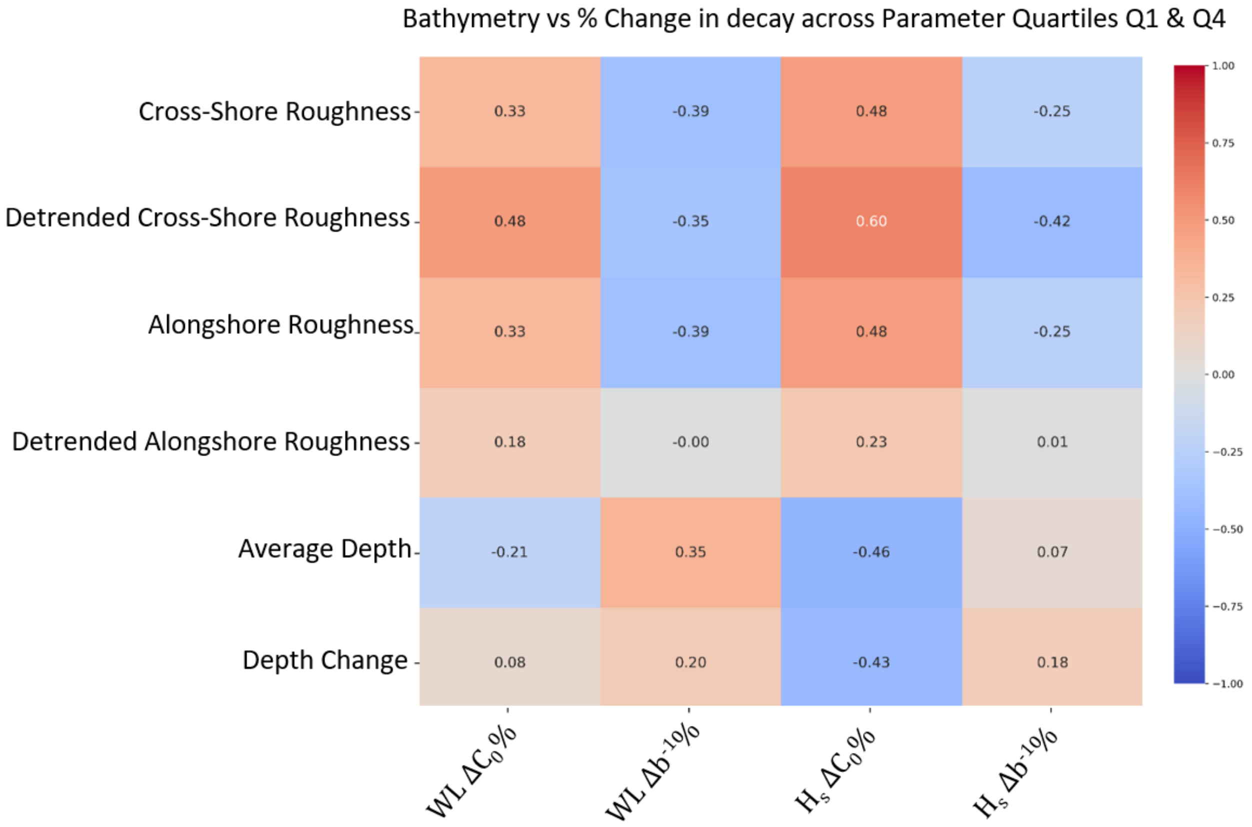
Bathymetry vs % Change in decay across Parameter Quartiles Q1 & Q4

	WL $\Delta C_0\%$	WL $\Delta b^{-1}\%$	H_s $\Delta C_0\%$	H_s $\Delta b^{-1}\%$
Cross-Shore Roughness	0.33	-0.39	0.48	-0.25
Detrended Cross-Shore Roughness	0.48	-0.35	0.60	-0.42
Alongshore Roughness	0.33	-0.39	0.48	-0.25
Detrended Alongshore Roughness	0.18	-0.00	0.23	0.01
Average Depth	-0.21	0.35	-0.46	0.07
Depth Change	0.08	0.20	-0.43	0.18

<u>Fig 15:</u> Heatmap showing the nonlinear correlation between bathymetry at sites (y axis) and percent change in decay coefficients (x axis) at each site. Cells are colored by strength of correlation.

In Fig 15, we examine correlations between bathymetric metrics binned at 1 km distances at each site and the percentage increase in C_0 and b^{-1} between lower and higher quartiles. Positive correlations are observed between roughness variables and C_0, with the highest being ε_{dc} and $Hs\Delta C_0\%$ ($\rho = .60$). Conversely, negative correlations are observed between roughness and increases in b^{-1}, with the lowest being $Hs\Delta b^{-1}\%$ ($\rho = -.42$). Depth variables show generally positive correlations with b^{-1} and negative correlations with C_0, though correlations between Δh and C_0 are negligible, except for $Hs\Delta C_0\%$ ($\rho = -.43$).

All the above correlations were also calculated with site-wise, coincident T_a data. The correlations relating to T_a were similar to those of H_s (albeit slightly weaker) and were not found to change the conclusions of this work. These results can be found within Appendix VI.

4. Discussion:

4.1 General Discussion

Past studies and visual inspection of individual satellite images show that turbidity laden with sediments can extend far offshore, starting at the shoreline. These turbid features can envelop kelp forests and drive organic material transport and the majority of sediment transport (Seymour, 2013) to deeper waters over the shelf. Through satellite images, such as those seen in Fig 1, observations of turbid patterns show distinct, coherent flow forms of offshore turbidity from rip currents on scales ranging from the surf zone (micro rip currents) to just past the breaker line (meso currents) to those extending up to kilometers offshore (macro rip currents) (Largier, 2022). Waves control this turbidity through initial mobilization of deposited sediments from shorelines and the seabed, driving erosion, and by controlling the hydrodynamics that further transport these mobilized sediments. These two steps, sediment mobilization and transport, are also controlled by their environment. Areas with larger caches of fine sediment, such as well-supplied regions near estuaries, confined areas like embayments, sandy shorelines, and regions with generally large sediment deposits such as kelp forests (Gaylord et al., 2012) have easily mobilized sediments (Green et al., 2004). Areas with complex coastlines and bathymetries have high kinetic energy as separation and turbulence and persistent channelization with solid features are common, enhancing energetics and transport (McMahan et al., 2023). However, these regions are often sediment-starved and further away from sediment sources, limiting the extent of turbid signals. Thus, areas with the most sediment availability and the greatest bathymetric and geomorphic complexity are likely to have the largest rip currents.

Furthermore, geometry of turbid features are also likely impacted by geomorphic complexity (Largier, 2022). Uniform regions with low bathymetric complexity, such as long sandy beaches, will often have uniformly spaced rip currents in the shape of radial plumes. Regions that are complex will have uneven rip current distributions with non-radial, unique shapes. These dynamics can be observed qualitatively through images. For instance, in Fig 1, columns A and C show examples of rip currents from bathymetrically complex, rocky regions. In column A, images come from a region near the Russian River, which is well-supplied with sediments, whereas in column C, which is a region in Salt Point, sources of sediments are far away. In both columns, rip shapes are complex, and their distribution is uneven. However, in Fig 1A.II, even in moderate wave conditions, meso rip currents extend over a kilometer offshore in two particularly well-sediment-supplied regions (near the Russian River Estuary and over a site with persistent kelp cover), but throughout all the Figs in column C, turbidity does not extend significantly past headlands and emanate from and are constrained within small headlands. In Fig 1, column B, we see three images along the uniform, sandy shores of the Pt Reyes seashore. In moderate wave conditions (Fig 1B.II), radially shaped meso rips are evenly distributed along the shoreline and have a moderate distance offshore. In high wave energy conditions, these shapes remain radial and evenly distributed; however, they do not extend nearly as far offshore as the well-fed rips from the rocky region in Column A on the same date.

In our study, using novel methodology in image post-processing and analysis combined with coincidental data and high-resolution bathymetric data, we quantitatively ground-truth the above statements and assumptions, illustrating the controls and interplay of geomorphology and wave energy in driving turbidity in the nearshore. The results in this study are two-part: the first consists of various maps of pixelwise statistics in which region-wide characteristics of surface turbidity and their geospatial correlation with wave energetics are presented, allowing us to stipulate where the surface is most variable and at its maximum, as well as its tie with correlation. The second part focuses on sitewise observation of the one-dimensional characteristics of turbidity cross-shore in the form of a turbidity decay equation, observed in their average condition at each site as conditionally subset in varying wave and tidal conditions. By further observation of these latter results, we can zero in on the conditions that result in the spatial distributions set in the first part, where turbidity transported with rip currents and correlation with wave energy vary geospatially, differing by geomorphic coastal environment.

4.2 Shoreline Supply/Erodibility: C_0

The turbidity decay coefficient, C_0, represents the initial maximum turbidity concentration before decay occurs as a function of offshore distance. Thus, it serves as an indicator of the erodibility of the local shoreline and the ease with which sediment is mobilized at the site's distance offshore (x) = 0m, or the closest shore-oriented position. Our results indicate that greater C_0 values are observed in sites with shallower bathymetries, particularly at lower water levels, where the increased contact between wave energy and the seafloor leads to proportionally higher shear stress throughout a shorter water column and sediment mobilization. This can be observed within the Pt Reyes National Seashore sites (28-31), where each site has respectively lower absolute first-kilometer average depth, $\bar{h}$, and C_0 values (Site 28: C_0 = .072 Lw, $\bar{h}$ = 12.43m; Site 29: C_0 = .029 Lw, $\bar{h}$ = 14.53m; Site 30: C_0 = .037 Lw, $\bar{h}$ = 15.94m; Site 31: C_0 = .025 Lw, $\bar{h}$ = 16.07m).

A strong negative correlation between C_0 and bathymetric roughness further supports the interpretation of C_0 as a metric of erodibility and mobility. Detrended cross-shore roughness, ε_{dc}, exhibits a strong negative correlation with C_0, with values as high $\rho = -0.63$ for Hs: Q1 at 1 km, and $\rho = -0.66$ for WL: Q1 at 1 km (Fig 14c). Areas with higher bathymetric roughness or rugosity, are often associated with features such as sea stacks, boulders, rocks, hummocks, and are often less rich in easily mobilized fine sediments (Green et al., 2004), leading to lower concentrations in initial sediment mobilization. Further, rougher areas maintain their roughness as rocks are less erodible, maintaining complex structure and not smoothing out like sand. This pattern is evident when comparing sites with varying rugosities but similar depths, such as Timber Cove in North Fort Ross (site 2: $\bar{h}$ = 16.71, ε_{dc} = 1.80, C_0 = 0.013 Lw) and the well-fed site just north of the Russian River

Estuary (site 11: $\bar{h}$ = 16.76, ε_{dc} = 1.17, C_0 = 0.018 Lw), or between the rocky shores of Bodega Marine Lab and the sea cliff fronted shores of Ross Reef in North Fort Ross (site 4: $\bar{h}$ = 15.72, ε_{dc} = 3.33, C_0 = 0.013 Lw) and the beach-fronted shores of Wrights Beach (site 16: $\bar{h}$ = 15.14, ε_{dc} = 0.63, C_0 = 0.038 Lw).

This explains why greater roughness is positively correlated with higher C_0 in decay equations averaged within higher wave quartiles (ρ = .60) as shown in Fig 15. Rougher sites, which generally lack readily suspensible sediments, require higher wave heights to induce significant C_0 concentrations, whereas lower wave heights are required to mobilize sediments in highly erodible or well-fed areas. Further, it is likely that bottom roughness dissipates near-bed fluid motion heights (Ruiz de Algeria-Arzaburu et al., 2013; Gallop et al., 2020; MacMahan et al., 2023), preventing mobilization, leading to lower mobilization particularly in low wave heights. Roughness also negatively influenced C_0 in low wave energy and low water level conditions, perhaps indicating that a higher ratio of water column contact with rougher bathymetries may trap sediments or dampen initial inducement of sediment suspension. This effect can also be interpreted in results in Fig 15, where ε_{dc} is positively correlated with increases in C_0 in decay equations subset to dates with lower quartile water levels (ρ = .48). At a site with high roughness, higher water levels lead to less bathymetric influenced reducing dampening caused by rugosity.

Our findings show that regions with shallow, smoother bathymetry are likely the most erodible and have reduced bottom shear, yielding the highest initial concentration of turbidity (C_0) from wave breaking. These results are consistent with well-fed coastlines observed throughout our study.

4.3 Wave-induced transport: b

The rate of decay of turbidity, represented by b^{-1}, serves as a measure of wave energetics and the ability of a site to transport sediments offshore, distinct from initial concentration amount

C0. Higher b^{-1} values correspond to less steep or rapid decay of C0, indicating that suspended sediments diminish less quickly with offshore distance and that turbidity extends further offshore. This parameter is influenced by both sediment characteristics, such as settling rate (Dietrich, 1982), and the hydrodynamics factors such as turbulence and horizontal shore-normal flow.

The rationalization of b^{-1} as a representation of transport energetics is supported by a strong positive correlation between b^{-1} and εdc (Fig 14b), values as high as ρ = -0.72 for Hs: Q1 at 0.5 km, and ρ = 0.83 for WL: Q1 at 0.5 km. Sites with high bathymetric roughness are found along complex coastlines, where structure yields gradients in wave setup and radiation stress that in turn promote rip currents (Castelle et al., 2016; Largier, 2022; MacMahan et al., 2023). Flow interaction with sea stacks, boulders, reefs, and headlands causes boundary and bathymetric rips, and complex coastlines and embayments promote bay rips. These factors enhance the transport extent of mobilized suspended sediments with higher energy flows and promote suspension residency from vertical flow. This also explains why depth change has the greatest negative correlations with b^{-1}, as limited contact with the bottom would decrease such interactions. Further, this bathymetric impact on flow energetics would also explain why the correlation between site roughness and decay b^{-1} is greatest in equations in low water levels, where there is maximum proportional contact of the entire water column with the bed and interaction with bathymetry causing separation. Further, higher b^{-1} in low water level conditions is consistent with studies that show decreasing water level may increase flow through constriction in channelized sandy intertidal bars (Austin et al., 2010; Scott et al., 2014), and rough bathymetries/reef morphologies. (MacMahan et al., 2023).

Roughness being highly correlated with positive b^{-1} in low water level conditions is consistent with sandy bathymetries, such as sites 11 and 12 directly in front of the Russian River, 19 and 20, 28-31, and 23, experiencing greater increases in b^{-1} with increasing water level, whereas rockier shores, such as those in Tomales Point, between the two esteros in Bodega Bay (site 24), rockier regions in Wright Beach Area, and sites 7, 8, 9, and 10, experience low to negative changes in b^{-1} with increases in wave height. This follows with correlations in Fig 15, where increases in changes in b^{-1} in equations subset by water level are negatively correlated with site roughness (ρ = -0.35) and positively correlated with site depth (ρ = 0.35). Further, it explains the negative correlation between site roughness and percent change in b^{-1} in decay equations within higher wave quartiles (ρ = -0.42), as rockier sites do not need as significant wave heights to induce greater b^{-1} as their wave energetics are already enhanced at the site as opposed to sandy sites that have less bathymetric influences on transport.

Therefore, the highest b^{-1} values are found along rough coastlines, which are rocky and complex- such structures yield gradients in wave setup and radiation stress that promote rip currents and flow separation, enhancing offshore sediment transport. Because of their structure, rocky systems are less controlled by Hs to induce transport than non-complex sandy shores. b^{-1} is enhanced by low water level conditions, particularly in rougher, rockier bathymetry.

4.4 Wave Induced Transport of Turbidity: C_0 & b

The interplay between C_0 and b^{-1} is crucial for understanding the extent of offshore turbidity, *d*. Following the above discussions, areas with a high initial supply of sediments (C_0) but a low b^{-1} are likely to exhibit short turbid rips, or high suspended sediment at the shoreline with little offshore transport. In contrast, areas with either high or low C_0 and high b^{-1} values indicate large rip currents or significant transport of sediments offshore of differing turbidity. This resolves why, on average, *b* increased more significantly in higher quartile Hs decay equations than C_0, as *b* is a direct measure of energetics, while Hs is a control of C_0, but not necessarily the same mechanic, as turbidity supply varies by site. This also resolves why there is a strong linear correlation (r = .75) between offshore distance of $C_{threshold}$ when plugged into average decay equations, d at each site with average *b* value but negligible linear correlation between d and C_0 at each site (r = .05).

The positive correlation between roughness and an increase in C_0 in decay equations averaged within higher wave quartiles ($\rho = 0.60$), as shown in Fig 16, suggests that rougher sites require higher wave heights to induce higher C_0 concentrations, as they do not have readily suspensible sediments at low wave energy scenarios. In contrast, lower wave heights are likely sufficient to mobilize sediments in highly erodible areas, making them less dependent on wave energy for sediment mobilization. The negative correlation between site roughness and percent change in b^{-1} in decay equations within higher wave quartiles suggests that rougher sites may not require as significant wave heights to increase b^{-1}, as wave energetics are already enhanced at these sites.

Higher wave energy induces the most significant increases in both C_0 and b^{-1}. However, in the absence of high wave heights, sites need to be both well-fed with sediments (to maximize C_0) and have complex bathymetry (to maximize b^{-1}) to achieve extensive offshore turbidity. Conversely, rough sites that are poorly supplied with sediments require higher wave heights to increase C_0, while smooth sites need greater wave heights to promote higher b^{-1} values.

4.5 Controls on transport extent and region wide turbidity

From these results, it is evident that to maximize the distance offshore, a balance must be met between low depth, sufficient sediment supply, and adequate bathymetric and shoreline complexity to induce larger rip currents. Comparisons between the North Fort Ross and Point Reyes National Seashore groups further highlight the influence of roughness on sediment transport. Despite having similar Δh values, sites in these groups exhibit different decay patterns. For example, Pt Reyes Beach IV (site 31, $\Delta h = 22.22$m, $\varepsilon_{dc} = 0.28$) had an offshore transport distance of d = 0.45, while Ross Reef (site 4, $\Delta h = -22.18$m, $\varepsilon_{dc} = 3.10$) had d = 0.99. Additionally, the offshore distance is the same at PT Reyes Beach II (site 29, $\Delta h = 16.98$, $\varepsilon_{dc} = 0.10$) and Timber Cove (site 2,

$\Delta h = 17.77$, $\varepsilon_{dc} = 1.80$), despite differences in Δh and ε_{dc} values. Similarly, Pt Reyes Beach III (site 30, $\Delta h = -18.72$m, $\varepsilon_{dc} = 0.12$) had d = 0.497, while Central Fort Ross (site 3, $\Delta h = -18.60$m, $\varepsilon_{dc} = 3.14$) had d = 0.84. Further, the Bodega Marine Lab site (site 21, $\Delta h = -18.53$m, $\varepsilon_{dc} = 0.81$) had both an offshore distance (d = 0.762) and roughness between those of Pt Reyes Beach III and Central Fort Ross, further supporting the role of roughness in modulating sediment transport.

The South Fort Ross group further illustrates the interplay between roughness and depth in determining sediment transport. Among Mid Jewell/Timber ($\varepsilon_{dc} = 1.31$, $\Delta h = -9.37$), Jewell Gulch ($\varepsilon_{dc} = 0.34$, $\Delta h = -9.99$), and Meyer Gulch ($\varepsilon_{dc} = 0.18$, $\Delta h = -14.44$), the steeper, deeper, and less rough sites exhibited further offshore transport of turbidity (d = 0.858km, d = 0.811km, and d = 0.677km, respectively). Timber Gulch had a significantly higher offshore distance and the greatest average distance of all sites (d = 1.653) and is likely very shallow given that data is effectively unavailable within 1 km of the shore.

Furthermore, all variables should be taken in balance, where *d*, as a function of turbidity, can be limited by low C_0, despite high *b* values. For instance, while the North Fort Ross sites exhibit the highest roughness across shore, they also exhibit the largest Δh, and have low d values. Thus, while transport energetics in rough regions may not be limited, a small supply of sediment will cause a small offshore extent as there is less suspended sediment to transport. In contrast, the sites with the largest transport have high roughness, low to moderate depths, and are also characteristically highly supplied by sediments. This is also well observed in the areas closest to the front of the Russian River estuary (sites 11 & 12), where offshore the average extents of turbid rip currents are great (d = 1.34km; d = 1.52km). Further, at the site with the highest offshore turbidity, site 5, we observe in both geospatial data of kelps, albeit prior to the temporal extent of the study, as well as through observation in high-resolution satellite imagery of the area, that the South Fort Ross area is abundant in kelps, so sediments are likely trapped and well supplied in this region.

High-resolution, recent data on regional Kelp Forest Coverage would greatly benefit these conclusions.

Our findings suggest that regions with shallow, smoother bathymetry are likely the most erodible and yield the highest initial concentration from wave breaking. These areas are consistent with well-fed sandy coastlines throughout our study. We find that rocky regions have the most turbulent and energetic environments and promote the most substantial vertical (upward) and offshore flows (b^{-1}). However, these two terms are separate, and for rocky regions to maximize the offshore extent of turbidity (d), regions need to be sufficiently well-fed by sediments (sufficient C_0).

Maps of turbid extent and correlation with wave energetics further elucidate these findings. Areas rich in sediment availability, such as regions well supplied with sand, like in front of the Russian River Estuary and Gualala Estuary, on average have higher turbidity extending further off the coast (Fig 7). These sediment-rich regions, as well as towards the headland boundaries of littoral cells where sediments are well confined, such as towards the south end of Point Reyes and near the Mussel Point Headland in Salmon Creek Beach, are those that also have the highest increase in offshore extent of turbidity in higher Hs percentiles (Fig 8).

However, while those sites are on average the most turbid, the ones that are most highly correlated with wave height are those with rocky bathymetries in Fig 9, with plentiful sea stacks, such as those in the South Fort Ross Region, the sea cliffs northward of the Gualala and Russian River Estuary, and the rocky, sheltered embayments between the two estuaries. This can also be seen when zooming in on correlation results of the Russian River Estuary in Fig 9B., where near the shore nearest to the estuary does not display high correlation values, but contours do form around the sea stacks 1km adjacent to the estuary.

These maps express the independence and the interplay between the controls of rip currents and offshore flow. Sandy regions such as Salmon Creek Beach have large caches of sediment which are easily suspended. However, their lack of bathymetric complexity, particularly away from their headlands, limits their correlation with wave energy, limiting the offshore transport of turbidity. Rocky regions are well correlated with wave energy, however, they are lacking sufficient erodibility for offshore flow to be fully observed as turbulent, as their coarser sediments settle quickly and are at a low initial turbidity (Green et al., 2004). The sites that produce the greatest offshore signals are those that are well-fed and bathymetrically complex.

5. Conclusion:

This study investigates the complex interplay between coastal geomorphology and wave dynamics in driving nearshore turbidity, with particular focus comparing the transport characteristics across diverse coast types between rocky and sandy shores. Using both novel methodologies in image-post processing to deal with nearshore heterogeneity, as well novel methods that integrate these processed data with high resolution bathymetry and coincidental, distributed modeled wave energy data, we have quantified the spatial patterns of wave-driven turbidity sitewide through maps and have isolated the factors that constrain its offshore extent across diverse coastal environments (rocky and sandy shores) and oceanographic climates by observing the distribution of cross-shore turbidity as a function of distance as a decay equation, isolating decay coefficients as important signals of sediment mobilization (C_0) and length scale decay (b^{-1}).

Our research builds on the understanding that suspended sediment turbidity can extend far offshore under the influence of rip currents generated by wave action. While previous studies have primarily focused on doing so in sandy shores and qualitatively in rocky shores, our methodology provides a quantitative framework for assessing the relative contributions of shoreline sediment supply and erodibility, C_0, wave induced transport, b^{-1}, wave height, Hs, and bathymetric complexity to offshore turbidity.

Shores with low cross-shore detrended bathymetric roughness and/or sandy, erodible shores, particularly near estuaries and embayments, exhibit high initial turbidity concentrations (C_0). These well-fed sandy regions demonstrate that sediments are readily suspended under lower wave energy, leading to significant shoreline turbidity. However, sandy shores lacking bathymetric complexity cannot sustain significant offshore transport, especially along uniform shorelines, without significant wave energy.

In contrast, rocky shores and complex shorelines exhibit distinct behavior. Complex bathymetry and high roughness promote stronger offshore transport (high b^{-1}) even in low wave height conditions due to flow separation and persistent channelization. This transport is enhanced during low tides. However, these rough sites often lack available sediments and or have rough bottom bathymetry dampening shear stress, resulting in low C_0 values in ambient wave conditions. Consequently, they rely on higher wave energy to drive the turbid signals of their flow. Despite this, the inherent roughness of complex shorelines leads to ambiently high b^{-1} values, particularly in low water level. Sites with the greatest offshore turbidity extent have a combination of high roughness, low to moderate depths, and abundant sediment supply, as observed near the Russian River and Gualala River estuaries.

Maps of turbid extent and correlation with wave energetics further elucidate these findings. Regions well-supplied with sediment and high bathymetric and coastline complexity, such as those near estuaries fronted by sea stacks, near headlands, and rocky kelp forests, exhibit higher average turbidity extending further offshore, with the greatest increase in offshore extent under higher waves. Sites most highly correlated with wave height (wave transport) are those with rocky bathymetries, plentiful nearshore sea stacks, and complex shorelines. The interplay between sediment availability and bathymetric complexity is evident in the Russian River Estuary, where areas nearest the estuary lack high correlation values despite ample sediment, while strong correlations form around adjacent sea stacks and boundaries.

This study highlights the importance of considering both sediment availability and geomorphic complexity when examining nearshore turbidity dynamics. Areas with the most substantial offshore turbidity signals are both well-supplied with sediments and have complex bathymetries. Our findings provide a quantitative basis for understanding factors controlling turbidity transport in diverse coastal settings, with implications for sediment budgets, coastal ecosystems, and management strategies, particularly in areas where understanding of water column geochemistry in rocky shores is essential such as in vulnerable kelp forests.

Future research could incorporate in-situ measurements and hydrodynamic modeling to validate and refine satellite-based observations and investigate three-dimensional dynamics of rip currents and sediment transport. Temporal considerations, such as seasonality in precipitation, sediment supply, wave climatology, and onshore morphology, would further enhance our understanding of these complex systems. Lastly, more comprehensive and specific maps of beach and coastline geomorphological classifications would aid in this study. Nonetheless, our study provides a novel, quantitative approach to characterizing nearshore turbidity across geomorphologically diverse coastlines, shedding light on the intricate interplay between sediment availability, wave forcing, and coastal geomorphology.

Acknowledgements:

Conversations with Douglas George and Gonzalo Saldías contributed to this work, particularly in conceptual design and analysis.

References

Aagaard, T., Greenwood, B., & Nielsen, J. (1997). Mean currents and sediment transport in a rip channel. Marine Geology, 140(1-2), 25-45.

Adams, P. N., Inman, D. L., & Lovering, J. L. (2011). Effects of climate change and wave direction on longshore sediment transport patterns in Southern California. Climatic Change, 109(1), 211-228.

de Alegria-Arzaburu, A. R., Mariño-Tapia, I., Enriquez, C., Silva, R., & González-Leija, M. (2013). The role of fringing coral reefs on beach morphodynamics. *Geomorphology*, *198*, 69-83

Almar, R., Castelle, B., Ruessink, B. G., Sénéchal, N., Bonneton, P., & Marieu, V. (2014). Two-and three-dimensional double-sandbar system behaviour under intense wave forcing and a meso–macro tidal range. Continental Shelf Research, 30(7), 781-792.

Austin, M., Scott, T., Brown, J., Brown, J., MacMahan, J., Masselink, G., & Russell, P. (2010). Temporal observations of rip current circulation on a macro-tidal beach. Continental Shelf Research, 30(9), 1149-1165.

Austin, M. J., Scott, T. M., Russell, P. E., & Masselink, G. (2012). Rip current prediction: development, validation, and evaluation of an operational tool. Journal of Coastal Research, 29(2), 283-300.

Barnard, P. L., O'Reilly, B., van Ormondt, M., Elias, E., Ruggiero, P., Erikson, L. H., ... & Hapke, C. (2009). The framework of a coastal hazards model—a tool for predicting the impact of severe storms. U.S. Geological Survey Open-File Report, 1–21.

Behrens, D. K., Bombardelli, F. A., Largier, J. L., & Twohy, E. (2013). Episodic closure of the tidal inlet at the mouth of the Russian River—A small bar-built estuary in California. Geomorphology, 189, 66-80.

Bell, T. W., Cavanaugh, K. C., Reed, D. C., & Siegel, D. A. (2015). Geographical variability in the controls of giant kelp biomass dynamics. Journal of Biogeography, 42(10), 2010-2021.

Bell, T. W., Allen, J. G., Cavanaugh, K. C., & Siegel, D. A. (2020). Three decades of variability in California's giant kelp forests from the Landsat satellites. *Remote Sensing of Environment*, *238*, 110811.

Buscombe, D. (2023). CoastSeg: Semantic segmentation for very high resolution satellite imagery of coastal environments.

Castelle, B., Scott, T., Brander, R. W., & McCarroll, R. J. (2016). Rip current types, circulation and hazard. *Earth-Science Reviews*, *163*, 1-21.

Castelle, B., & Coco, G. (2013). Surf zone flushing on embayed beaches. Geophysical Research Letters, 40(10), 2206-2210.

Castelle, Bruno, and Gerd Masselink. "Morphodynamics of wave-dominated beaches." Cambridge Prisms: Coastal Futures 1 (2023): e1.

Cavanaugh, K. C., Siegel, D. A., Reed, D. C., & Dennison, P. E. (2011). Environmental controls of giant-kelp biomass in the Santa Barbara Channel, California. Marine Ecology Progress Series, 429, 1-17.

Coco, G., Senechal, N., Rejas, A., Bryan, K. R., Capo, S., Parisot, J. P., ... & MacMahan, J. H. M. (2014). Beach response to a sequence of extreme storms. Geomorphology, 204, 493-501.

Dettinger, M. D., Ralph, F. M., Das, T., Neiman, P. J., & Cayan, D. R. (2011). Atmospheric rivers, floods and the water resources of California. Water, 3(2), 445-478.

Dietrich, W. E. (1982). Settling velocity of natural particles. *Water resources research*, *18*(6), 1615-1626.

Dogliotti, A. I., Ruddick, K. G., Nechad, B., Doxaran, D., & Knaeps, E. (2015). A single algorithm to retrieve turbidity from remotely-sensed data in all coastal and estuarine waters. Remote Sensing of Environment, 156, 157-168.

Drusch, M., Del Bello, U., Carlier, S., Colin, O., Fernandez, V., Gascon, F., ... & Bargellini, P. (2012). Sentinel-2: ESA's optical high-resolution mission for GMES operational services. Remote sensing of Environment, 120, 25-36.

European Space Agency. (2015). Sentinel-2 User Handbook. European Space Agency.

Fitzpatrick, S., Buscombe, D., Warrick, J. A., Lundine, M. A., & Vos, K. (2024). CoastSeg: an accessible and extendable hub for satellite-derived-shoreline (SDS) detection and mapping. *Journal of Open Source Software*, *9*(99), 6683.

Gallop, S. L., Kennedy, D. M., Loureiro, C., Naylor, L. A., Muñoz-Pérez, J. J., Jackson, D. W., & Fellowes, T. E. (2020). Geologically controlled sandy beaches: Their geomorphology, morphodynamics and classification. *Science of the Total Environment*, *731*, 139123.

Garcia-Reyes, M., & Largier, J. L. (2012). Seasonality of coastal upwelling off central and northern California: New insights, including temporal and spatial variability. Journal of Geophysical Research: Oceans, 117(C3).

Gaylord, B., Nickols, K. J., & Jurgens, L. (2012). Roles of transport and mixing processes in kelp forest ecology. The Journal of Experimental Biology, 215(6), 997-1007.

George, D. A., Largier, J. L., Storlazzi, C. D., & Barnard, P. L. (2015). Classification of rocky headlands in California with relevance to littoral cell boundary delineation. Marine Geology, 369, 137-152.

George, D. A., Largier, J. L., Pasternack, G. B., Barnard, P. L., Storlazzi, C. D., & Erikson, L. H. (2019). Modeling sediment bypassing around idealized rocky headlands. *Journal of Marine Science and Engineering*, *7*(2), 40.

Gordon, H. R., & Wang, M. (1994). Influence of oceanic whitecaps on atmospheric correction of ocean-color sensors. *Applied optics*, *33*(33), 7754-7763.

Green, M. O., Vincent, C. E., & Trembanis, A. C. (2004). Suspension of coarse and fine sand on a wave-dominated shoreface, with implications for the development of rippled scour depressions. Continental Shelf Research, 24(3), 317-335.

Griggs, G. B., & Hein, J. R. (1980). Sources, dispersal, and clay mineral composition of fine-grained sediment off central and northern California. The Journal of Geology, 88(5), 541-566.

Holman, R. A., & Haller, M. C. (2013). Remote sensing of the nearshore. Annual review of marine science, 5, 95-113.

Jaffe, B. E., Sternberg, R. W., & Sallenger, A. H. (1984). The role of suspended sediment in shore-normal beach profile changes. Coastal Engineering 1984 (pp. 1983-1996).

Killeen, H., Parker, M., Morgan, S. G., Largier, J. L., Susner, M. G., Dibble, C., & Dann, D. (2023). Small-scale topographic fronts along an exposed coast structure plankton communities. *Estuarine, Coastal and Shelf Science*, *293*, 108474.

Lahet, F., & Stramski, D. (2010). MODIS imagery of turbid plumes in San Diego coastal waters during rainstorm events. Remote Sensing of Environment, 114(2), 332-344.

Largier, J. L., Magnell, B. A., & Winant, C. D. (1993). Subtidal circulation over the northern California shelf. Journal of Geophysical Research: Oceans, 98(C10), 18147-18179.

Largier, J. L. (2022). Rip currents and the influence of morphology on wave-driven cross-shore circulation.

Lawson, S. E., Wiberg, P. L., McGlathery, K. J., & Fugate, D. C. (2007). Wind-driven sediment suspension controls light availability in a shallow coastal lagoon. Estuaries and Coasts, 30(1), 102-112.

Loureiro, C., Ferreira, Ó., & Cooper, J. A. G. (2012). Extreme erosion on high-energy embayed beaches: influence of megarips and storm grouping. Geomorphology, 139, 155-171.

MacMahan, J. H., Thornton, E. B., & Reniers, A. J. (2006). Rip current review. Coastal Engineering, 53(2-3), 191-208.

MacMahan, J., Thornton, E., Patria, N., Gon, C., & Denny, M. (2023). Rip Currents Off Rocky-Shore Surge Channels. *Journal of Geophysical Research: Oceans*, *128*(8), e2022JC019317.

Masselink, G., & Short, A. D. (1993). The effect of tide range on beach morphodynamics and morphology: a conceptual beach model. Journal of Coastal Research, 785-800.

McCarroll, R. J., Brander, R. W., MacMahan, J. H., Turner, I. L., Reniers, A. J. H. M., Brown, J. A., ... & Bradstreet, A. (2014). Evaluation of swimmer-based rip current escape strategies. Natural hazards, 71(3), 1821-1846.

Mendes, R., Vaz, N., Fernández-Nóvoa, D., Da Silva, J. C. B., Decastro, M., Gómez-Gesteira, M., & Dias, J. M. (2014). Observation of a turbid plume using MODIS imagery: The case of Douro estuary (Portugal). *Remote sensing of environment*, *154*, 127-138.

Morgan, S. G., Dibble, C. D., Susner, M. G., Wolcott, T. G., Wolcott, D. L., & Largier, J. L. (2021). Robotic biomimicry demonstrates behavioral control of planktonic dispersal in the sea. *Marine Ecology Progress Series*, *663*, 51-61.

Moulton, M., Elgar, S., Raubenheimer, B., Warner, J. C., & Kumar, N. (2017). Rip currents and alongshore flows in single channels dredged in the surf zone. Journal of Geophysical Research: Oceans, 122(5), 3799-3816.

Mukaka, M. M. (2012). A guide to appropriate use of correlation coefficient in medical research. Malawi medical journal, 24(3), 69-71.

Nechad, B., Ruddick, K. G., & Park, Y. (2010). Calibration and validation of a generic multisensor algorithm for mapping of total suspended matter in turbid waters. Remote Sensing of Environment, 114(4), 854-866.

Noyes, T. J., Guza, R. T., Elgar, S., & Herbers, T. H. C. (2004). Field observations of shear waves in the surf zone. Journal of Geophysical Research: Oceans, 109(C1).

O'Reilly, W. C., Olfe, C. B., Thomas, J., Seymour, R. J., & Guza, R. T. (2016). The California coastal wave monitoring and prediction system. Coastal Engineering, 116, 118-132.

Orzech, M. D., Thornton, E. B., MacMahan, J. H., O'Reilly, W. C., & Stanton, T. P. (2010). Alongshore rip channel migration and sediment transport. Marine Geology, 271(3-4), 278-291.

Patsch, K., & Griggs, G. B. (2007). Development of sand budgets for California's major littoral cells. *Calif. Coast. Rec. Proj*, 1-115.

Runyan, K., & Griggs, G. B. (2003). The effects of armoring seacliffs on the natural sand supply to the beaches of California. *Journal of coastal research*, 336-347.

Saldías, G. S., Largier, J. L., Mendes, R., Pérez-Santos, I., Vargas, C. A., & Sobarzo, M. (2016). Satellite-measured interannual variability of turbid river plumes off central-southern Chile: Spatial patterns and the influence of climate variability. *Progress in Oceanography*, *146*, 212-222.

Saldías, G. S., Sobarzo, M., Largier, J., Moffat, C., & Letelier, R. (2012). Seasonal variability of turbid river plumes off central Chile based on high-resolution MODIS imagery. *Remote Sensing of Environment*, *123*, 220-233.Seymour, R. J. (Ed.). (2013). *Nearshore sediment transport*. Springer Science & Business Media

Schober, P., Boer, C., & Schwarte, L. A. (2018). Correlation coefficients: appropriate use and interpretation. *Anesthesia & analgesia*, *126*(5), 1763-1768.

Shi, W., & Wang, M. (2009). An assessment of the black ocean pixel assumption for MODIS SWIR bands. Remote Sensing of Environment, 113(8), 1587-1597.

Short, A. D., & Masselink, G. (1999). Embayed and structurally controlled beaches. Handbook of beach and shoreface morphodynamics, 1, 230-250.

Sinnott, R. W. (1984). Virtues of the Haversine. Sky and Telescope, 68(2), 158.

Smith, J. A., & Largier, J. L. (1995). Observations of nearshore circulation: Rip currents. Journal of Geophysical Research: Oceans, 100(C6), 10967-10975.

Vanhellemont, Q. (2019). Adaptation of the dark spectrum fitting atmospheric correction for aquatic applications of the Landsat and Sentinel-2 archives. Remote Sensing of Environment, 225, 175-192.

Vanhellemont, Q., & Ruddick, K. (2015). Advantages of high quality SWIR bands for ocean colour processing: Examples from Landsat-8. Remote Sensing of Environment, 161, 89-106.

Vanhellemont, Q., & Ruddick, K. (2018). Atmospheric correction of metre-scale optical satellite data for inland and coastal water applications. *Remote sensing of environment*, *216*, 586-597.

Virtanen, P., Gommers, R., Oliphant, T. E., Haberland, M., Reddy, T., Cournapeau, D., ... & Van Mulbregt, P. (2020). SciPy 1.0: fundamental algorithms for scientific computing in Python. *Nature methods*, *17*(3), 261-272.

Vos, K., Splinter, K. D., Harley, M. D., Simmons, J. A., & Turner, I. L. (2019). CoastSat: A Google Earth Engine-enabled Python toolkit to extract shorelines from publicly available satellite imagery. Environmental Modelling & Software, 122, 104528.

Warrick, J. A., Mertes, L. A., Siegel, D. A., & Mackenzie, C. (2004). Estimating suspended sediment concentrations in turbid coastal waters of the Santa Barbara Channel with SeaWiFS. International Journal of Remote Sensing, 25(10), 1995-2002.

Warrick, J. A., Mertes, L. A., Washburn, L., & Siegel, D. A. (2004). Dispersal forcing of southern California river plumes, based on field and remote sensing observations. *Geo-Marine Letters*, *24*, 46-52.

Wright, L. D., & Short, A. D. (1984). Morphodynamic variability of surf zones and beaches: a synthesis. *Marine geology*, *56*(1-4), 93-118.

Appendix

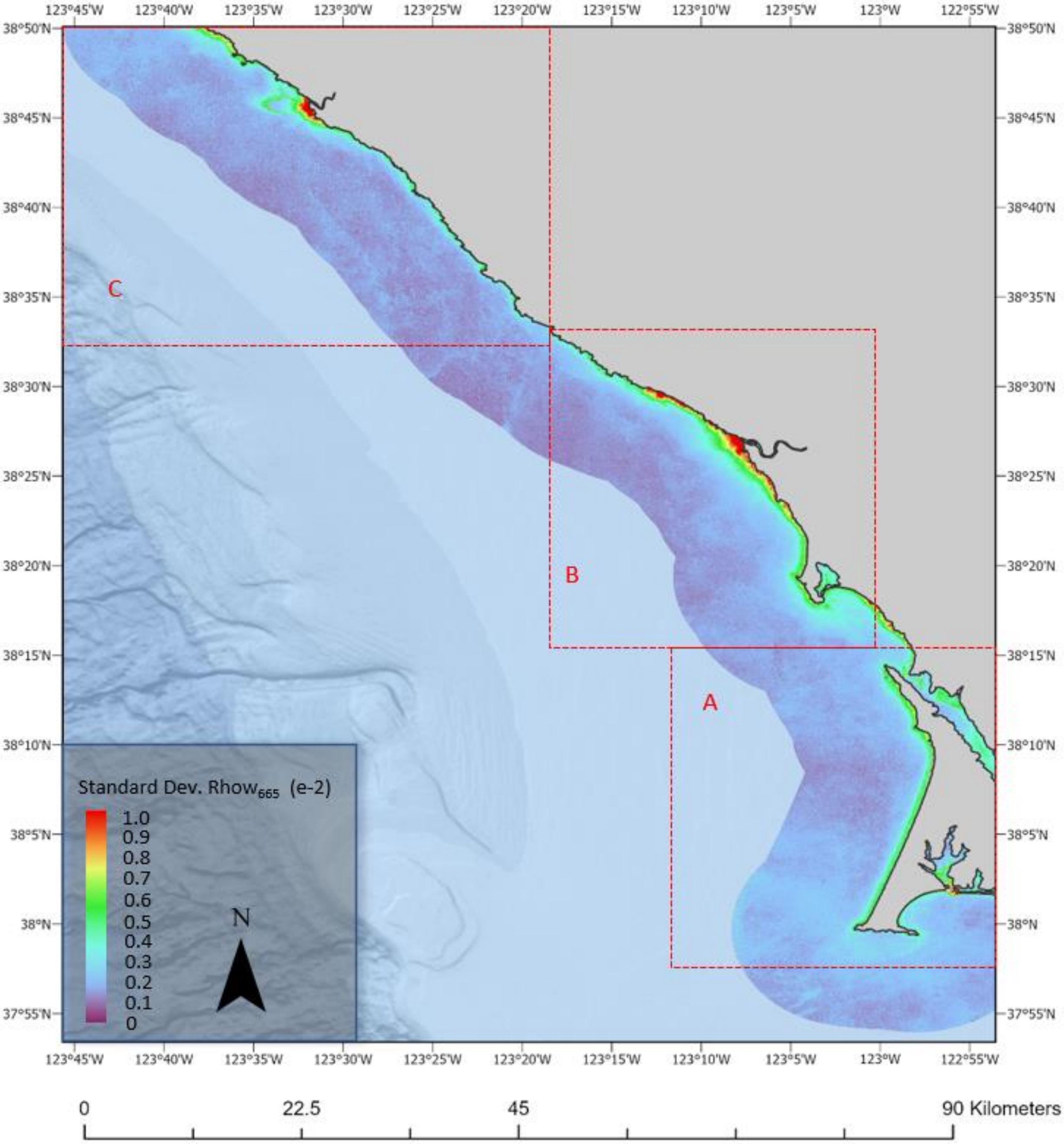

Appendix I: Map of standard deviation at each pixel location

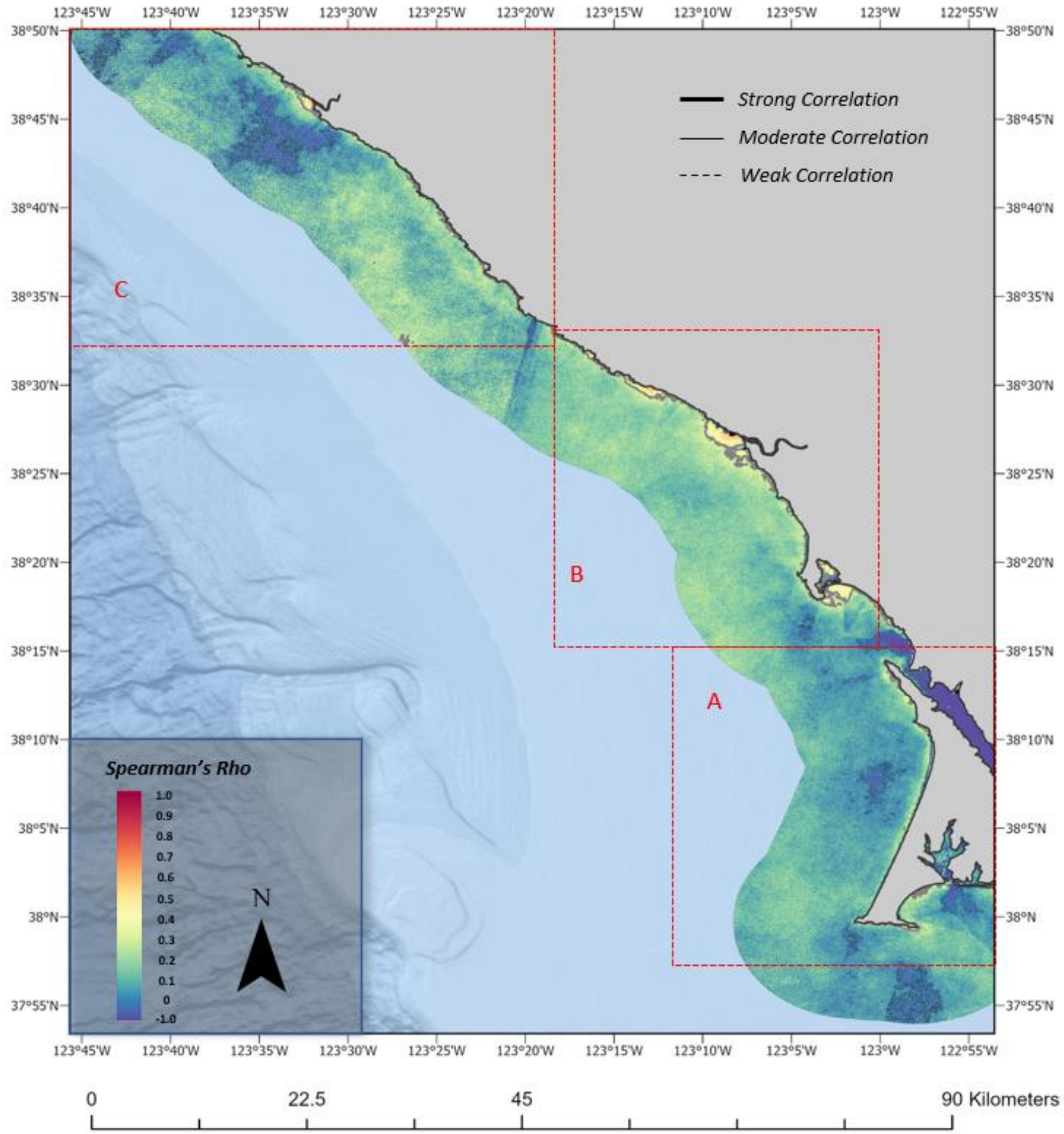

Appendix II: Correlation between rhow_{665} and nearest coincident Ta data at each pixel position.

S	*P*	Q_1C_0	Q_1b^{-1}	Q_1n	Q_2C_0	Q_2b^{-1}	Q_2n	Q_3C_0	Q_3b^{-1}	Q_3n	Q_4C_0	Q_4b^{-1}	Q_4n
1	WL	0.012	0.392	14	0.014	0.468	22	0.017	0.276	25	0.015	0.268	33
2	WL	0.011	0.484	16	0.010	0.560	21	0.014	0.423	29	0.014	0.356	41
3	WL	0.013	0.545	16	0.017	0.694	21	0.018	0.577	31	0.016	0.626	39
4	WL	0.009	0.904	13	0.013	0.954	19	0.015	0.924	22	0.017	0.864	34
5	WL	0.087	0.227	18	0.061	0.505	21	0.042	0.780	31	0.038	0.705	48
6	WL	0.052	0.222	25	0.054	0.168	26	0.042	0.458	25	0.037	0.467	49
7	WL	0.126	0.224	24	0.138	0.183	26	0.080	0.282	33	0.089	0.229	52
8	WL	0.058	0.211	27	0.062	0.197	27	0.048	0.242	33	0.054	0.217	52
9	WL	0.014	0.346	15	0.031	0.324	19	0.030	0.385	25	0.032	0.335	41
10	WL	0.034	0.237	23	0.047	0.293	22	0.041	0.304	27	0.047	0.273	40
11	WL	0.016	0.510	16	0.019	0.774	20	0.018	0.957	26	0.021	1.020	31
12	WL	0.017	0.549	25	0.030	0.711	28	0.026	0.689	30	0.030	1.083	48
13	WL	0.031	0.377	27	0.042	0.440	31	0.064	0.304	35	0.045	0.422	51
14	WL	0.029	0.482	45	0.034	0.566	34	0.027	0.529	36	0.039	0.628	23
15	WL	0.027	0.256	53	0.037	0.354	39	0.030	0.318	40	0.035	0.360	25
16	WL	0.042	0.257	43	0.036	0.329	35	0.040	0.255	36	0.039	0.370	21
17	WL	0.024	0.254	47	0.024	0.386	39	0.022	0.412	33	0.027	0.377	22
18	WL	0.026	0.138	43	0.025	0.159	42	0.030	0.157	33	0.026	0.209	21
19	WL	0.045	0.120	52	0.042	0.170	39	0.048	0.202	37	0.039	0.258	21
20	WL	0.040	0.166	44	0.028	0.244	34	0.038	0.225	32	0.032	0.341	19
21	WL	0.018	0.486	22	0.016	0.448	28	0.022	0.403	22	0.014	0.640	11
22	WL	0.025	0.417	35	0.034	0.391	36	0.038	0.329	32	0.038	0.510	13
23	WL	0.040	0.199	20	0.046	0.258	19	0.046	0.240	23	0.042	0.387	10
24	WL	0.041	0.519	36	0.057	0.357	39	0.044	0.442	32	0.054	0.408	22

25	WL	0.015	0.403	22	0.015	0.328	26	0.016	0.409	21	0.021	0.515	12
26	WL	0.022	0.321	26	0.022	0.388	34	0.023	0.312	29	0.022	0.460	18
27	WL	0.014	0.275	30	0.014	0.378	29	0.020	0.274	26	0.021	0.320	17
28	WL	0.096	0.159	36	0.071	0.194	36	0.074	0.178	31	0.046	0.307	23
29	WL	0.050	0.163	36	0.044	0.237	37	0.051	0.193	29	0.032	0.282	23
30	WL	0.035	0.164	42	0.038	0.212	30	0.039	0.208	27	0.030	0.277	25
31	WL	0.021	0.171	35	0.031	0.203	33	0.025	0.221	29	0.025	0.277	22
1	Hs	0.009	0.193	27	0.015	0.535	27	0.016	0.448	26	0.029	0.474	14
2	Hs	0.008	0.302	13	0.011	0.278	33	0.012	0.587	32	0.023	0.524	29
3	Hs	0.009	0.515	15	0.012	0.493	30	0.016	0.652	34	0.026	0.672	28
4	Hs	0.007	0.783	15	0.011	0.900	29	0.014	0.923	25	0.023	0.891	19
5	Hs	0.065	0.269	47	0.035	0.785	28	0.034	0.747	23	0.040	0.939	20
6	Hs	0.061	0.147	58	0.033	0.604	36	0.034	0.597	18	0.036	0.687	13
7	Hs	0.096	0.215	78	0.101	0.231	37	0.110	0.340	13	0.059	0.739	7
8	Hs	0.057	0.188	88	0.054	0.278	37	0.052	0.458	13	0.040	1.869	1
9	Hs	0.020	0.323	54	0.034	0.345	35	0.043	0.422	9	0.070	0.518	2
10	Hs	0.044	0.186	44	0.037	0.272	33	0.046	0.339	23	0.044	0.604	12
11	Hs	0.013	0.776	41	0.019	0.843	25	0.026	1.124	16	0.036	1.030	11
12	Hs	0.017	0.505	31	0.022	0.813	45	0.029	0.804	32	0.046	0.957	23
13	Hs	0.060	0.208	37	0.040	0.342	39	0.040	0.440	31	0.052	0.621	37
14	Hs	0.016	0.425	19	0.024	0.470	42	0.034	0.537	50	0.040	0.817	27
15	Hs	0.030	0.122	41	0.032	0.249	43	0.032	0.413	53	0.036	0.632	20
16	Hs	0.044	0.172	34	0.040	0.223	39	0.037	0.365	48	0.038	0.497	14
17	Hs	0.023	0.176	28	0.024	0.276	40	0.023	0.422	44	0.028	0.462	29
18	Hs	0.018	0.104	29	0.032	0.104	31	0.026	0.193	41	0.031	0.212	38

19	Hs	0.034	0.108	34	0.048	0.139	35	0.044	0.175	44	0.044	0.248	36
20	Hs	0.024	0.153	21	0.037	0.166	23	0.036	0.183	30	0.035	0.341	55
21	Hs	0.010	0.386	9	0.015	0.443	11	0.012	0.634	20	0.023	0.446	43
22	Hs	0.017	0.389	6	0.035	0.215	16	0.026	0.379	36	0.039	0.405	58
23	Hs	0.074	0.152	26	0.034	0.301	25	0.040	0.359	14	0.036	0.364	7
24	Hs	0.048	0.311	33	0.040	0.514	36	0.041	0.406	29	0.050	0.540	31
25	Hs	0.016	0.441	6	0.013	0.319	10	0.012	0.440	24	0.020	0.384	41
26	Hs	0.022	0.192	3	0.018	0.227	21	0.022	0.327	32	0.024	0.469	51
27	Hs	0.012	0.313	17	0.013	0.266	31	0.017	0.297	35	0.025	0.447	19
28	Hs	0.094	0.113	17	0.075	0.177	20	0.086	0.178	33	0.065	0.263	56
29	Hs	0.050	0.127	15	0.042	0.188	21	0.049	0.173	29	0.048	0.256	60
30	Hs	0.035	0.100	17	0.042	0.168	20	0.033	0.180	30	0.040	0.277	57
31	Hs	0.013	0.116	14	0.019	0.206	18	0.024	0.221	29	0.027	0.237	58
1	Ta	0.009	0.382	19	0.011	0.460	20	0.015	0.406	31	0.017	0.222	24
2	Ta	0.010	0.471	20	0.011	0.495	32	0.018	0.484	28	0.013	0.371	27
3	Ta	0.012	0.623	26	0.016	0.619	35	0.025	0.599	22	0.020	0.561	24
4	Ta	0.009	1.021	21	0.015	0.899	20	0.014	0.913	26	0.023	0.742	21
5	Ta	0.030	0.567	20	0.048	0.606	17	0.041	0.706	38	0.050	0.587	43
6	Ta	0.044	0.157	23	0.048	0.242	35	0.033	0.538	34	0.043	0.361	33
7	Ta	0.115	0.197	43	0.085	0.228	41	0.113	0.231	23	0.074	0.306	28
8	Ta	0.052	0.214	57	0.053	0.252	40	0.074	0.172	24	0.058	0.242	18
9	Ta	0.018	0.428	40	0.027	0.412	26	0.033	0.252	19	0.037	0.247	15
10	Ta	0.031	0.211	30	0.036	0.274	22	0.038	0.382	28	0.059	0.226	32
11	Ta	0.013	0.758	22	0.018	0.868	19	0.022	0.842	25	0.025	0.876	27
12	Ta	0.013	0.854	38	0.028	0.685	28	0.030	0.660	31	0.041	0.926	34

13	Ta	0.026	0.309	33	0.041	0.384	28	0.045	0.405	45	0.059	0.385	38
14	Ta	0.021	0.488	35	0.029	0.553	47	0.032	0.530	32	0.039	0.616	24
15	Ta	0.029	0.232	49	0.031	0.359	46	0.032	0.315	35	0.035	0.424	27
16	Ta	0.044	0.221	46	0.039	0.280	38	0.038	0.343	29	0.038	0.360	22
17	Ta	0.021	0.296	48	0.024	0.460	37	0.025	0.391	30	0.028	0.387	26
18	Ta	0.030	0.110	42	0.025	0.184	35	0.024	0.170	32	0.029	0.158	30
19	Ta	0.043	0.126	44	0.040	0.173	50	0.048	0.172	40	0.048	0.185	15
20	Ta	0.039	0.151	22	0.037	0.224	44	0.032	0.192	33	0.030	0.267	30
21	Ta	0.013	0.660	17	0.016	0.500	21	0.023	0.355	23	0.015	0.406	22
22	Ta	0.020	0.446	21	0.042	0.344	32	0.043	0.373	33	0.037	0.374	30
23	Ta	0.039	0.213	10	0.043	0.301	10	0.047	0.252	19	0.036	0.332	33
24	Ta	0.027	0.442	23	0.043	0.398	21	0.055	0.350	37	0.049	0.499	48
25	Ta	0.012	0.493	15	0.016	0.356	19	0.015	0.386	22	0.022	0.409	25
26	Ta	0.019	0.316	22	0.025	0.360	18	0.022	0.348	29	0.024	0.375	38
27	Ta	0.013	0.279	35	0.020	0.444	27	0.016	0.345	23	0.021	0.369	17
28	Ta	0.076	0.169	26	0.074	0.261	29	0.062	0.209	32	0.075	0.189	39
29	Ta	0.076	0.154	21	0.047	0.226	29	0.036	0.255	29	0.049	0.212	46
30	Ta	0.035	0.188	24	0.035	0.273	26	0.029	0.209	34	0.042	0.201	40
31	Ta	0.022	0.255	25	0.024	0.251	24	0.023	0.219	30	0.029	0.181	40

Appendix III: Table of C_0 and *b* equations when split in wave parameter quartiles

Site	*P*	Q_1 *D*	Q_1 *n*	Q_2 *D*	Q_2 *n*	Q_3 *D*	Q_3 *n*	Q_4 *D*	Q_4 *n*
1	WL	0.32	14	0.55	22	0.42	25	0.42	33
2	WL	0.41	16	0.50	21	0.54	29	0.56	41
3	WL	0.53	16	0.86	21	0.85	31	0.87	39
4	WL	0.54	13	0.99	19	1.16	22	1.21	34
5	WL	0.67	18	1.42	21	1.96	31	1.70	48
6	WL	0.52	25	0.45	26	1.24	25	1.10	49
7	WL	0.76	24	0.68	26	1.12	33	0.84	52
8	WL	0.58	27	0.60	27	0.80	33	0.75	52
9	WL	0.46	15	0.82	19	0.96	25	1.03	41
10	WL	0.54	23	0.91	22	0.86	27	0.95	40
11	WL	0.85	16	1.09	20	1.56	26	1.67	31
12	WL	0.84	25	1.46	28	1.42	30	2.17	48
13	WL	0.78	27	1.14	31	0.94	35	1.24	51
14	WL	0.91	45	1.25	34	1.25	36	1.86	23
15	WL	0.51	53	0.94	39	0.94	40	1.06	25
16	WL	0.63	43	0.83	35	0.82	36	1.14	21
17	WL	0.47	47	0.76	39	0.90	33	0.98	22
18	WL	0.27	43	0.35	42	0.41	33	0.61	21
19	WL	0.32	52	0.48	39	0.64	37	0.94	21
20	WL	0.42	44	0.56	34	0.62	32	1.15	19
21	WL	0.73	22	0.72	28	0.77	22	1.03	11
22	WL	0.73	35	0.92	36	0.88	32	1.41	13
23	WL	0.50	20	0.81	19	0.76	23	1.19	10
24	WL	1.31	36	1.09	39	1.19	32	1.20	22
25	WL	0.50	22	0.46	26	0.57	21	1.20	12
26	WL	0.52	26	0.71	34	0.56	29	0.80	18
27	WL	0.30	30	0.56	29	0.48	26	0.63	17
28	WL	0.50	36	0.61	36	0.55	31	0.80	23
29	WL	0.41	36	0.60	37	0.51	29	0.66	23
30	WL	0.37	42	0.54	30	0.53	27	0.66	25
31	WL	0.28	35	0.49	33	0.46	29	0.62	22
1	Hs	0.13	27	0.75	27	0.75	26	1.13	14
2	Hs	0.13	13	0.28	33	0.80	32	1.14	29
3	Hs	0.35	15	0.48	30	0.86	34	1.26	28
4	Hs	0.22	15	0.90	29	1.07	25	1.88	19
5	Hs	0.76	47	1.75	28	1.75	23	2.21	20
6	Hs	0.40	58	1.37	36	1.36	18	1.75	13
7	Hs	0.72	78	0.92	37	1.67	13	5.59	7
8	Hs	0.54	88	0.94	37	1.76	13	2.37	1
9	Hs	0.65	54	0.98	35	1.51	9	4.13	2
10	Hs	0.48	44	0.84	33	1.39	23	1.95	12
11	Hs	0.98	41	1.55	25	1.93	16	2.21	11

12	Hs	0.75	31	1.44	45	2.10	32	2.33	23
13	Hs	0.58	37	0.88	39	1.34	31	2.01	37
14	Hs	0.62	19	0.86	42	1.38	50	2.25	27
15	Hs	0.25	41	0.58	43	1.30	53	2.54	20
16	Hs	0.44	34	0.58	39	1.06	48	1.63	14
17	Hs	0.30	28	0.52	40	0.89	44	1.45	29
18	Hs	0.17	29	0.25	31	0.46	41	0.65	38
19	Hs	0.24	34	0.39	35	0.50	44	0.90	36
20	Hs	0.31	21	0.41	23	0.45	30	1.04	55
21	Hs	0.37	9	0.56	11	0.84	20	0.95	43
22	Hs	0.51	6	0.50	16	0.75	36	1.14	58
23	Hs	0.50	26	0.87	25	1.21	14		7
24	Hs	0.82	33	1.31	36	1.18	29	1.67	31
25	Hs	0.47	6	0.37	10	0.49	24	0.72	41
26	Hs	0.28	3	0.34	21	0.56	32	0.87	51
27	Hs	0.34	17	0.32	31	0.50	35	0.96	19
28	Hs	0.35	17	0.53	20	0.54	33	0.82	56
29	Hs	0.32	15	0.44	21	0.44	29	0.71	60
30	Hs	0.22	17	0.41	20	0.39	30	0.71	57
31	Hs	0.13	14	0.34	18	0.42	29	0.54	58
1	Ta	0.28	19	0.44	20	0.65	31	0.39	24
2	Ta	0.43	20	0.45	32	0.82	28	0.56	27
3	Ta	0.61	26	0.75	35	1.10	22	0.90	24
4	Ta	0.47	21	0.94	20	1.06	26	1.60	21
5	Ta	1.09	20	1.42	17	1.76	38	1.61	43
6	Ta	0.36	23	0.61	35	1.22	34	0.95	33
7	Ta	0.70	43	0.83	41	0.91	23	1.06	28
8	Ta	0.59	57	0.82	40	0.63	24	0.90	18
9	Ta	0.78	40	1.04	26	0.67	19	0.75	15
10	Ta	0.48	30	0.72	22	1.14	28	0.94	32
11	Ta	0.92	22	1.29	19	1.62	25	1.54	27
12	Ta	1.07	38	1.22	28	1.60	31	2.25	34
13	Ta	0.63	33	0.93	28	1.11	45	1.21	38
14	Ta	0.81	35	1.16	47	1.24	32	1.60	24
15	Ta	0.52	49	0.83	46	0.99	35	1.16	27
16	Ta	0.58	46	0.72	38	1.04	29	0.97	22
17	Ta	0.52	48	0.86	37	0.91	30	0.93	26
18	Ta	0.24	42	0.43	35	0.44	32	0.42	30
19	Ta	0.33	44	0.48	50	0.55	40	0.57	15
20	Ta	0.37	22	0.57	44	0.50	33	0.69	30
21	Ta	0.76	17	0.66	21	0.83	23	0.71	22
22	Ta	0.75	21	0.93	32	0.98	33	0.97	30
23	Ta	0.56	10	0.84	10	0.81	19	0.99	33

24	Ta	0.88	23	1.02	21	1.16	37	1.38	48
25	Ta	0.51	15	0.49	19	0.63	22	0.72	25
26	Ta	0.48	22	0.66	18	0.61	29	0.72	38
27	Ta	0.33	35	0.80	27	0.56	23	0.69	17
28	Ta	0.48	26	0.77	29	0.60	32	0.60	39
29	Ta	0.44	21	0.57	29	0.60	29	0.57	46
30	Ta	0.40	24	0.63	26	0.49	34	0.53	40
31	Ta	0.42	25	0.48	24	0.46	30	0.42	40

Appendix IV: Table of distance of clear water threshold in average decay equations in dates subset by wave parameter quartiles

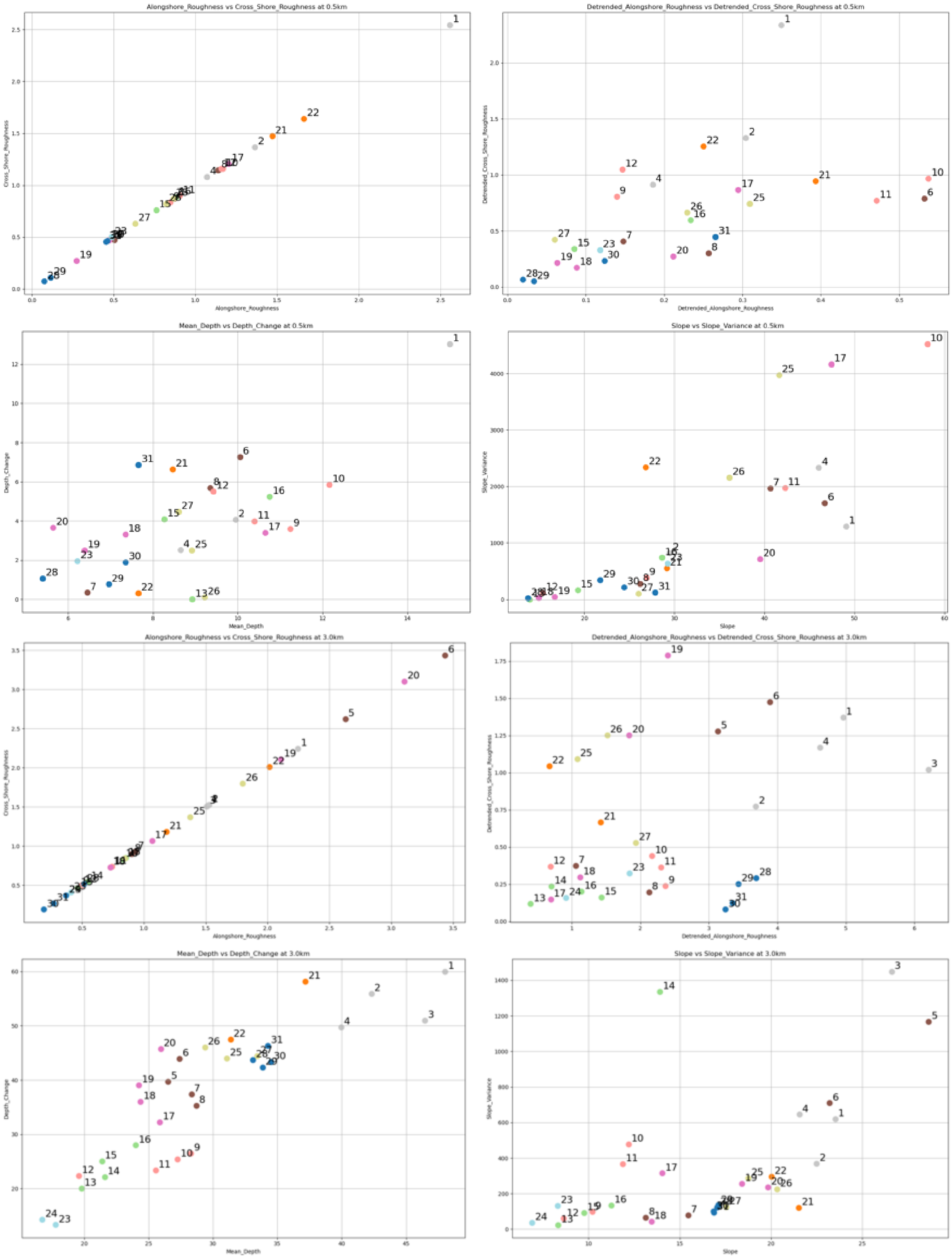

Appendix V: Plots of bathymetric variables in .5km (top) and 3km (bottom) bins.

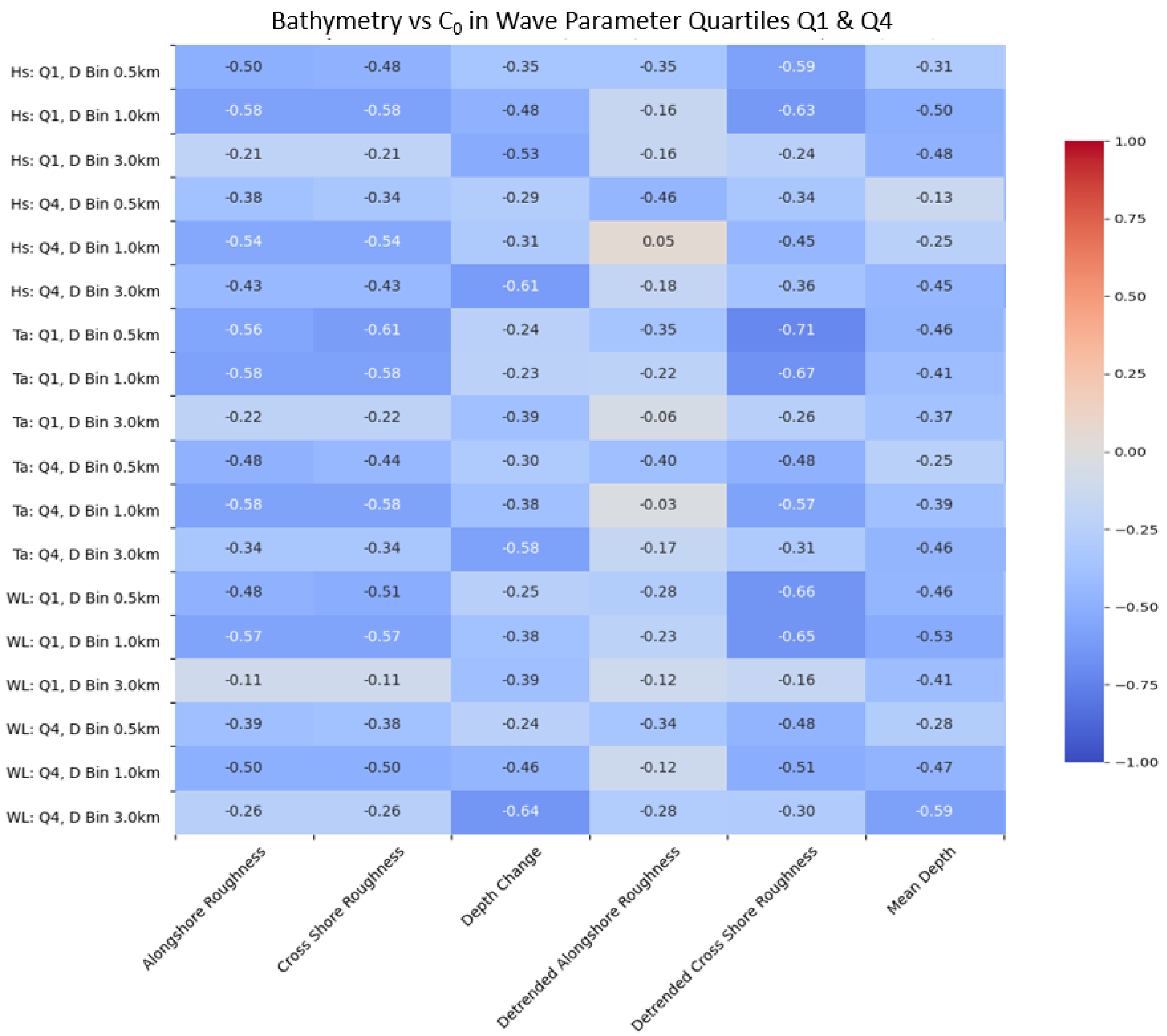

Bathymetry vs C_0 in Wave Parameter Quartiles Q1 & Q4

	Alongshore Roughness	Cross Shore Roughness	Depth Change	Detrended Alongshore Roughness	Detrended Cross Shore Roughness	Mean Depth
Hs: Q1, D Bin 0.5km	-0.50	-0.48	-0.35	-0.35	-0.59	-0.31
Hs: Q1, D Bin 1.0km	-0.58	-0.58	-0.48	-0.16	-0.63	-0.50
Hs: Q1, D Bin 3.0km	-0.21	-0.21	-0.53	-0.16	-0.24	-0.48
Hs: Q4, D Bin 0.5km	-0.38	-0.34	-0.29	-0.46	-0.34	-0.13
Hs: Q4, D Bin 1.0km	-0.54	-0.54	-0.31	0.05	-0.45	-0.25
Hs: Q4, D Bin 3.0km	-0.43	-0.43	-0.61	-0.18	-0.36	-0.45
Ta: Q1, D Bin 0.5km	-0.56	-0.61	-0.24	-0.35	-0.71	-0.46
Ta: Q1, D Bin 1.0km	-0.58	-0.58	-0.23	-0.22	-0.67	-0.41
Ta: Q1, D Bin 3.0km	-0.22	-0.22	-0.39	-0.06	-0.26	-0.37
Ta: Q4, D Bin 0.5km	-0.48	-0.44	-0.30	-0.40	-0.48	-0.25
Ta: Q4, D Bin 1.0km	-0.58	-0.58	-0.38	-0.03	-0.57	-0.39
Ta: Q4, D Bin 3.0km	-0.34	-0.34	-0.58	-0.17	-0.31	-0.46
WL: Q1, D Bin 0.5km	-0.48	-0.51	-0.25	-0.28	-0.66	-0.46
WL: Q1, D Bin 1.0km	-0.57	-0.57	-0.38	-0.23	-0.65	-0.53
WL: Q1, D Bin 3.0km	-0.11	-0.11	-0.39	-0.12	-0.16	-0.41
WL: Q4, D Bin 0.5km	-0.39	-0.38	-0.24	-0.34	-0.48	-0.28
WL: Q4, D Bin 1.0km	-0.50	-0.50	-0.46	-0.12	-0.51	-0.47
WL: Q4, D Bin 3.0km	-0.26	-0.26	-0.64	-0.28	-0.30	-0.59

Bathymetry vs b^{-1} in Wave Parameter Quartiles Q1 & Q4

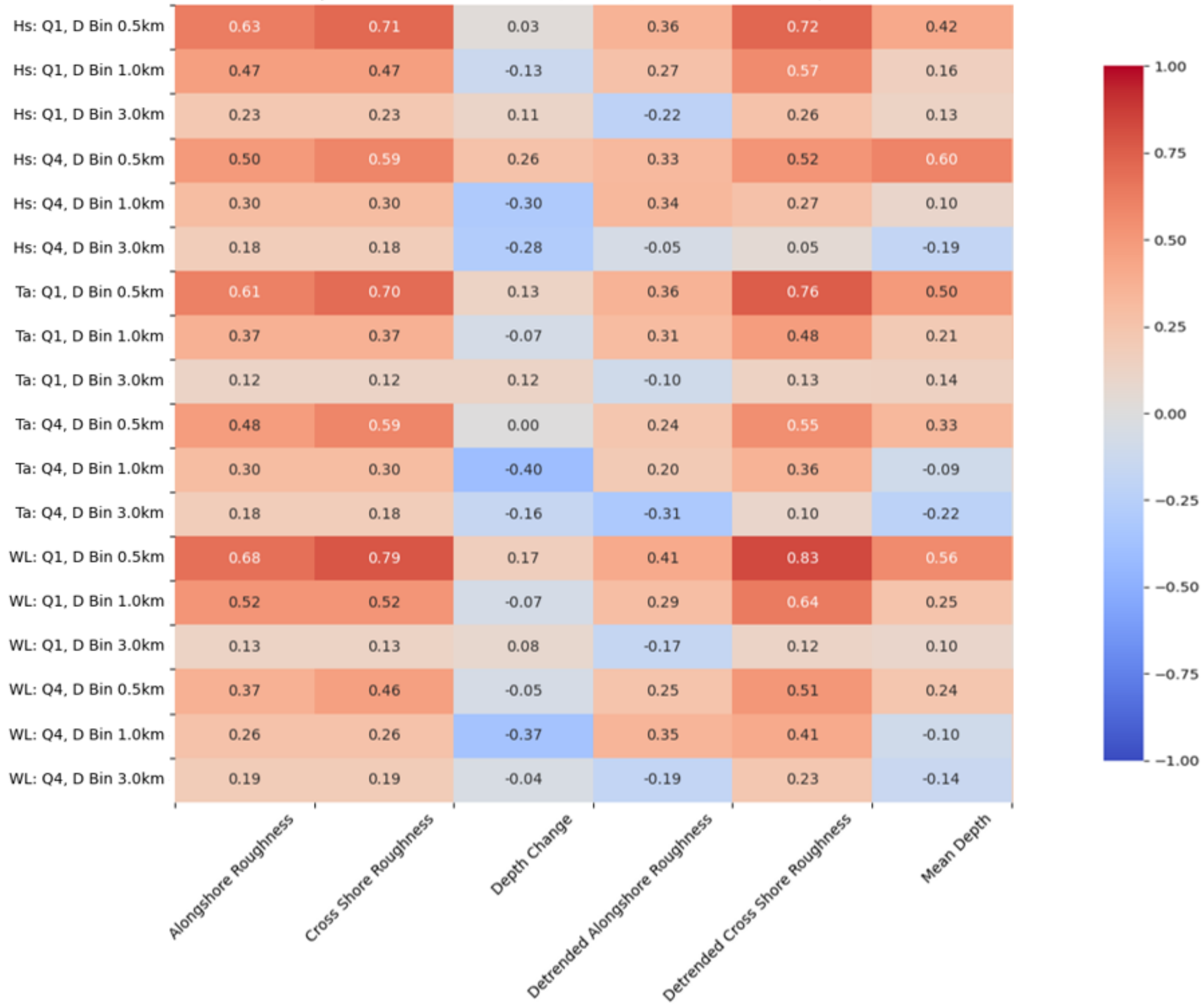

	Alongshore Roughness	Cross Shore Roughness	Depth Change	Detrended Alongshore Roughness	Detrended Cross Shore Roughness	Mean Depth
Hs: Q1, D Bin 0.5km	0.63	0.71	0.03	0.36	0.72	0.42
Hs: Q1, D Bin 1.0km	0.47	0.47	-0.13	0.27	0.57	0.16
Hs: Q1, D Bin 3.0km	0.23	0.23	0.11	-0.22	0.26	0.13
Hs: Q4, D Bin 0.5km	0.50	0.59	0.26	0.33	0.52	0.60
Hs: Q4, D Bin 1.0km	0.30	0.30	-0.30	0.34	0.27	0.10
Hs: Q4, D Bin 3.0km	0.18	0.18	-0.28	-0.05	0.05	-0.19
Ta: Q1, D Bin 0.5km	0.61	0.70	0.13	0.36	0.76	0.50
Ta: Q1, D Bin 1.0km	0.37	0.37	-0.07	0.31	0.48	0.21
Ta: Q1, D Bin 3.0km	0.12	0.12	0.12	-0.10	0.13	0.14
Ta: Q4, D Bin 0.5km	0.48	0.59	0.00	0.24	0.55	0.33
Ta: Q4, D Bin 1.0km	0.30	0.30	-0.40	0.20	0.36	-0.09
Ta: Q4, D Bin 3.0km	0.18	0.18	-0.16	-0.31	0.10	-0.22
WL: Q1, D Bin 0.5km	0.68	0.79	0.17	0.41	0.83	0.56
WL: Q1, D Bin 1.0km	0.52	0.52	-0.07	0.29	0.64	0.25
WL: Q1, D Bin 3.0km	0.13	0.13	0.08	-0.17	0.12	0.10
WL: Q4, D Bin 0.5km	0.37	0.46	-0.05	0.25	0.51	0.24
WL: Q4, D Bin 1.0km	0.26	0.26	-0.37	0.35	0.41	-0.10
WL: Q4, D Bin 3.0km	0.19	0.19	-0.04	-0.19	0.23	-0.14

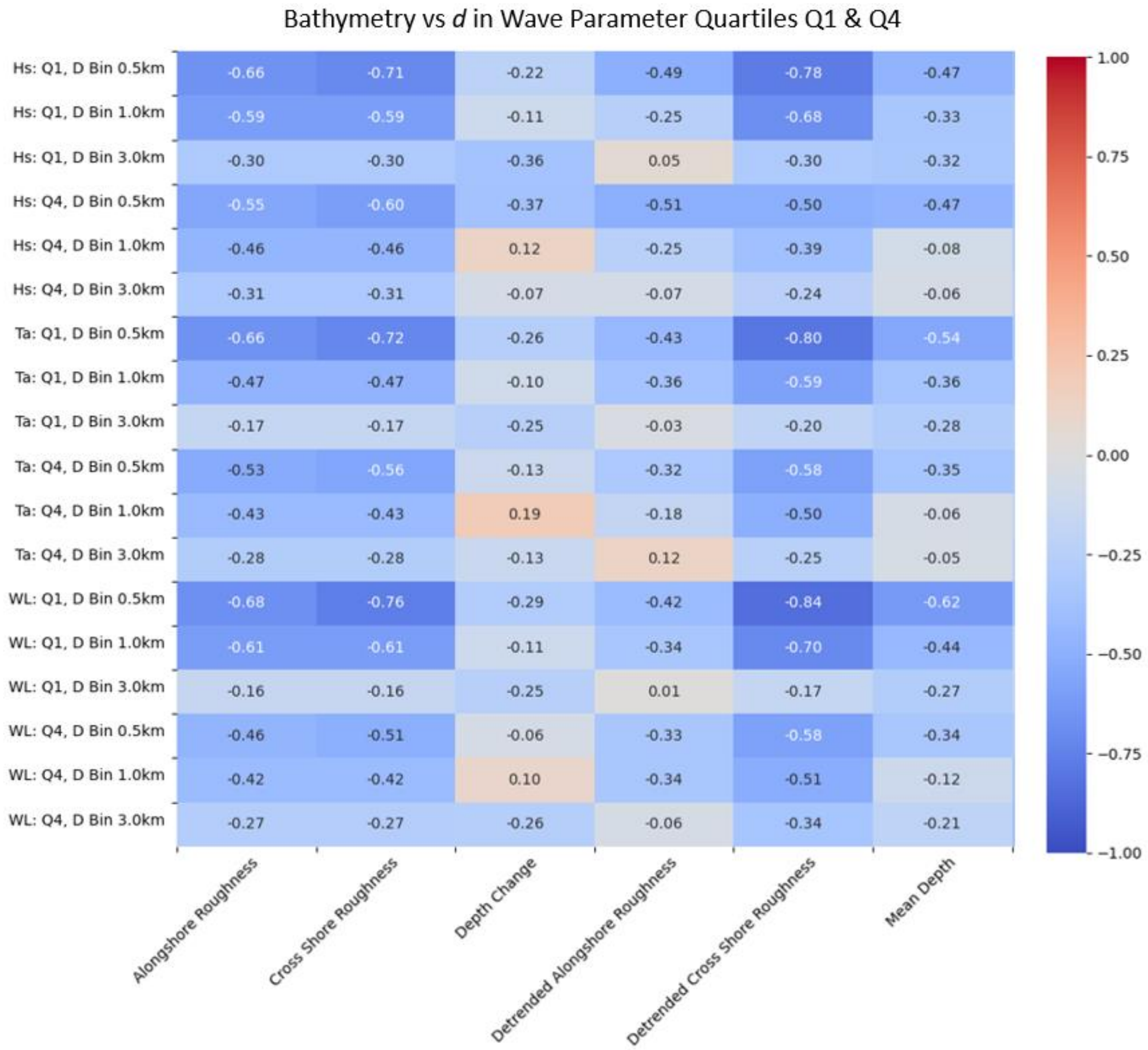

Bathymetry vs *d* in Wave Parameter Quartiles Q1 & Q4

	Alongshore Roughness	Cross Shore Roughness	Depth Change	Detrended Alongshore Roughness	Detrended Cross Shore Roughness	Mean Depth
Hs: Q1, D Bin 0.5km	-0.66	-0.71	-0.22	-0.49	-0.78	-0.47
Hs: Q1, D Bin 1.0km	-0.59	-0.59	-0.11	-0.25	-0.68	-0.33
Hs: Q1, D Bin 3.0km	-0.30	-0.30	-0.36	0.05	-0.30	-0.32
Hs: Q4, D Bin 0.5km	-0.55	-0.60	-0.37	-0.51	-0.50	-0.47
Hs: Q4, D Bin 1.0km	-0.46	-0.46	0.12	-0.25	-0.39	-0.08
Hs: Q4, D Bin 3.0km	-0.31	-0.31	-0.07	-0.07	-0.24	-0.06
Ta: Q1, D Bin 0.5km	-0.66	-0.72	-0.26	-0.43	-0.80	-0.54
Ta: Q1, D Bin 1.0km	-0.47	-0.47	-0.10	-0.36	-0.59	-0.36
Ta: Q1, D Bin 3.0km	-0.17	-0.17	-0.25	-0.03	-0.20	-0.28
Ta: Q4, D Bin 0.5km	-0.53	-0.56	-0.13	-0.32	-0.58	-0.35
Ta: Q4, D Bin 1.0km	-0.43	-0.43	0.19	-0.18	-0.50	-0.06
Ta: Q4, D Bin 3.0km	-0.28	-0.28	-0.13	0.12	-0.25	-0.05
WL: Q1, D Bin 0.5km	-0.68	-0.76	-0.29	-0.42	-0.84	-0.62
WL: Q1, D Bin 1.0km	-0.61	-0.61	-0.11	-0.34	-0.70	-0.44
WL: Q1, D Bin 3.0km	-0.16	-0.16	-0.25	0.01	-0.17	-0.27
WL: Q4, D Bin 0.5km	-0.46	-0.51	-0.06	-0.33	-0.58	-0.34
WL: Q4, D Bin 1.0km	-0.42	-0.42	0.10	-0.34	-0.51	-0.12
WL: Q4, D Bin 3.0km	-0.27	-0.27	-0.26	-0.06	-0.34	-0.21

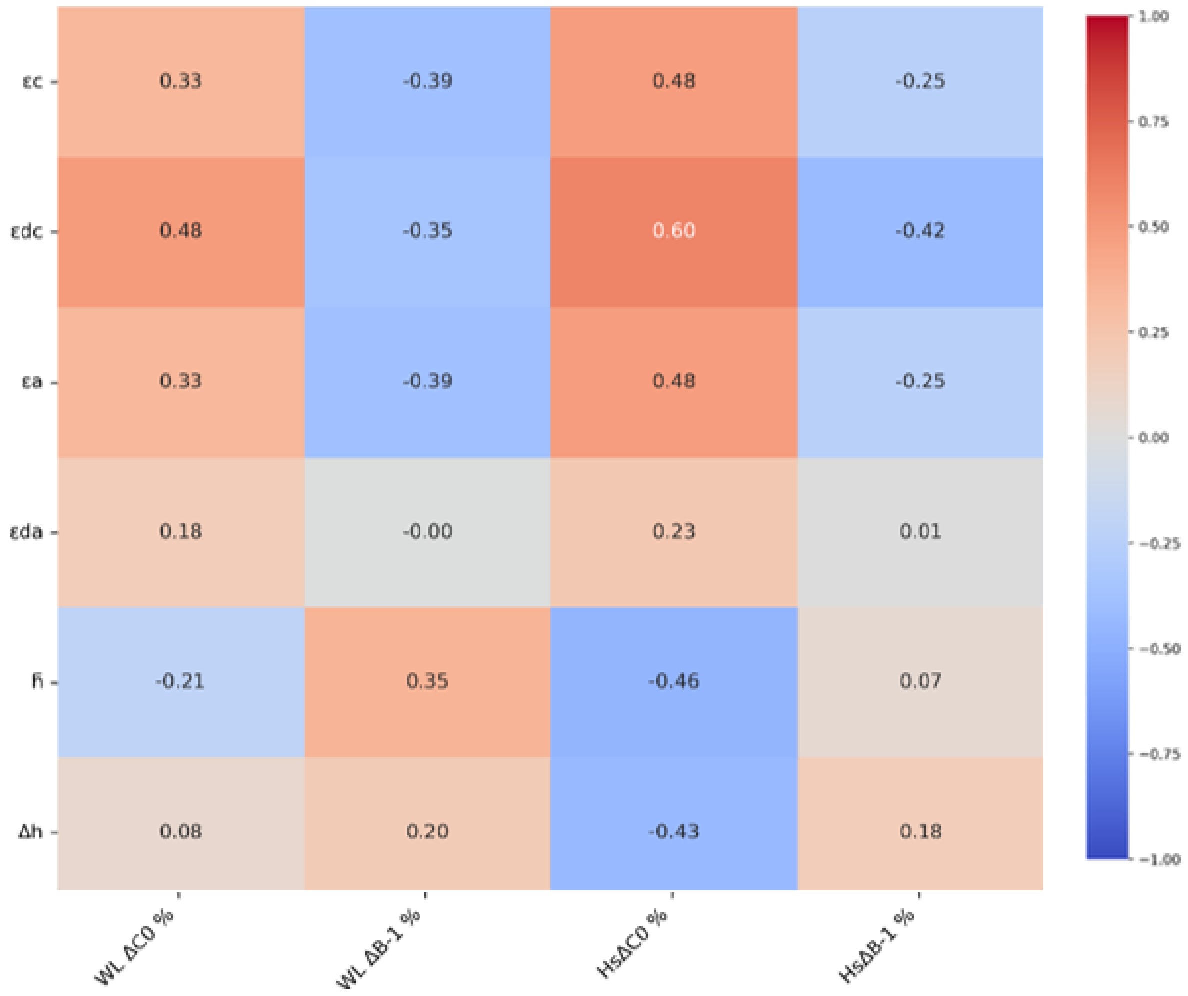

Appendix V: Sitewise results considering Ta

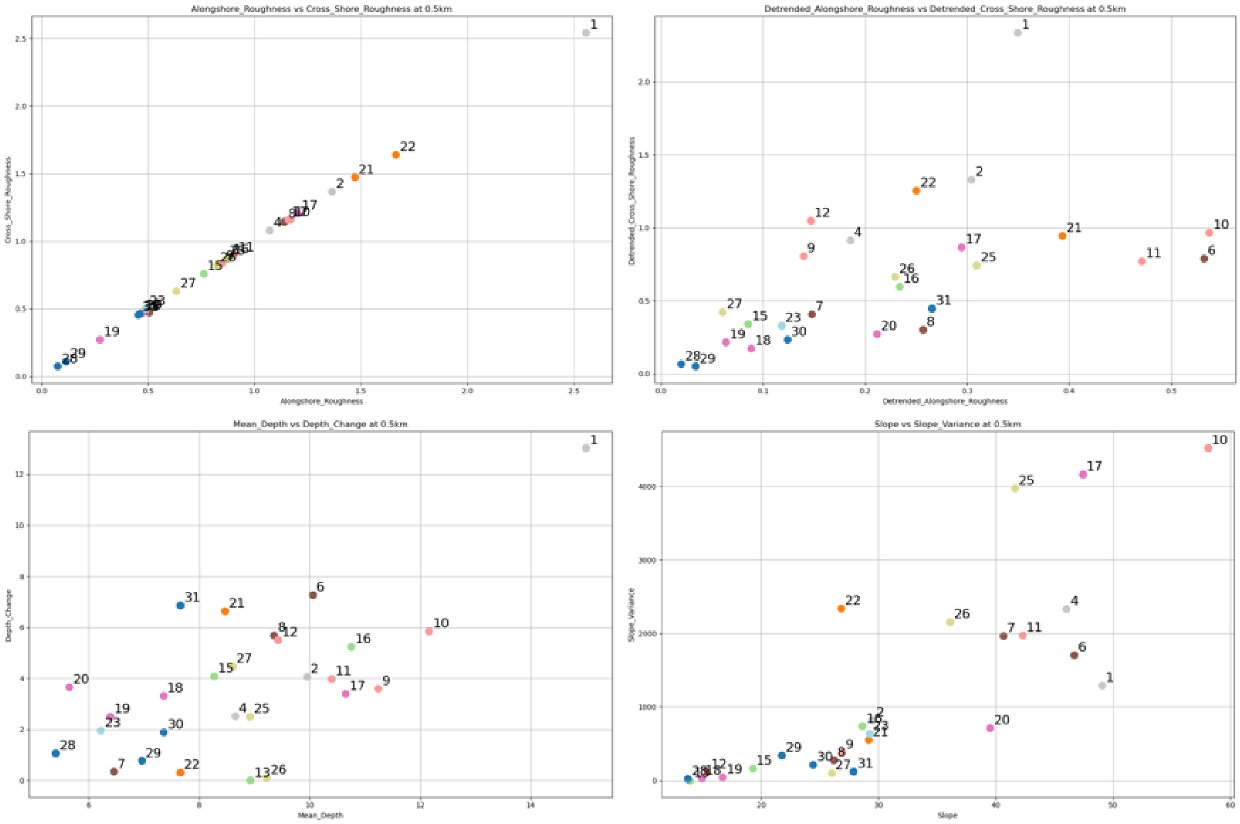
Alongshore_Roughness vs Cross_Shore_Roughness at 0.5km
Alongshore_Roughness
Cross_Shore_Roughness
Detrended_Alongshore_Roughness vs Detrended_Cross_Shore_Roughness at 0.5km
Detrended_Alongshore_Roughness
Detrended_Cross_Shore_Roughness
Mean_Depth vs Depth_Change at 0.5km
Mean_Depth
Depth_Change
Slope vs Slope_Variance at 0.5km
Slope
Slope_Variance

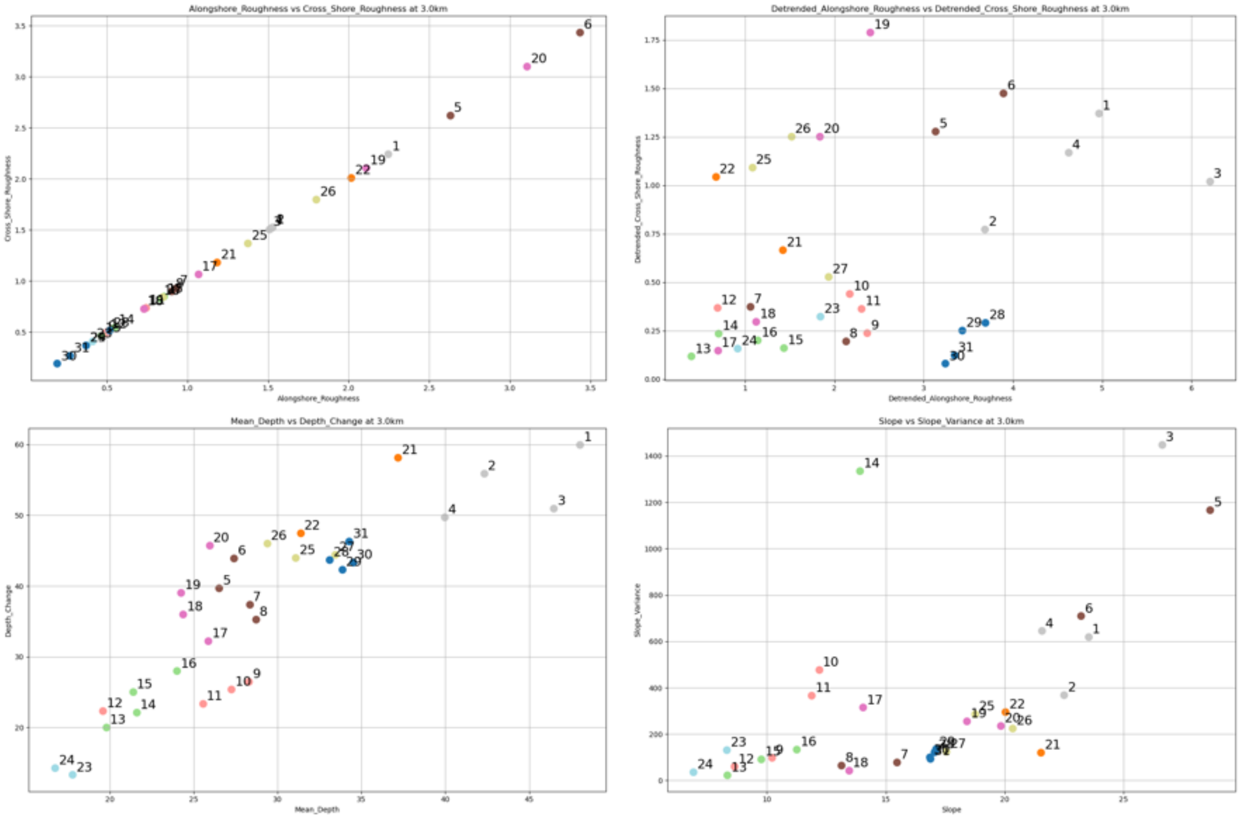
Alongshore_Roughness vs Cross_Shore_Roughness at 3.0km
Alongshore_Roughness
Cross_Shore_Roughness
Detrended_Alongshore_Roughness vs Detrended_Cross_Shore_Roughness at 3.0km
Detrended_Alongshore_Roughness
Detrended_Cross_Shore_Roughness
Mean_Depth vs Depth_Change at 3.0km
Mean_Depth
Depth_Change
Slope vs Slope_Variance at 3.0km
Slope
Slope_Variance

Appendix III: Bathymetric characteristic comparisons of each site binned at .5km and 3km offshore. Note: some sites have no available data within the first .5km, and are excluded from respective .5km plots.

Site ID	D Bin	εc	ε_{dc}	ε_{a}	ε_{da}	$\bar{h}$	Δh
1	0.5	2.54	2.34	2.56	0.35	-15.00	-13.02
2	0.5	1.37	1.33	1.36	0.30	-9.94	-4.07
3	0.5						
4	0.5	1.08	0.91	1.07	0.19	-8.65	-2.52
5	0.5						
6	0.5	0.87	0.79	0.87	0.53	-10.05	-7.28
7	0.5	0.47	0.41	0.51	0.15	-6.45	-0.35
8	0.5	1.14	0.30	1.14	0.26	-9.35	-5.69
9	0.5	0.84	0.81	0.85	0.14	-11.24	-3.61
10	0.5	1.16	0.97	1.17	0.54	-12.16	-5.84
11	0.5	0.90	0.77	0.91	0.47	-10.40	-3.98
12	0.5	1.16	1.05	1.16	0.15	-9.42	-5.52
13	0.5			0.05	0.00	-8.93	0.00
14	0.5						
15	0.5	0.76	0.34	0.76	0.09	-8.27	-4.10
16	0.5	0.88	0.60	0.88	0.23	-10.75	-5.24
17	0.5	1.21	0.87	1.20	0.29	-10.65	-3.41
18	0.5	0.47	0.17	0.47	0.09	-7.35	-3.32
19	0.5	0.27	0.22	0.27	0.06	-6.39	-2.50
20	0.5	0.47	0.27	0.47	0.21	-5.64	-3.66
21	0.5	1.47	0.95	1.47	0.39	-8.47	-6.65
22	0.5	1.64	1.26	1.66	0.25	-7.65	-0.31
23	0.5	0.50	0.33	0.49	0.12	-6.22	-1.95
24	0.5						
25	0.5	0.82	0.67	0.82	0.23	-9.21	-0.12
26	0.5	0.87	0.75	0.87	0.31	-8.92	-2.51
27	0.5	0.63	0.42	0.63	0.06	-8.60	-4.48
28	0.5	0.07	0.07	0.08	0.02	-5.40	-1.06
29	0.5	0.11	0.05	0.12	0.03	-6.95	-0.77
30	0.5	0.46	0.24	0.46	0.12	-7.35	-1.90
31	0.5	0.46	0.45	0.45	0.27	-7.65	-6.87
1	1	4.66	3.46	4.66	1.34	-23.79	-28.86
2	1	3.64	1.80	3.64	0.36	-16.71	-17.77
3	1	4.25	3.14	4.26	2.78	-17.09	-18.60
4	1	3.33	3.10	3.33	1.74	-15.72	-22.18

5	1	0.09	0.03	0.10	0.43	-10.87	-0.87
6	1	2.36	1.31	2.36	1.62	-14.27	-9.37
7	1	0.74	0.34	0.74	0.33	-12.06	-9.99
8	1	0.99	0.18	0.99	0.31	-14.24	-14.44
9	1	0.69	0.65	0.69	0.85	-17.53	-13.52
10	1	1.47	1.36	1.47	1.12	-18.13	-14.74
11	1	1.34	1.17	1.34	0.95	-16.76	-13.59
12	1	0.77	0.71	0.77	0.59	-11.88	-8.67
13	1	0.53	0.32	0.53	0.40	-12.08	-5.51
14	1	0.98	0.81	0.98	0.65	-12.63	-5.88
15	1	1.11	0.44	1.11	0.40	-12.82	-11.91
16	1	0.63	0.44	0.63	0.57	-15.14	-11.90
17	1	1.01	0.37	1.01	0.54	-15.05	-10.55
18	1	0.65	0.18	0.65	0.25	-11.65	-12.45
19	1	0.98	0.60	0.98	0.29	-11.36	-13.17
20	1	0.81	0.64	0.81	0.32	-11.29	-13.74
21	1	1.39	0.81	1.39	0.27	-14.68	-18.53
22	1	1.86	1.33	1.87	0.63	-12.76	-11.62
23	1	0.49	0.36	0.49	0.46	-11.26	-9.96
24	1	0.43	0.29	0.43	0.12	-9.88	-4.95
25	1	1.40	1.29	1.40	0.27	-10.79	-3.96
26	1	1.52	1.01	1.52	0.43	-12.88	-11.00
27	1	0.86	0.48	0.86	0.18	-14.74	-16.20
28	1	0.52	0.19	0.52	0.88	-12.43	-18.11
29	1	0.35	0.10	0.35	0.42	-14.53	-16.98
30	1	0.32	0.12	0.32	0.33	-15.94	-18.72
31	1	0.37	0.28	0.37	0.53	-16.07	-22.22
1	3	2.25	1.37	2.25	4.96	-48.02	-59.95
2	3	1.53	0.77	1.53	3.68	-42.30	-55.89
3	3	1.51	1.02	1.51	6.20	-46.45	-51.00
4	3	1.52	1.17	1.52	4.62	-39.94	-49.72
5	3	2.62	1.28	2.63	3.13	-26.51	-39.74
6	3	3.43	1.48	3.43	3.89	-27.40	-43.96
7	3	0.93	0.37	0.93	1.06	-28.33	-37.40
8	3	0.90	0.20	0.90	2.13	-28.69	-35.26
9	3	0.49	0.24	0.49	2.37	-28.28	-26.49
10	3	0.73	0.44	0.73	2.17	-27.24	-25.44
11	3	0.74	0.36	0.74	2.30	-25.54	-23.39
12	3	0.50	0.37	0.50	0.69	-19.58	-22.35
13	3	0.47	0.12	0.47	0.39	-19.78	-20.01
14	3	0.55	0.24	0.55	0.70	-21.58	-22.14
15	3	0.85	0.16	0.85	1.43	-21.37	-25.05
16	3	0.83	0.20	0.83	1.14	-23.99	-27.99

17	3	1.07	0.15	1.07	0.69	-25.87	-32.22
18	3	0.73	0.30	0.73	1.12	-24.36	-35.99
19	3	2.11	1.79	2.11	2.40	-24.23	-39.07
20	3	3.10	1.25	3.11	1.84	-25.94	-45.78
21	3	1.18	0.67	1.18	1.42	-37.18	-58.17
22	3	2.01	1.04	2.02	0.67	-31.36	-47.51
23	3	0.41	0.32	0.41	1.84	-17.78	-13.31
24	3	0.37	0.16	0.37	0.91	-16.73	-14.28
25	3	1.80	1.25	1.80	1.52	-29.37	-46.06
26	3	1.37	1.09	1.37	1.08	-31.08	-44.01
27	3	0.85	0.53	0.85	1.93	-33.43	-44.45
28	3	0.52	0.29	0.52	3.69	-33.11	-43.74
29	3	0.37	0.25	0.37	3.43	-33.84	-42.33
30	3	0.19	0.08	0.19	3.24	-34.49	-43.37
31	3	0.27	0.13	0.27	3.34	-34.26	-46.34

Appendix IV: Bathymetric characteristic comparisons of each site binned at .5km and 3km offshore. Note: some sites have no available data within the first 0.5km, and are excluded from respective .5km plots.